

**Searches for stochastic gravitational waves and long
gravitational wave transients in LIGO S5 data**

A DISSERTATION
SUBMITTED TO THE FACULTY OF THE GRADUATE SCHOOL
OF THE UNIVERSITY OF MINNESOTA
BY

Shivaraj Kandhasamy

IN PARTIAL FULFILLMENT OF THE REQUIREMENTS
FOR THE DEGREE OF
DOCTOR OF PHILOSOPHY

Prof. Vuk Mandic, Adviser

December 2013

© Shivaraj Kandhasamy 2013
ALL RIGHTS RESERVED

ACKNOWLEDGEMENTS

It has been a memorable journey through the forests of science to get to this relatively significant (?) peak. It could not have happened without the help and guidance from many of my wonderful friends and colleagues.

First and foremost, I would like to thank my adviser Vuk Mandic for giving me this opportunity and also for his un-conditional support throughout my graduate years. He was a wonderful critic. He was quick to point out the problems (before they got bigger) and at the same time applaud the work when it was due. He was a welcoming person, even outside the academic. I am grateful to have had him as my PhD adviser. Thank you Vuk.

Second, I would like to thank all the members of LIGO's stochastic group from whom I learned very many things. I especially thank Eric Thrane, who also happened to be a post-doc at the University of Minnesota during my graduate years, for many insightful discussions on several projects I worked with him. He was also my go-to person for initial reading of my writings, for which I am very thankful. I would also like to thank Joe Romano, Nelson Christensen, Warren Anderson, Talukder Dipongkar, Nickolas Fotopoulos, Sanjit Mitra, Sean Morris, Tanner Prestegard, Patrick Meyers, Michael Coughlin, Tania Regimbau, Robert Schofield, Gwynne Crowder and Alan Weinstein for many helpful discussions. All these would not have happened without the LSC collaboration and its funding agency National Science Foundation, so I am very grateful to them for making this possible. I also thank Jan Harms, Gary Pavlis with whom I had the privilege to work on Homestake seismic array. My work with stochastic group was supported by National Science Foundation grant No. PHY-0758036 and the Homestake seismic array work by National Science Foundation grant No. PHY-0939669. My final year at the university was supported by the graduate school through Doctoral Dissertation Fellowship, for which I am very thankful to the University of Minnesota.

Apart from the people I mentioned above, there were many others in LIGO and VIRGO

collaborations from whom I learned a great deal on data analyses and gravitation waves. I am indebted to all of them.

I also have been fortunate to have had many wonderful friends with whom I rarely spoke of any physics but who were an integral and critical part of my life during all these years. I thank all of them and in particular many thanks to Kaushik Basu, Feng Luo, Xiaoyi Cui, Nadya Monina, Alexander Monin, Kwang Ho Hur, Tamilkadir Rajavel. During my stay at Minneapolis, I also found many friends and families who became part of my extended family, making my home away from home. In particular, I am grateful to Gopal's family, Sanjeev's family and Bairav's family for their exceptional hospitality. I also thank at this time, the physics department staff and my friends at the department for making my stay in this foreign country a pleasant one.

Finally, I thank my parents and brothers for their encouragement and sacrifice during all these years. I could not have come any where close to what I am now without their support. The fact that in our family, including our extended family, I was the first one to get a high school diploma of any kind is a testimony for their sacrifice. I definitely cannot express my gratitude for that in a few lines or even in any number of pages. I am very very grateful to have them as my parents.

To my parents

ABSTRACT

Incoherent superposition of gravitational waves from a large number of unresolved sources gives rise to the stochastic gravitational-wave background. This background could be of cosmological origin, produced by early universe events such as inflation. It could also be of astrophysical origin, produced by a large number of astrophysical objects such as binary neutron stars and black holes. Detection of the stochastic gravitational wave background would therefore provide information both about the state of the universe at its earliest moments and about its evolution at later times. Long gravitational-wave transients are gravitational waves whose times scales range from minutes to weeks. Such long gravitational-wave transients are predicted by a variety of astrophysical models, including stellar core collapse and accretion onto newly formed proto-neutron stars and black holes. Detection of long transient gravitational waves would provide clues about various dynamical process occurring in these astrophysical objects. In this thesis, we describe methods to search for stochastic and long transient gravitational waves in interferometric gravitational-wave detector data and present results obtained by using the Laser Interferometer Gravitational-wave Observatory (LIGO) data acquired during its fifth science run.

Contents

List of Tables	viii
List of Figures	ix
1 Gravitational waves: Sources and Detectors	1
1.1 Gravitational waves in general relativity	2
1.1.1 Weak field limit	3
1.1.2 Plane wave solutions	4
1.1.3 Effect of GWs on the distance between free masses	6
1.2 Gravitational wave sources	6
1.2.1 Sources with known signal model	7
1.2.2 Sources with unknown signal model	9
1.3 Gravitational wave detectors	11
1.3.1 Interferometric detectors	12
1.3.2 Detection prospects	16
1.4 Organization of other chapters	18
2 Searches for stochastic gravitational waves in LIGO data	19
2.1 Sources of stochastic GW background	20
2.1.1 Cosmological GW background	21
2.1.2 Astrophysical GW background	24
2.1.3 Observational constraints	25
2.2 Cross-correlation statistics	27

2.3	Analysis pipeline	35
2.3.1	Initial data selection	36
2.3.2	Data quality cuts	37
2.3.3	Applying cross-correlation statistic	38
2.4	Results using non-colocated LIGO detectors	41
2.4.1	Data quality cuts	41
2.4.2	Software and Hardware injections	41
2.4.3	Final results and implications	44
2.5	Results using colocated LIGO detectors	50
2.5.1	PEM coherence studies	53
2.5.2	Data quality cuts	56
2.5.3	Hardware and software injections	58
2.5.4	Final Results	58
2.6	Summary	61
3	Searches for long GW transients	64
3.1	Sources of Long GW Transients	65
3.1.1	Core-collapse supernovae	65
3.1.2	Postmerger evolution of compact binaries	67
3.1.3	Isolated neutron stars	68
3.2	An excess cross-power statistic	69
3.2.1	A single ft -map pixel	70
3.2.2	Energy, fluence and power	72
3.2.3	Multi-pixel statistic	73
3.2.4	Multi-detector statistic	75
3.2.5	Relationship to the GW radiometer	76
3.2.6	Relation to other search frameworks	77
3.3	Distribution of signal and background	78
3.4	Pattern recognition	78

3.4.1	Broadband box search	78
3.4.2	Other algorithms	79
3.4.3	Application to environmental noise identification	83
3.5	Searches for long GW transients from GRBs	85
3.5.1	Gamma-ray bursts	85
3.5.2	Methodology and preliminary results	85
3.6	Summary	88
4	Seismic waves and gravitational wave detectors	90
4.1	Seismic waves and Newtonian noise	91
4.1.1	Newtonian noise	93
4.2	Homestake seismic array	94
4.2.1	Initial results	98
4.3	Seismic field decomposition	100
4.4	Beamforming methods	101
4.4.1	Spectral based methods	102
4.4.2	Parametric methods	104
4.4.3	Simulation results	107
4.5	Summary	114
5	Conclusion and Discussion	115
	References	117
A	Statistics of long GW transient analysis pipeline	133
A.1	Derivations	133
A.1.1	Introduction and notation	133
A.1.2	Derivation of \hat{Y}	136
A.1.3	Variance of the estimator	138
A.1.4	Expectation value of $\hat{\sigma}_Y^2$	140
A.1.5	Distribution of $\text{SNR}(t; f, \hat{\Omega})$	141

CONTENTS

viii

B Flowcharts of analysis pipelines

146

List of Tables

2.1	Definition of various stages of noise removal in terms of the analysis steps described in Section 2.5.4. Here stage III is corresponds to the blind analysis and stage IV to post-unblinding analysis.	60
2.2	The different rows correspond to results obtained after various stages of noise removal. † The PEM-coherence estimate on stage I also excludes frequencies (such as 60 Hz harmonics) and time segments similar to stages II-IV.	61
4.1	A table providing the location and type of seismometer used at each station. The location coordinates are measured with respect to the (Yates) mine-shaft elevator.	96

List of Figures

1.1	An example waveform showing the inspiral part of GW signal from a coalescing binary. The y-axis corresponds to instantaneous strain amplitude of the GW signal. Image from [109].	9
1.2	An outline of interferometric GW detector. Image from [68].	13
1.3	Strain spectra for LIGO detectors (H1, H2, L1) and Virgo detector (V1) during their S5 and VSR1 science runs respectively. The legend also provides distances up to which the detectors can detect a CBC signal with sufficient signal-to-noise ratio.	17
2.1	Existing bounds and expected spectra for some of the cosmological models (Section 2.1.1, Section 2.1.3). The pulsar limit shown in this plot comes from the long time observation of timing variations in a set of pulsars as mentioned in Section 1.3.	27
2.2	The above figure shows different coordinate systems and angles referred in Section 2.2. For the calculation in Section 2.2, we assume $\psi = 0$	29
2.3	The above figure shows overlap reduction functions for colocated, coaligned H1-H2 LIGO detector pair as well as non-colocated and differently oriented H1-L1 LIGO detector pair.	34

- 2.4 Coherence Γ_{12} between H1 and L1 computed in the frequency band 40–512 Hz using all of the S5 data, for three different frequency resolutions: 1 mHz, 10 mHz, and 100 mHz (top-to-bottom). Plots on the left show Γ_{12} as a function of frequency while plots on the right show distribution of Γ_{12} . The distribution of Γ_{12} is expected to follow an exponential distribution for Gaussian noise. Here ‘accepted’ refers to the frequencies that were used for calculating Y_{final} 42
- 2.5 Coherence Γ_{12} between H2 and L1 computed in the frequency band 40–512 Hz using all of the S5 data, for three different frequency resolutions: 1 mHz, 10 mHz, and 100 mHz (top-to-bottom). Plots on the left show Γ_{12} as a function of frequency while plots on the right show distribution of Γ_{12} . The distribution of Γ_{12} is expected to follow an exponential distribution for Gaussian noise. Here ‘accepted’ refers to the frequencies that were used for calculating Y_{final} 43
- 2.6 Histogram of the fluctuations of the estimator Y_I over segments I around the mean, normalized by the standard deviation σ_{Y_I} is shown in red (for the H1-L1 pair). The blue curve shows the Gaussian fit to the histogram, which has zero mean and unit variance. The Kolmogorov-Smirnov test statistic (comparing the histogram and the fit) is 0.2 for H1-L1 (0.4 for H2-L1), indicating that the data is indeed Gaussian-distributed, and that the estimate of the theoretical variance $\sigma_{Y_I}^2$ is reliable. Figure published in [42]. 44
- 2.7 Stochastic signal simulations in hardware for H1-L1 (blue) and H2-L1 (red), and in software (H1-L1, green) are shown. The error bars denote 2σ ranges. Figure published in [42]. 45
- 2.8 Signal-to-noise ratio for the recovery of a software simulation with H1-L1 data with $\Omega_0^{simulated} = 3.8 \times 10^{-5}$ is shown as a function of the time-lag between the two interferometers. The inset shows the zoom-in around zero-lag: the signal is recovered well for zero-lag (SNR ≈ 7.2), but it disappears quickly with time-lag of ± 30 ms. Figure published in [42]. 46

- 2.9 $Y(f)$ and $\sigma(f)$ obtained by combining the H1-L1 and H2-L1 data from the S5 run. The inset shows that the ratio of the two spectra is consistent with a Gaussian of zero mean and unit variance. Figure published in [42]. 47
- 2.10 90% confidence upper limit is shown as a function of the power index α for several LIGO results: based on the previous runs S3 and S4 and the S5 result presented here. Figure published in [42]. 48
- 2.11 The result shown here (LIGO S5) applies in the frequency band around 100 Hz, and is compared to the previous LIGO S4 result [7] and to the projected Advanced LIGO sensitivity [71] in this band. The indirect bounds due to BBN [112, 18] and CMB and matter power spectra [153] apply to the integral of $\Omega_{\text{gw}}(f)$ over the frequency bands denoted by the corresponding dashed curves. Projected sensitivities of the satellite-based Planck CMB experiment [153] and LISA GW detector [25] are also shown. Figure published in [42]. . . 49
- 2.12 The above figure shows the $\hat{w} - \hat{n}_t$ plane for $r = 0.1$. The regions excluded by the BBN [47], LIGO, and pulsar [126] bounds are above the corresponding curves (the inset shows a zoom-in on the central part of the figure). The BBN curve was calculated in [32]. We note that the CMB bound [153] almost exactly overlaps with the BBN bound. Also shown is the expected reach of Advanced LIGO [71]. Figure published in [42]. 50
- 2.13 The above figure shows how different experiments probe the $\epsilon - G\mu$ plane for a typical value of $p = 10^{-3}$ [167] (p is expected to be in the range $10^{-4} - 1$). The excluded regions (always to the right of the corresponding curves) correspond to the S4 LIGO result [7], current result, BBN bound [18, 47], CMB bound [153], and the pulsar limit [126]. In particular, the bound presented here excludes a new region in this plane ($7 \times 10^{-9} < G\mu < 1.5 \times 10^{-7}$ and $\epsilon < 8 \times 10^{-11}$), which is not accessible to any of the other measurements. The entire plane shown here will be accessible to Advanced LIGO [71] SGWB search. Figure published in [42]. 51

- 2.14 The above figure shows the $f_1 - \mu$ plane for a representative value of $f_s = 30$ Hz in Pre-Big-Bang models. Excluded regions corresponding to the S4 result and to the result presented here are shaded. The regions excluded by the BBN [18, 47] and the CMB [153] bounds are above the corresponding curves. The expected reaches of the Advanced LIGO [71] and of the Planck satellite [153] are also shown. Figure published in [42]. 52
- 2.15 Coherence Γ_{12} between H1 and H2 computed in the frequency band 80–160 Hz using all of the S5 data, for three different frequency resolutions: 1 mHz, 10 mHz, and 100 mHz (top-to-bottom). Plots on the left show Γ_{12} as a function of frequency while plots on the right show distribution of Γ_{12} . The distribution of Γ_{12} is expected to follow an exponential distribution for Gaussian noise. Here 'accepted' refers to the frequencies that were used for further analyses. 57
- 2.16 Left panel: The inverse Fourier transform of $\hat{\Omega}_0(f)$ for an $\text{SNR}_{\Omega_0} \approx 15$ software signal injection in the H1-H2 data with $\Omega_0 = 1.10 \times 10^{-5}$. Note that the signal decoheres on a time-scale of order 10 ms, which justifies the ± 1 s time-shifts used to identify noise correlations in the time-shift method. Right panel: Recovered amplitudes for 10 software injection trials, along with $\pm \sigma_{\hat{\Omega}_0}$ error bars. The injected signal, denoted by the dashed line, in each case was $\Omega_0 = 1.10 \times 10^{-5}$ 59
- 2.17 Plots of $\hat{\Omega}_0(f)$ and $\hat{\Omega}_{0,\text{PEM}}(f)$ (left), and the inverse Fourier transform of $\hat{\Omega}_0(f)$ (right) for the 80–160 Hz band after various stages of noise removal were applied to the data. The four rows correspond to four different stages of cleaning defined in Table 2.1. 62

2.18	The above figure shows upper limits from current/past SGWB analyses, as well as indirect limits from Big Bang Nucleosynthesis (BBN), and projected limits using Advanced LIGO. Indirect limits from BBN apply to SGWBs present in the early universe at the time of BBN, but not to SGWBs of astrophysical origin created more recently. The $\alpha = 3$ bound on astrophysical SGWB presented here improves on the previous best limit by a factor of $>350x$. It complements the indirect bound from the BBN, which is only sensitive to cosmological SGWBs from the early universe, as well as direct $\alpha = 0$ measurements using lower-frequency observation bands [14].	63
3.1	An example ft-map of $\text{SNR}(t; f, \hat{\Omega})$ using simulated data with with $T = 4$ sec and $\delta F = 0.25$ Hz resolution (see (3.10)).	70
3.2	Distribution of $\text{SNR}(t; f, \hat{\Omega})$ for the case of $4\text{ s} \times 0.25\text{ Hz}$ size pixels with Monte Carlo data. For this plot we used 2 neighboring segments to calculate $\hat{\sigma}_Y(t; f, \hat{\Omega})$	79
3.3	Histogram of $\text{SNR}(t; f, \hat{\Omega})$ using $52\text{ s} \times 0.25\text{ Hz}$ pixels comparing S5 data with an unphysical time-shift (blue) to Monte Carlo data (red) and a normal distribution with mean = 0 and $\sigma = 1$ (black). Here we used 2 neighboring segments to calculate $\hat{\sigma}_Y(t; f, \hat{\Omega})$. Figure taken from [159].	80
3.4	GW strain amplitude spectrum due to PNS convection in an axisymmetric PNS model at a typical galactic distance of 10 kpc [124]. This plot was generated using the data simulated in [124] available at [123]. Figure published in [159].	81

3.5 PNS signal injection and recovery using with the box-search algorithm. Top-left: an ft -map of $\hat{Y}(t; f, \hat{\Omega})$. The injected signal (not visible by eye) is indicated with a green arrow. Top-right: an ft -map of $\text{SNR}(t; f, \hat{\Omega})$. The injected signal (not visible by eye) is indicated with a black arrow. Bottom-left: a histogram of SNR_Γ for a $200 \text{ Hz} \times 12 \text{ s}$ box. The blue dashed line corresponds to the injection. Though the signal is weak in each pixel, the signal obtained by combining every pixel in Γ is large. Bottom-right: \hat{Y}_Γ as a function of time. Figure published in [159]. 82

3.6 Top-left: a 400 s-duration map of $\text{SNR}(t; f)$ (see Eq. (3.10)) created with $4 \text{ s} \times 0.25 \text{ Hz}$ pixels and using s_{GW} cross-correlated with a microphone. The slightly curved track on the right side of the plot is caused by the Doppler-shifted acoustic signal from a passing airplane. Top-right: the associated Radon map. Note the bright spot on the mid-right corresponding to the airplane track. Bottom-left: ft -map of the reconstructed track using the maximum $\text{SNR}(t; f)$ pixel in Radon space. Bottom-right: ft -map of the magnitude of $\text{SNR}(t; f)$ including a black line corresponding to the veto window. These data are from the beginning of LIGO's S5 science run. . Figure taken from [159]. 84

3.7 Injection and recovery of ADI signals using burst cluster algorithm. The plot on the left shows an ADI injection in timeshifted H1-L1 data and the plot on the right shows the recovery of largest cluster using burst cluster algorithm. . 87

3.8 Left panel: Distribution of largest cluster SNRs using both simulated and time-shifted H1-L1 data. Right panel: Recovered largest cluster (median) SNR as a function of distance to an ADI signal (injected in timeshifted H1-L1 data). 88

- 4.1 An earthquake data showing the arrival of P, S and surface waves. The above plot was made using data from the 2000ft-A station. This event corresponds to a 5.6 earthquake occurred in N. California on February 13, 2012 at a depth of 33 km. 93
- 4.2 The above figure is a pictorial depiction of Newtonian noise. At low frequencies, the variations in the heights of Earth’s surface produces a considerable gravitational pull on the suspended mirrors of GW detectors mimicking the effect of GWs. 94
- 4.3 Expected strain sensitivity for advanced LIGO GW detectors. This plot was produced by Gravitational Wave Interferometer Noise Calculator (GWINC) using advanced LIGO configuration [87]. 95
- 4.4 The above figure is a cross-sectional (top) view of the mine showing the locations of the seismic stations. The blue circles and blue star correspond to currently operating stations. The station at 4100-ft level marked by a star is the new station built to be away from the plane of the other stations. The map is aligned with cardinal directions (top is North). 95
- 4.5 Above photo, taken during the construction of 4100ft-D station, shows the two hut setup used for isolating seismometers and data acquisition systems. 96
- 4.6 Internal view of the data read-out system. The boards that are not labeled are used for providing DC power. 97
- 4.7 Timing plot of ~ 100 data files from 4100D-ft station. The blue curve is the time assigned to each of those files (adjusted for expected increase) by the Dreamplug and red curve is the linear fit. We see that the variation of the blue curve is of the order of 0.1 msec. 99
- 4.8 A photo of the 4100ft-A station showing the complete data acquisition setup. It is the only station where the data acquisition is set up in a natural cave like chamber. The seismometer is behind the the wall shown here. 99

4.9	Seismic spectrum showing the reduction in high frequency noise (1 – 10 Hz) with depth. At 1 Hz we observe almost 10× reduction at 4100 ft as compared to the 300 ft depth, which is consistent with theoretical expectations for suppression of surface seismic waves with depth.	100
4.10	Plots of square (left) and spiral array (right), each consisting of 25 seismometers, used for 2D simulations.	107
4.11	Simulation and recovery of single Rayleigh wave source using four different beamforming methods. For this simulation, we used a square array of 25 stations on the surface. The black marker shows the intended simulation location and the color indicates the likelihood of recovery (‘red’ corresponds to highly likely). We find that there is strong aliasing in all the four cases. . .	108
4.12	Simulation and recovery of single Rayleigh wave source using four different beamforming methods. For this simulation, we used a spiral array of 25 stations on the surface. The black marker shows the intended simulation location and the color indicates the likelihood of recovery (‘red’ corresponds to highly likely).	109
4.13	Simulation and recovery of four Rayleigh wave sources using four different beamforming methods. For this simulation, we used a spiral array of 25 stations on the surface. The black markers show the intended simulation locations and the color indicates the likelihood of recovery (‘red’ corresponds to highly likely).	110
4.14	3D simulation and recovery of two P-wave wave sources using four different beamforming methods. For this simulation, we used 49 stations randomly distributed in a 16 km ³ volume. The boxes show the intended simulation locations and the color indicates the likelihood of recovery (‘red’ corresponds to highly likely). Due to computational (memory) problem, GW radiometer method was performed using coarser resolution.	112

4.15	Recovery of simulated P and R-waves using corresponding filters. The P-wave was placed underground and R-wave on the surface ($\theta = 0$). The top plot uses P-wave filter and the bottom plot uses R-wave filter.	113
A.1	The above figure shows different coordinate systems and angles involved in the calculation of strain induced in GW detectors. For unpolarized signals, we assume $\psi = 0$	134
A.2	Distribution of Y (Eq. (A.39)) for Gaussian data.	142
A.3	Distribution of P_{adj} (Eq. (A.42)) using simulated data.	143
A.4	Distribution of σ_Y (Eq. (A.43) using simulated data).	144
A.5	Distribution of $\text{SNR}(t; f, \hat{\Omega})$ using simulated data (for $N = 2$).	145

Chapter 1

Gravitational waves: Sources and Detectors

In 1905, the year now called *Annus Mirabilis*, Albert Einstein published four seminal papers that laid the foundation for a new era in modern physics [61]. In one of the papers on electrodynamics of moving bodies, widely known as the special theory of relativity, he showed that space and time are not distinct but are intermingled as *spacetime* and there is no universal reference frame in which space and time are absolute. This axiomatic theory of relativity was based on two assumptions which were that, (i) the speed of light in vacuum is constant and is the maximum speed limit; and (ii) physical laws are same in every inertial reference frame. The special theory of relativity made many new predictions and all of them were confirmed by experiments. Hence it became necessary for other physical theories to comply with the special theory of relativity. Newton's law of gravitation, then accepted theory of gravity, relied on a universal time and required action-at-a-distance (i.e., force with infinite speed) and hence was in contradiction with the special theory of relativity. Newton's theory was not completely wrong, since it was able to make observable predictions, only that it seemed to be an approximate theory of a more fundamental one.

After eleven years of struggle to generalize special relativity to non-inertial frames involving gravity, in 1916 Einstein formulated a new theory called general relativity which, under certain conditions, reduced to Newton's theory of gravity as expected. The new theory was able to explain various existing observations such as perihelion precession of Mercury and also made new predictions such as gravitational redshift of light that were confirmed

later [116]. Today, after nearly a century of observations, it still stands unchallenged and is considered one of the pillars of modern physics.

In general relativity, gravity manifests as curvature of spacetime and gravitational force is seen as the response of objects to this curvature. This description is well captured by J. Wheeler’s phrase [116]

“Mass tells spacetime how to curve, and spacetime tells mass how to move.”

Similar to the electromagnetic field, this ‘field’ of curvature could be static or time-varying. The static curvature is equivalent to the well-known Newtonian gravity while the time-varying curvature with finite propagation speed, equal to the speed of light, was a new prediction of general relativity. These perturbations of spacetime can carry energy from one place to another and are called gravitational waves (GWs).

Similar to other types of waves, the frequency and amplitude of GWs are highly dependent on their source characteristics. In general, the larger the mass the higher the amplitude and larger the size the smaller the frequency (see Eqs. (1.18) and (1.19)). More so than other forms of radiations such as photons or neutrinos, GWs interact very weakly with matter and hence can travel long distances without scattering. This makes GWs a strong candidate for studying objects, such as black holes, that are far away and/or difficult to detect with other radiations. In this chapter, we briefly revisit general relativity as it applies to GWs, examine GW signals from some of the astrophysical and cosmological sources, and assess the prospects of their detection using current and future generations of GW detectors.

1.1 Gravitational waves in general relativity

In this section we show how the frame work of general relativity predicts the existence of GWs. The derivation given here follows a similar line of arguments as most text books on this subject [116, 143]. The Einstein field equation that connects spacetime geometry to mass-energy content is

$$G_{\mu\nu} = \frac{8\pi G}{c^4} T_{\mu\nu} , \quad (1.1)$$

where $G_{\mu\nu}$ is the Einstein tensor, $T_{\mu\nu}$ is the stress-energy tensor, G is Newton's constant, and c is speed of light. Here the Greek indices μ and ν run from 0 to 3, corresponding to one time index (t) and three spacial indices (x, y, z). We use this convention for all Greek indices throughout the chapter, unless stated otherwise. The Einstein tensor describes the curvature of space-time and the stress-energy tensor represents the mass-energy content that produces the curvature (analogous to the source term in electromagnetism). The constant prefactor of $\frac{8\pi G}{c^4}$ is chosen such that Eq. (1.1) reduces to Newton's law of gravitation when the gravitational field is weak and the velocities involved are much less than the speed of light.

In special relativity, the infinitesimal "distance" $d\tau$, also called *proper distance*, between two events separated by dx^μ is given by

$$d\tau^2 = dx^\mu \eta_{\mu\nu} dx^\nu , \quad (1.2)$$

where $\eta_{\mu\nu} = \text{diag}(-1, 1, 1, 1)$ is the Minkowski metric tensor. In Eq. (1.2), we sum over indices μ and ν (any repeated index means summing over it). In general relativity, where the spacetime metric tensor is represented by $g_{\mu\nu}$ which need not be as simple as $\eta_{\mu\nu}$, we replace $\eta_{\mu\nu}$ in Eq (1.2) with $g_{\mu\nu}$. Einstein tensor $G_{\mu\nu}$ is a function of the metric tensor $g_{\mu\nu}$ and given by,

$$G_{\mu\nu} = R_{\mu\nu} - \frac{1}{2}R g_{\mu\nu} , \quad (1.3)$$

where

$$R = g^{\mu\nu} R_{\mu\nu} . \quad (1.4)$$

Here $R_{\mu\nu}$ is the Ricci tensor and R is the Ricci scalar. Both $R_{\mu\nu}$ and R are functions of $g_{\mu\nu}$ and are used to simplify the complex form of $G_{\mu\nu}$ and Eq. (1.1).

1.1.1 Weak field limit

Since we are interested in the wave behavior of the perturbations, let's look at the Einstein equation in a small amplitude regime i.e., in *weak field limit*. In the weak field limit, the

metric tensor can be written as

$$g_{\mu\nu} = \eta_{\mu\nu} + h_{\mu\nu}, \quad (1.5)$$

where $\eta_{\mu\nu}$ is the flat Minkowski metric and $|h_{\mu\nu}| \ll 1$. In this limit, to first order in $h_{\mu\nu}$, the Ricci tensor $R_{\mu\nu}$ is

$$R_{\mu\nu} = \frac{1}{2} \left(h_{\mu,\nu\alpha}^{\alpha} + h_{\nu,\mu\alpha}^{\alpha} - h_{\mu\nu,\alpha}^{\alpha} - \eta^{\alpha\beta} h_{\alpha\beta,\mu\nu} \right). \quad (1.6)$$

In the above equation [,] represents partial derivative i.e., $A_{\mu\nu,\alpha} = \partial_{\alpha} A_{\mu\nu}$. Using Eqs. (1.3), (1.6) and a modified $h_{\mu\nu}$ (trace-inversed $h_{\mu\nu}$) given by

$$\bar{h}_{\mu\nu} = h_{\mu\nu} - \frac{1}{2} \eta_{\mu\nu} h^{\gamma}_{\gamma}, \quad (1.7)$$

the Einstein tensor can be written as,

$$G_{\mu\nu} = -\frac{1}{2} \left(\bar{h}_{\mu\nu,\alpha}^{\alpha} + \eta_{\mu\nu} \bar{h}_{\alpha\beta}^{\alpha\beta} - \bar{h}_{\mu\alpha,\nu}^{\alpha} - \bar{h}_{\nu\alpha,\mu}^{\alpha} \right). \quad (1.8)$$

Applying the Lorentz gauge condition, provided by the invariant requirement on $x^{\alpha} \rightarrow x^{\alpha} + \xi^{\alpha}(x^{\beta})$,

$$\bar{h}^{\mu\alpha}_{,\alpha} = 0, \quad (1.9)$$

the Einstein tensor becomes

$$G_{\mu\nu} = -\frac{1}{2} \bar{h}_{\mu\nu,\alpha}^{\alpha}. \quad (1.10)$$

1.1.2 Plane wave solutions

In free space with $T_{\mu\nu} = 0$ and in the weak field limit, the Einstein field equation Eq. (1.1) becomes

$$-\frac{1}{2} \square \bar{h}_{\mu\nu} = 0, \quad (1.11)$$

where \square corresponds to the *D'Alembert* operator ∂_α^α . Eq. (1.11) is a wave equation for $\bar{h}_{\mu\nu}$ and the simplest plane wave solutions of Eq. (1.11) are

$$\bar{h}_{\mu\nu} = \text{Re} \left[A_{\mu\nu} e^{ik_\alpha x^\alpha} \right], \quad (1.12)$$

where $A_{\mu\nu}$ and k_α are the wave amplitude and the wave vector of the plane waves respectively. Any general solution can be written as a linear combination of these plane waves.

Applying the Lorentz gauge condition given by Eq. (1.9) and an additional condition of trace of $\bar{h}_{\mu\nu}$ to be zero (since the Lorentz gauge condition does not uniquely fix the coordinate transformation), for a wave traveling in the z -direction, we get

$$\bar{h}_{\mu\nu}^{(TT)} = \begin{pmatrix} 0 & 0 & 0 & 0 \\ 0 & \bar{h}_{xx}^{(TT)} & \bar{h}_{xy}^{(TT)} & 0 \\ 0 & \bar{h}_{xy}^{(TT)} & -\bar{h}_{xx}^{(TT)} & 0 \\ 0 & 0 & 0 & 0 \end{pmatrix} e^{i\omega(t-z/c)}, \quad (1.13)$$

where ω is the angular frequency of the wave. This gauge, combination of Lorentz gauge and traceless condition, is called Transverse Traceless (TT) gauge. In this gauge $\bar{h}_{\mu\nu}^{(TT)} = h_{\mu\nu}^{(TT)}$, and so we henceforth drop the bar on $\bar{h}_{\mu\nu}$. We can also redefine $h_{\mu\nu}^{(TT)}$ as,

$$h_{\mu\nu}^{(TT)} = (e_+ h_+ + e_\times h_\times) e^{i\omega(t-z/c)} \quad (1.14)$$

where $h_+ = h_{xx}^{(TT)}$, $h_\times = h_{xy}^{(TT)}$ and,

$$e_+ = \begin{pmatrix} 0 & 0 & 0 & 0 \\ 0 & 1 & 0 & 0 \\ 0 & 0 & -1 & 0 \\ 0 & 0 & 0 & 0 \end{pmatrix}, \quad e_\times = \begin{pmatrix} 0 & 0 & 0 & 0 \\ 0 & 0 & 1 & 0 \\ 0 & 1 & 0 & 0 \\ 0 & 0 & 0 & 0 \end{pmatrix}. \quad (1.15)$$

The tensors e_+ and e_\times correspond to two polarization states of a GW traveling in the z -direction.

1.1.3 Effect of GWs on the distance between free masses

Let's look at the effect of these waves on the distance between two free masses. The (proper) distance between two free masses at $x = 0$ and $x = \epsilon$ is obtained by integrating Eq (1.2) (after replacing $\eta_{\mu\nu}$ by $g_{\mu\nu}$) as below,

$$\begin{aligned}
 \Delta_\epsilon &= \int_0^\epsilon |d\tau|^{1/2} \\
 &= \int_0^\epsilon |g_{\mu\nu} dx^\mu dx^\nu|^{1/2} \\
 &= \int_0^\epsilon |g_{xx}|^{1/2} dx \simeq |g_{xx}(x=0)|^{1/2} \epsilon \\
 &\simeq \left[1 + \frac{1}{2} h_{xx}^{(TT)}(x=0) \right] \epsilon .
 \end{aligned} \tag{1.16}$$

Here we have used the long wavelength approximation, i.e., the wavelength of the GW is much larger than the distance ϵ , in step 3. From Eq. (1.16), we see that the distance between two free masses changes as GWs pass by. This effect can be used to detect GWs and is the basis for GW detectors. In Eq. (1.16) the magnitude of $h_{xx}^{(TT)}$ represents the fractional change in the distance between free masses, $\frac{\delta\epsilon}{\epsilon}$, also called *strain*. This identification of h with strain is used in the rest of this chapter and other chapters. For a distance change of 10^{-15} m (\sim size of proton) and an initial separation of 1 km, this corresponds to $h = 10^{-18}$ while the most optimistic astrophysical sources are expected to produce strain at the level of 10^{-21} !

1.2 Gravitational wave sources

In the previous section we derived the plane wave solutions Eq. (1.12) by setting the source term $T_{\mu\nu}$ to zero. This is fine for studying nature of the perturbations and their propagation properties. However, for generating GWs we need to add the source term. For a source with a quadrupole moment $I_{\mu\nu}$, the perturbations $h_{\mu\nu}$ are given by [116]

$$h_{\mu\nu} = \frac{2G}{c^4 r} \ddot{I}_{\mu\nu} . \tag{1.17}$$

For a simple system of two masses (each of mass M) separated by a distance $2R$ and rotating at a frequency f , the strain produced by GWs at a distance r is given by [140]

$$h(t) \approx \frac{2G^2 M^2}{c^4 r R} \cos(4\pi f t), \quad (1.18)$$

where

$$f \sim \left(\frac{3GM}{4\pi R^3} \right)^{1/2}. \quad (1.19)$$

Applying Eq. (1.18) for a laboratory set up with $M = 10$ kg, $R = 10$ m, $f = 10$ Hz and $r = 10$ m, we get $h \sim 10^{-38}$ which is too small to measure with current GW detectors. All terrestrial sources produce h on a similar scale and hence cannot be detected at this time. However for astrophysical sources, such as binary neutron stars, this number can be as big as 10^{-21} (a number that can be feasibly measured with current GW detectors) and hence can be detected.

There are various astrophysical sources that can produce GWs [44, 159, 37, 130, 162]. These sources can be classified into two broad categories depending on the GW signals they produce: (i) signals that can be modeled easily and (ii) signals that are hard to model. This classification is inspired by the data analysis tools that are used to detect GW signals. In general, if we know the waveform of a signal, we can use optimal matched filtering techniques [88] to extract it from within the detector noise. However, if we don't know the waveform, then there is no unique technique available and we have to use tools that suit to the specific scenario; for example, in case of strong GW signals, we can look for excess power above the detector noise level. In most cases, we will have some partial information about the signal which can be folded into analysis tools to improve the sensitivity [159].

1.2.1 Sources with known signal model

There are only a few sources for which we can construct signal models with relatively good accuracy. Isolated, spinning neutron stars with spherical asymmetry, binary systems consisting of two compact objects such as two neutron stars (BNS), one black hole and one neutron star (BH-NS) or two black holes (BBH) are examples of such sources. For a large part of

their life, these sources are expected to produce slowly varying sinusoidal GW signals [95].

Binary of compact objects

According to Eq. (1.18), a rotating binary system (BNS, BH-NS, BBH) is expected to emit GWs. Initially when the two objects are far away from each other, the GW signal is expected to be nearly monochromatic with a frequency twice that of the orbital frequency of the binary and an amplitude given by Eq. (1.18). Since GWs carry away energy (Eq. (1.18) gives the instantaneous strain), the orbit of the binary system will shrink which in turn will increase the frequency as well as the amplitude and eventually leading to the *merger* of the two objects. The *inspiral* phase leading up to the merger can be well modeled using post-Newtonian (PN) approximations [48]. The corresponding GW signals are known as compact binary coalescence (CBC) signals. Even though the inspiral phase lasts for most of the binary's lifetime (millions of years), the part of inspiral phase that could be detected with the current generation of GW detectors is just the last few minutes before the merger (corresponding to ~ 10 Hz - a few kHz GW signal). The long, low frequency part of the inspiral phase (< 10 Hz) is undetectable due to the high (seismic) noise level at those frequencies, at least in the current generation of GW detectors. Using Eq. (1.18) for a BNS with two $1.4M_{\odot}$ neutron stars at 1 Mpc distance and emitting GW signal at 1 kHz we get strain at the level of 10^{-21} . Figure 1.1 shows an example of CBC waveform. The merger phase is also expected to emit GWs, but the signal is expected to be messy and hard to model. After the merger, in the case of BBH, there is also possibility of a *ringdown* phase in which the newly formed black hole can undergo quasi-normal mode oscillations producing GWs, which can be modeled well [53].

Isolated neutron stars

Isolated, rotating neutron stars with spherical asymmetry can also produce monochromatic, sinusoidal GWs. The asymmetry could arise either during the formation of the neutron star or later due to accretion of material surrounding the neutron star [28]. Also, in case of neutrons stars with high magnetic field (i.e., pulsars), a difference in their magnetic and

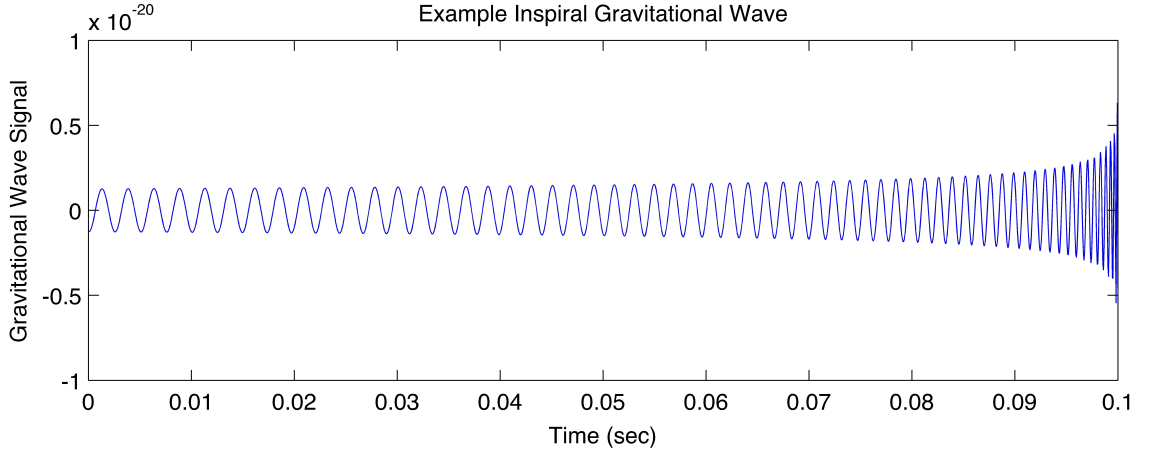


Figure 1.1: An example waveform showing the inspiral part of GW signal from a coalescing binary. The y-axis corresponds to instantaneous strain amplitude of the GW signal. Image from [109].

rotational axes can build up asymmetry [46]. The deviation from symmetry is measured by *ellipticity* ϵ which is given by

$$\epsilon = \frac{I_{xx} - I_{yy}}{I_{zz}}, \quad (1.20)$$

where I_{xx} , I_{yy} and I_{zz} are moments of inertia along the principle axes and z is the axis of rotation. The amplitude of GWs from such a system will be proportional to ϵ and given by,

$$h = \frac{4\pi^2 G}{c^4} \frac{I_{zz} f^2 \epsilon}{r} \quad (1.21)$$

where r is the distance to the neutron star and f is twice the spin frequency of the neutron star. For a neutron star of mass $1.4 M_{\odot}$, radius 10 km, $\epsilon = 10^{-6}$, $f = 1$ kHz and at a distance of 1 kpc, we get $h \sim 10^{-24}$.

1.2.2 Sources with unknown signal model

In many of the astrophysical systems, either the system itself or its environment is not well understood. This translates into uncertainty of the signal waveform we are trying to construct. Even in the case of well understood systems such as binary compact objects, the

impact of its surroundings (for example presence of a large accretion disc) on the evolution of the system can be very significant and can change the expected signal waveform. The GW signals in such cases could be classified into either bursts (short transients) lasting up to a few minutes or long-lived lasting from a few minutes to forever.

Burst GW sources

As we saw in Section 1.2.1, the merger phase of binary compact objects could produce GW signals that are hard to model. These signals in general are expected to be short (\sim seconds) and to have large amplitudes ($\sim 10^{-21}$) [95]. The other possible sources include asymmetric core collapse of massive stars known as *collapsars*, various instabilities produced by the accretion of materials onto a neutron star, pulsar glitches [161, 130, 37, 160], etc.. Since it is hard to model these cases (or requires intensive computer simulations), we can use energy based arguments to deduce the expected strength of GWs from these sources. The energy carried by GWs is proportional to $\langle \dot{h}_{\mu\nu}^{(TT)} \dot{h}^{(TT)\mu\nu} \rangle$ and using this one can derive a strain-energy relation [140] given by,

$$h \sim \frac{1}{\pi f r} \sqrt{\frac{GE}{tc^3}}, \quad (1.22)$$

where E is the expected energy emitted in GWs, t is the duration of GW signal, f is the frequency of GW signal, and r is the distance to the source. For optimistic values of $E = 0.01 M_{\odot}$, $f = 1$ kHz, $t = 1$ sec and $r = 1$ kpc, we get $h \sim 2 \times 10^{-21}$.

Long-lived GW sources

Under certain conditions, most of the sources listed under burst sources can also produce long duration GWs. There are also other sources such as gamma-ray bursts (GRBs), black holes with large accretion discs that could produce long GW transients [124, 45, 130, 162]. The detailed mechanisms for some of these sources are given in Chapter 3, in which we deal with the detection of such GW signals.

The other prominent source that comes under this category is not a single source, but

an ensemble of the aforementioned sources. Even if the individual GW signal can be well modeled, the incoherent combination of signals from a large number of such sources can be hard to model. Such superposition of many unresolved GW signals is called stochastic GW background (SGWB). The sources could be from the early universe related to inflation [83, 151], electroweak phase transition [65], cosmic strings [167, 148], or recent astrophysical sources such as binary neutron stars [35], magnetars [136], rotating neutron stars [135]. More on these sources can be found in Chapter 2.

1.3 Gravitational wave detectors

Since the amplitudes of GWs, even from the most optimistic sources, are expected to be very small, there has as yet been no direct detection of GWs. There are however indirect pieces of evidence coming from the observations of orbital decay of several close binary systems [165, 60]. As pointed out in Section 1.2.1, the emission of GWs decreases the orbit of a binary and hence by measuring the rate of decay we can estimate the energy emitted in GWs. The Hulse-Taylor pulsar system (PSR B1913+16) is an example of such close binary system. The observed orbital decay of the binary system PSR B1913+16, which has been observed for the past ~ 35 years, is within 1% of the value predicted by just the emission of GWs.

In Section 1.1.3 we noted that GWs, characterized by simple plane waves, change the distance between free masses and it can be used to detect them on Earth. Currently, there are two kinds of popular detectors in operation: (i) resonant mass detectors and (ii) interferometric detectors. Most of the resonant mass detectors are made up of a large metal bar with piezoelectric sensors attached at the ends [17]. Other configurations such as spheres are also used [69]. When a GW passes through the bar with a frequency equal to the resonance frequency of the bar, it will excite vibrations in the bar which can be read out from the piezoelectric sensors. Since resonance mass detectors rely on the resonance of the bar, which happens only for a narrow frequency range, these types of detectors are considered narrowband detectors (\sim kHz). In 1962, Joseph Weber built the first resonance

bar detector, which was also the first GW detector of any kind, starting a new era of GW detectors [164].

Interferometric detectors are based on large scale Michelson interferometers. Since GWs produce alternate stretching and shrinking of spatial dimensions perpendicular to the direction of their propagation, and interferometers are sensitive to differential change in their perpendicular arms, interferometric GW detectors are well suited for this measurement. Because they measure the actual change in the distance as compared to the resonance nature of bar detectors, interferometric detectors are broadband and are sensitive to all GW frequencies and only limited by local and instrumental noise sources. However, this is only true for simple Michelson interferometers. In reality, the interferometric detectors employ various resonant cavities to improve their efficiency which in turn reduces their bandwidth [12].

Apart from these two types of detectors, there is also the pulsar timing array approach that uses variations in light arrival time from a pulsar, which could happen due to passage of GWs between the pulsar and Earth, to detect GWs [75]. This is also a narrowband GW detection method ($\sim 10^{-7}$ Hz). Since all the analyses done in this thesis use data from interferometric detectors, henceforth we concentrate only on the interferometric detectors.

1.3.1 Interferometric detectors

In 1972, Rainer Weiss at MIT published a detailed report on the possibility of interferometric broadband GW detectors with sensitivities comparable to or exceeding then existing resonance mass detectors. Based on that and other related studies, during 1980's and 1990's several 1 \sim 40 m scale interferometric GW detectors were constructed and used for GW detection. These small scale detectors also served as the prototypes for next generation large scale detectors. With the experience gained from those small scale detectors and with the use of latest technologies, several kilometer scale ground-based interferometric GW detectors were constructed during last two decades. The Laser Interferometer Gravitational-Wave Observatory (LIGO), a US collaboration, has built two 4 km and one 2 km interferometric detectors [12]; two in Hanford, WA and one in Livingston, LA. Similarly other collaborations around the world such as VIRGO [67] in Italy, GEO [85] in Germany, and TAMA [155] in

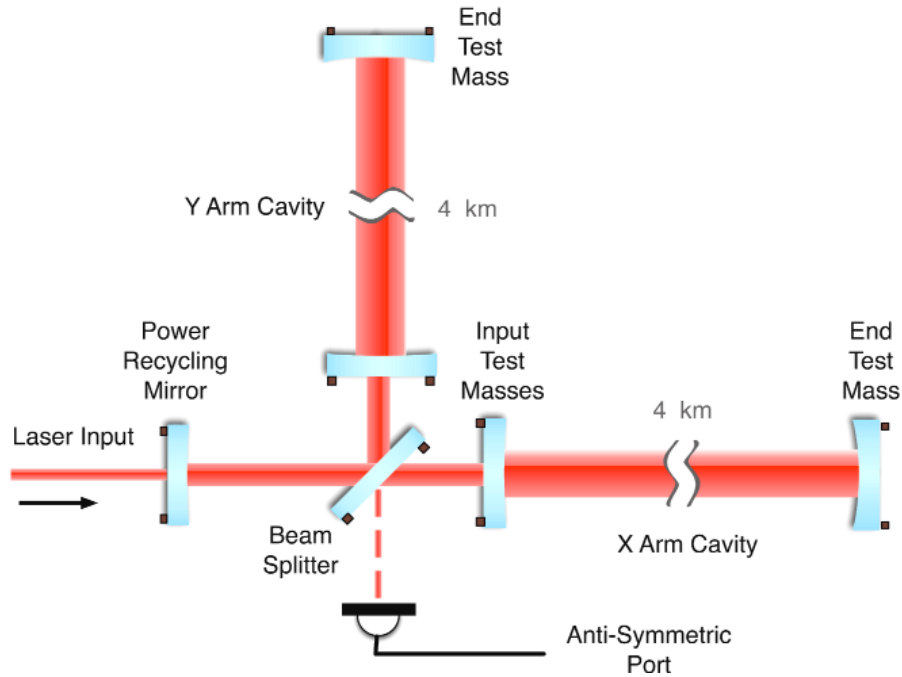


Figure 1.2: An outline of interferometric GW detector. Image from [68].

Japan have built kilometer scale interferometers.

Figure 1.2 shows an outline of a typical interferometric GW detector. The interferometer relies on a powerful laser beam to measure the differential change in the two arms. The initial laser beam is split into two halves by a beam splitter. The two new beams then propagate in the orthogonal arms, reflect off of suspended mirrors (which act as free masses) at the end of the arms, and are recombined at the beam splitter. The light passing through the beam splitter exits to what is known as the anti-symmetric port and impinges on a photodiode. If a GW passes through the detector, it will effectively change the positions of the end mirrors and hence the distances traveled by the two laser beams. Consequently it will produce intensity fluctuations in the recombined laser beam, at the photodiode. By measuring the size of these intensity fluctuations we can determine the amplitude of GWs. Since GWs only affect free masses, all the mirrors in the interferometer are suspended with a low resonance frequency so that at high frequencies they can be considered as “free” masses. Also, to increase the efficiency of the detector various optical cavities are set up

in the interferometer. A Fabry-Perot cavity is set up between the beam splitter and the end mirrors to increase the storage time of photons in the arms, effectively increasing the arm lengths (which correspond to increase in the strain sensitivity). There is also a power recycling cavity to increase the total power in the interferometric arms (strain sensitivity around ~ 100 Hz is proportional to the power in the arms). There are various noise sources that can limit the sensitivity of an interferometer. The main noise sources are shot noise, seismic noise and thermal noise which basically limit the sensitivity at high frequencies, low frequencies and frequencies in the middle, respectively.

Shot noise and radiation pressure noise

The differential distance between two arms of the interferometer is obtained by measuring the intensity of light at the photodiode. Because of the discrete nature of light, this is also equivalent to measuring the number of photons arriving at the photodiode. Since the ‘arrival’ of a photon is probabilistic, the measured number of photons N in a time interval τ follows Poisson statistics and is given by

$$p(N) = \frac{\langle N \rangle^N e^{-\langle N \rangle}}{N!}; \quad \langle N \rangle = \frac{\lambda P_D \tau}{h_P c}, \quad (1.23)$$

where $\langle N \rangle$ is the mean number of photons arriving during interval τ , h_P is Plank’s constant, λ is the wavelength of the photon and P_D is the total power of measured by the photodiode. Fluctuations in the number of arriving photons translates into fluctuations in the phase difference between the light beams from the two arms, and the strain due to this noise can be written as [141]

$$h_{shot}(f) = \frac{1}{L} \sqrt{\frac{h_P c \lambda}{4\pi^2 P_{in}}}, \quad (1.24)$$

where L is length of each arm and P_{in} is input laser power. For typical values of $P_{in} = 10$ W, $\lambda = 1 \mu\text{m}$, $L = 4$ km, we get $h_{shot} \sim 5 \times 10^{-21}$. Eq. (1.24) tells us that by increasing the input power P_{in} we can reduce the shot noise. However as we increase the input power another noise, called radiation pressure noise, starts to dominate. Photons impinging on the mirrors will exert a force and will move the mirrors. This force, called radiation pressure, is

proportional to P_{in} . According to Poisson statistics Eq. (1.23) this force will fluctuate with the fluctuations proportional to $P_{in}^{1/2}$. For mirrors of mass M , the strain due to radiation pressure noise is [141]

$$h_{rad}(f) = \frac{1}{Mf^2L} \sqrt{\frac{h_P P_{in}}{4\pi^4 c \lambda}}. \quad (1.25)$$

Eq. (1.25) is valid only for frequencies above the resonance frequency of the mirror suspension. From Eqs. (1.24) and (1.25), a P_{in} can be chosen to minimize the quadrature sum of strains due to shot noise and radiation pressure noise. Here we note that the frequency independent shot noise expression (Eq. (1.24)) only applies to simple Michelson interferometers, interferometers without any resonant cavities. For interferometers with resonant cavities, which is case for LIGO interferometers, shot noise linearly increases with frequency.

Seismic Noise

Since the mirrors are suspended in a housing bolted to the ground, any ground motion would affect the mirrors and will introduce noise. The displacement of the mirrors due to ground motion above their resonance frequency f_0 is

$$x(f) \approx \frac{f_0^2}{f^2} x_g, \quad (1.26)$$

where x_g is the displacement of the housing due to ground motion. In general the mirror suspensions are made up of coupled pendulae with N stages, and hence the resulting displacement is given by

$$x(f) \approx \left(\frac{f_0^2}{f^2} \right)^N x_g. \quad (1.27)$$

In initial LIGO, most of the mirror pendula were hanged at the end of a four-stage passive isolation. The observed *quite* ground motion spectrum above ~ 1 Hz, in general, has the form,

$$x_g(f) \approx \frac{10^{-7}}{f^2} \text{m}/\sqrt{\text{Hz}}. \quad (1.28)$$

The combination of passive isolation and ground motion spectrum produces,

$$h_{seism}(f) \approx \frac{1}{f^{14}} 1/\sqrt{\text{Hz}}, \quad \text{for } f \gtrsim 10\text{Hz} \quad (1.29)$$

which at 100 Hz is $\sim 10^{-28}$, well below the expected strain from astrophysical sources. Apart from directly affecting the mirrors, the seismic field fluctuations can also introduce another noise called Newtonian noise which is further described in Chapter 4.

Thermal noise

There are several sources of thermal noise in an interferometric detector and the dominant one comes from the damping of the mirror pendulum due to thermal fluctuations in the suspension wires. At frequencies above the natural frequency f_0 of the mirror pendulum, strain due to suspension thermal noise [82] is given by,

$$h_{therm-sus}(f) \approx \left(\frac{k_B T f_0}{2\pi^4 M \tau f^5} \right)^{1/2}, \quad (1.30)$$

where τ is the free decay time of the natural oscillation at frequency f_0 , k_B is Boltzmann's constant, M mass of the mirror, and T is the effective temperature. Apart from suspension thermal noise, there is also thermal noise due to internal modes of the mirror coatings that affect the sensitivity of the detector.

Figure 1.3 shows the measured noise levels of LIGO and VIRGO detectors during their S5 and VSR1 science runs respectively.

1.3.2 Detection prospects

Nearly a century ago Einstein predicted the existence of GWs and it has been more than four decades since the first use of a GW detector, yet there has been no confirmed direct detection of GWs. The main reason for that is the very small amplitudes of GWs, even from most optimistic sources. Only recently, with advancements in technologies such as the stable high-power lasers, better acoustic and seismic isolation systems, nanometer-smooth

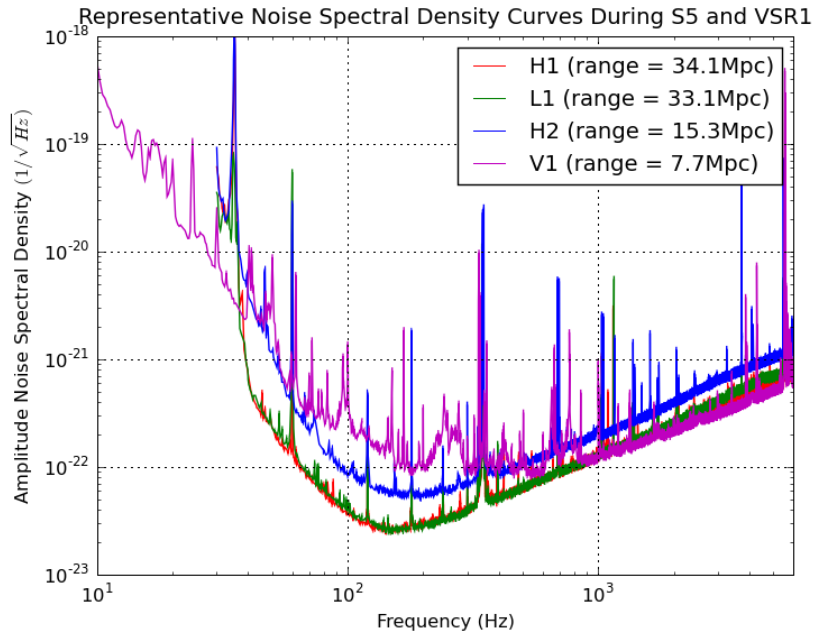


Figure 1.3: Strain spectra for LIGO detectors (H1, H2, L1) and Virgo detector (V1) during their S5 and VSR1 science runs respectively. The legend also provides distances up to which the detectors can detect a CBC signal with sufficient signal-to-noise ratio.

optics, and precise timing systems, detectors with sensitivities comparable to expected GW strains have been built. The current and next generation of GW detectors have realistic chance of detecting GWs within a few years of their operation.

Recently concluded science runs of LIGO and Virgo detectors did not observe any GW signals, but have provided interesting astrophysical and cosmological limits. The CBC analyses using those science run data resulted in upper limits on various binary mergers [56] with numbers close to the predictions by various electromagnetic observations. For example, the 90% upper limit on the rate of binary neutron star mergers is $3.9 \times 10^{-2} \text{Yr}^{-1} L_{10}^{-1}$ where L_{10} is 10^{10} times the blue solar luminosity. The searches for continuous waves from pulsars set upper limit on the ellipticity of such systems with $\epsilon \leq 10^{-6}$ [55]. Burst searches using the same data set resulted in an upper limit on the energy radiated in GWs within a distance scale: $5.6 \times 10^{-2} M_{\odot}$ at 16 Mpc, in the frequency around 150 Hz and GW signal duration of 1 sec [57]. Searches for SGWB set an upper limit on the strength of such a background,

below the limit predicted by the big-bang nucleosynthesis (BBN) in the LIGO frequency band, which is the focus of Chapter 2.

Currently most of the existing GW detectors are being upgraded to the next generation with increased sensitivities [71]. Also there are possibilities of new ground-based GW detectors [58] and space-based detectors [25] starting within this decade. Hence it is more likely that first direct GW detection will happen within this decade, maybe in time for the centennial of Einstein's general relativity paper.

1.4 Organization of other chapters

The rest of the thesis is organized as follows. In Chapter 2 we summarize some of the models of SGWB and describe an analysis pipeline used to search for such signals in LIGO data. We also present the search results obtained by using data from LIGO S5 science run. In Chapter 3 we look at some of the models of long duration GW transients and describe a new analysis pipeline developed to look for such signals. Then we present the results obtained from running the pipeline on LIGO S5 data searching for long GW transients from GRBs. In Chapter 4 we discuss the effect of seismic noise on current and future generation of GW detectors. We then describe an underground seismic array set up at Homestake mine, South Dakota to study the seismic field underground, which would be useful for next generation of GW detectors. We also present initial results and discuss some of the algorithms used for studying seismic field decomposition. In Chapter 5 we provide a summary of earlier chapters and results.

Chapter 2

Searches for stochastic gravitational waves in LIGO data

A stochastic background of gravitational waves is expected to arise from a large number of unresolved and uncorrelated sources. Since GWs can travel long distances without scattering and the universe is filled with large numbers of GW sources, it is natural to expect a background formed by the random superposition of GW signals from all these sources. In such cases, we cannot identify the sources individually (unless they are strong enough to stand above the rest of the signals) but can only make a statistical statement about the background as a whole. Stochastic gravitational-wave background can be of either cosmological origin produced by the events occurred during the early universe and/or of astrophysical origin produced by collections of astrophysical objects such as binary black holes, rotating neutron stars etc.

Since the Big Bang, the universe has undergone several transformations and most of them are believed to have produced GWs. For example, density perturbations created by the amplifications of vacuum fluctuations during the inflation could produce GWs. Such a background of GWs from the early universe, called cosmological (or) primordial GW background, is expected to provide information about the universe mere fractions of a second after the Big Bang [83, 151, 24, 18]. Here we note that for cosmological GWs, the concept of ‘individual sources’ may not be even meaningful (for example, inflationary density perturbations that produced GWs extended throughout the universe) and hence the ‘background’ description may be the only option.

As we discussed in Chapter 1, current universe contains GW sources that can be identified individually, if the signal is strong enough, and are distributed in large numbers throughout the universe. These sources could be well known binaries of neutron stars and black holes [35], rotating neutron stars [135], magnetars [136], galactic white-dwarf binaries [90, 26, 89, 120] or relatively unknown binary black holes [35]. A GW background from such recent sources, called astrophysical GW background, could provide information about the spatial distribution and formation rate of these various source populations.

The detection of a SGWB, of either cosmological or astrophysical origin, is a major science goal for both current and planned searches for GWs [83, 151, 24, 112]. Given the random nature of a stochastic background of GW radiation, it is difficult to distinguish between GW background and local detector noise just using one detector. Hence, searches for SGWB involve cross-correlating data from two or more detectors [83, 115, 40, 70, 19], under the assumption that correlated noise between any two detectors is negligible. For such a case, the contribution to the cross-correlation from the (common) GW signal grows linearly with the observation time T , while the noise grows like \sqrt{T} and so signal-to-noise ratio $\text{SNR} \propto \sqrt{T}$. This allows one to search for stochastic signals buried within the detector noise by integrating for a sufficiently long interval of time.

In this chapter, we provide a summary of some of the stochastic GW sources and describe a cross-correlation analysis pipeline that is used to search for SGWB in GW detector data [19]. We also present results of applying the pipeline on LIGO S5 data, acquired from November 2005 to October 2007.

2.1 Sources of stochastic GW background

The spectrum of stochastic GW background is usually described by the dimensionless quantity $\Omega_{\text{gw}}(f)$ given by

$$\Omega_{\text{gw}}(f) = \frac{f}{\rho_c} \frac{d\rho_{\text{gw}}}{df}, \quad (2.1)$$

where $d\rho_{\text{gw}}$ is the energy density of GWs contained in the frequency range f to $f + df$ and ρ_c is the critical energy density [19],

$$\rho_c = \frac{3c^2 H_0^2}{8\pi G}. \quad (2.2)$$

Here H_0 is the present day Hubble parameter. The measured values of H_0 are in the range of $67 - 72$ km/(Mpc – sec). Since there are uncertainties in the measurement of Hubble parameter H_0 , we write it as $H_0 = h_0 \times H_{100}$ where $H_{100} = 100$ km/(Mpc – sec) and use $h_0^2 \Omega_{\text{gw}}(f)$ as the reference quantity while comparing different models. Note that $h_0^2 \Omega_{\text{gw}}(f)$ is independent of actual Hubble expansion rate. While some of the cosmological and astrophysical models predict complex spectra for $\Omega_{\text{gw}}(f)$, most of them can be approximated by a power law given by

$$\Omega_{\text{gw}}(f) = \Omega_\alpha \left(\frac{f}{f_{\text{ref}}} \right)^\alpha, \quad (2.3)$$

where α is the spectral index and f_{ref} is some reference frequency.

2.1.1 Cosmological GW background

In standard cosmology, the universe after the Big Bang underwent several transformations such as inflation, phase transitions etc., to get to the current state. Most of these transformations are expected to produce radiations of all kinds, including GWs. Depending on how and when they were produced, these GWs would have specific frequency spectra. Due to the expansion of the universe, frequencies of the original GWs appear red-shifted today to lower frequencies. Using a simple Friedmann-Robertson-Walker (FRW) cosmological model, we can write an approximate relation between currently observable GW frequency f_0 and temperature of the universe T_* when they were produced as [112]

$$f_0 \simeq \frac{1.6 \times 10^{-7}}{\alpha} \left(\frac{T_*}{1 \text{ GeV}} \right) \text{ Hz}, \quad (2.4)$$

where α is a scale factor ≤ 1 , corresponding to the ratio of the wavelength of GW to Hubble size at that time. From Eq. (2.4), we see that there is a high frequency cutoff of $\sim 10^2$ GHz on

GW frequencies due to the highest possible plank scale temperatures $\sim 10^{19}$ GeV, assuming α is not too small. Also using the relation between time t_* (when the GWs were produced) and frequency f_0 given by [112]

$$t_* \simeq \frac{6.6 \times 10^{-21}}{\alpha^2} \left(\frac{1 \text{ Hz}}{f_0} \right)^2 \text{ sec} , \quad (2.5)$$

we can approximately determine the time t_* . Using Eqs. (2.4) and (2.5), for the frequencies at which current ground based interferometers are sensitive (~ 100 Hz), we get $T_* \simeq 10^9$ GeV and $t_* \simeq 10^{-24}$ sec which is mere fractions of second after the Big Bang.

Given below is a summary of some of the models that predict GWs from that epoch.

Inflationary models

In standard cosmology, inflation is a well accepted theory in which, just after the Big Bang, the universe undergoes rapid expansion within a short period of time. Even though the exact mechanism of such expansion is not well understood, inflation provides natural solutions to various cosmological problems such as flatness, horizon and non-existence of monopoles and hence became an integral part of the standard cosmology. It also agrees well with cosmic microwave background (CMB) observations.

During the inflation, the zero-point fluctuations of many fields including spacetime perturbations were amplified many-folds during a short period of time. Since the expansion was very fast, the initial zero-point fluctuations before the expansion ended up in the excited states after the expansion producing a lot of radiation. This is the basis for GW production in all inflationary models while the exact form or shape of the spectra depends on the individual model. For a simple De Sitter inflation, we get [112]

$$h_0^2 \Omega_{gw}(f) \simeq 10^{-13} \left(\frac{10^{-16}}{f} \right)^2 \left(\frac{\hbar H}{10^{-4} M_P c^2} \right)^2 \quad \text{for } 3 \times 10^{-18} \text{Hz} < f < 10^{-16} \text{Hz}, \quad (2.6)$$

$$\text{and } h_0^2 \Omega_{gw}(f) \simeq \left(\frac{\hbar H}{10^{-4} M_P c^2} \right)^2 \quad \text{for } 10^{-16} \text{Hz} < f < 10^{10} \text{Hz}. \quad (2.7)$$

where $M_P = \sqrt{\frac{\hbar c}{G}}$ is the Plank mass and H is the Hubble parameter during the De Sitter

inflation. Here 10^{-16} Hz corresponds to the scale at which radiation-matter transition occurred.

There are also other inflationary models that predict GWs from this epoch and in some cases the predicted spectra are different. For example, in slow-roll inflation the Hubble parameter is not constant, as in De Sitter inflation, but changes during the inflation and hence the spectrum in this case is not flat but a little tilted (also an order of magnitude lower) [112]. The Axion inflation, on the other hand, is expected to produce GWs with higher amplitude at frequencies relevant to the current and next generation of GW detectors [118].

At the end of inflation, the inflaton field responsible for the inflation is expected to transfer its potential energy into relativistic particles reproducing similar environment as in the beginning of the inflation. This process, called reheating, is also expected to produce GWs [52].

Cosmic strings

Cosmic strings are topological defects that might have formed during phase transitions in the early universe [98]. They are in general expected to be in the form of loops and to have high tension equal to their mass-per-length (multiplied by c^2). Because of such large tension, they would oscillate relativistically under their own tension producing GWs. The strings could also interact with each other and in the process break and reconnect again into smaller strings. These interactions would produce kinks and cusps that propagate at the speed of light along the string producing GWs [122]. The wavelength of the GWs produced in this model is proportional to the length of the loops and spans a wide range of frequencies ($\sim 10^{-8} - 10^{10}$ Hz). More recently, it was realized that fundamental strings, as in string theory, may also be expanded to cosmological scales during inflation producing cosmic strings [139]. Hence, searching for cosmic strings may provide a unique and powerful window into string theory and into particle physics at the highest energy scales.

Pre-Big-Bang model

In the pre-Big-Bang model [33, 54, 113] the universe starts off large and then undergoes a period of inflation driven by the kinetic energy of a dilaton field, after which the standard cosmology follows. Although more speculative than the standard cosmology model, the pre-Big-Bang model makes testable predictions of the GW spectrum. In the pre-Big-Bang model, the GWs are produced via the mechanism of amplification of vacuum fluctuations, analogous to the standard inflationary model. The typical GW spectrum increases as f^3 up to a turn-over frequency f_s , above which $\Omega_{\text{gw}}(f) \sim f^{3-2\mu}$ with $\mu < 1.5$. The spectrum cuts off at a frequency f_1 , which is theoretically expected to be within a factor of 10 from 4.3×10^{10} Hz.

Phase transitions

Standard model of particles physics predict various phase transitions during the evolution of the universe. According to the standard model, as the universe cools down after the Big Bang, first it would undergo grand unified theoretical (GUT) phase transition separating strong interaction from the rest of the forces, then electroweak phase transition separating weak interaction from electromagnetic interaction and finally QCD phase transition in which protons and neutrons condense out from the quark soup. If any of these phase transitions are of first order, then there will be density inhomogeneities which in turn can produce GWs [112]. There could also be first order phase transitions that are initiated by the formation of local bubbles of a new vacuum. If these bubbles are of critical size, then they would grow and collide with other bubbles producing GWs. Spectra of these GWs are expected to be highly peaked and the peak frequency is given by the Eq. (2.4) [18].

2.1.2 Astrophysical GW background

Unresolved GW signals from a large number of astrophysical sources can also create a GW background. Unlike cosmological background, astrophysical GW background would provide information about the recent universe at red-shifts $z \sim 2 - 6$. There are various

sources/mechanism that can produce such backgrounds. These sources could be galactic such as white-dwarf binaries, or extra-galactic such as collapsars, BBH etc. The GW background from galactic sources is expected to have strong anisotropies (because of the disc nature of our galaxy) while ones from extra-galactic sources are expected to be isotropic. Some of these sources are described in more detail in Chapter 3. Depending on the rate of such sources, the GW background could be stochastic or not. If the rate of such sources is high i.e., the duty cycle $D > 1$, which is the ratio of signal duration to time between successive signals, then the background will be stochastic otherwise it will be either burstlike ($D \ll 1$) or popcorn signal ($D \lesssim 1$).

In general, the expected GW frequency from an astrophysical source can be estimated using its dynamical frequency given by Eq. (1.19). By using $R \leq \frac{2GM}{c^2}$ (Schwarzschild radius) in Eq. (1.19) and a typical mass of $M = 1.4 M_{\odot}$, we get an approximate upper limit on the expected frequency which is ~ 20 kHz. Thus we see that, unlike cosmological GW backgrounds which can extend up to GHz, astrophysical backgrounds are limited in frequency range extending only up to tens of kHz. Hence any observation of GW background at very high frequencies would clearly correspond to a cosmological origin. At low frequencies, astrophysical GW backgrounds are expected to have higher amplitudes and hence can potentially mask a cosmological background. Since most of the predicted astrophysical backgrounds are either low in frequencies or low in amplitudes compared to the sensitivities of current generation of LIGO detectors we do not discuss them further here. More discussions on these models can be found in [35, 154, 136, 135].

2.1.3 Observational constraints

There are various observations that constrain $\Omega_{gw}(f)$ in all or part of the frequency range. Below we summarize a few of the important bounds that apply to ground based GW detectors.

The nucleosynthesis bound

The most constraining bounds on the SGWB comes from the Big-Bang-Nucleosynthesis (BBN) and from CMB measurements. The BBN bound is derived from the fact that a large GW energy density at the time of BBN would alter the expansion rate of the universe and in turn would affect the abundances of the light nuclei produced in the early universe. The BBN model and observations of abundances of lightest nuclei constrain the total GW energy density at the time of nucleosynthesis [112, 18] as:

$$\int \Omega_{\text{gw}}(f) d(\ln f) < 1.1 \times 10^{-5} (N_\nu - 3), \quad (2.8)$$

where N_ν (the *effective* number of neutrino species at the time of BBN) captures the uncertainty in the radiation content during BBN. Measurements of the light-element abundances, combined with the Wilkinson Microwave Anisotropy Probe (WMAP) data give the upper bound $N_\nu - 3 < 1.4$ [47].

Similarly, a large GW background at the time of decoupling of CMB would alter the observed CMB and matter power spectra. Assuming homogeneous initial conditions, the total GW energy density at the time of CMB decoupling is constrained to $\int \Omega_{\text{gw}}(f) d(\ln f) < 1.3 \times 10^{-5}$ [153]. Both the bounds given above, apply only to GWs (and other unknown radiation) emitted before the star and galaxy formations.

Anisotropy of cosmic microwave background

The strongest constrain on the low frequency spectrum of $\Omega_{\text{gw}}(f)$ comes from the large scale temperature fluctuations observed in the CMB by Cosmic Background Explorer (COBE). At the time of last scattering, when CMB photons started to free stream, any scalar density perturbations produced by the inflation would have red-shifted the CMB photons. This effect is called the Sachs-Wolf effect. As we saw in Section 2.1.1, the inflation that produced these scalar density perturbations could also produce tensor perturbations, which are GWs. Since GWs stretch/shrink spatial dimensions, any GWs present at that time would have changed the frequency of CMB photons and contributed to the observed temperature fluctuations.

As such effects have not been observed by CMB measurements at low l -values, an upper limit is placed on $h_0^2 \Omega_{gw}(f)$ [112],

$$h_0^2 \Omega_{gw}(f) < 7 \times \left(\frac{3 \times 10^{-18}}{f} \right) \quad \text{for } (3 \times 10^{-8} \text{ Hz} < f < 3 \times 10^{-16} \text{ Hz}), \quad (2.9)$$

$$\text{and } h_0^2 \Omega_{gw}(f) < 10^{-14} \quad \text{for } f > 3 \times 10^{-16} \text{ Hz} \quad (2.10)$$

Figure 2.1 shows existing bounds and expected spectra for the cosmological models described in Section 2.1.1.

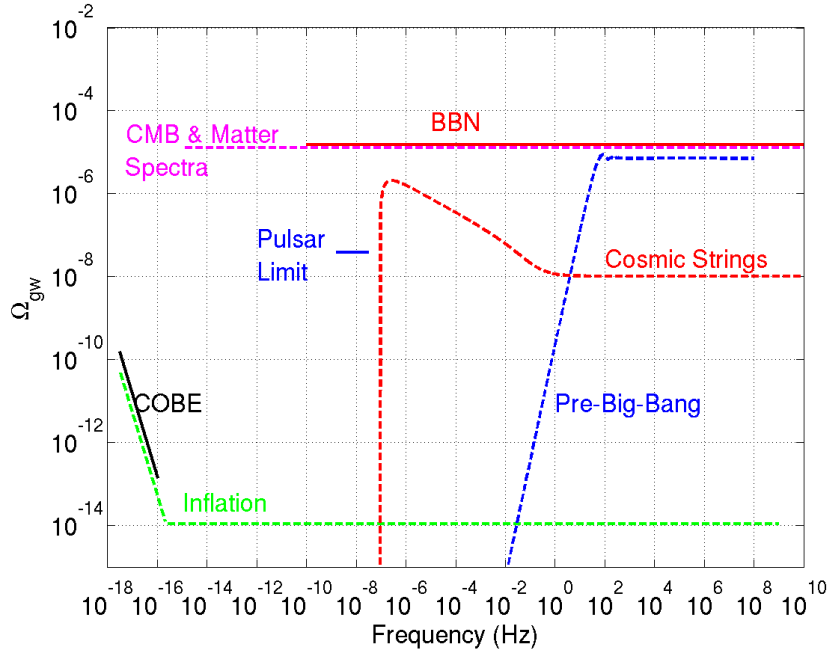


Figure 2.1: Existing bounds and expected spectra for some of the cosmological models (Section 2.1.1, Section 2.1.3). The pulsar limit shown in this plot comes from the long time observation of timing variations in a set of pulsars as mentioned in Section 1.3.

2.2 Cross-correlation statistics

In this section, we derive the cross-correlation statistic that was used for SGWB searches described in Section 2.4 and Section 2.5. For the derivation we follow the conventions of [19]

and [66]. The metric perturbation due to a GW coming from a source in the direction $\hat{\Omega}$ defined on a two sphere of the equatorial coordinate system (cf. Figure 2.2) and consisting of both $+$ and \times polarizations can be written as (using Eq. (1.14))

$$h_{ab}(t, \vec{x}) = \sum_A \int_{-\infty}^{\infty} df e_{ab}^A(\hat{\Omega}) h_A(f, \hat{\Omega}) e^{2\pi i f(t + \hat{\Omega} \cdot \vec{x}/c)} , \quad (2.11)$$

where a, b corresponds to spatial indices (x, y, z) and A correspond to different polarizations. The quantities e_{ab}^A are the polarization tensors and $h_A(f)$ are corresponding amplitudes expected at the origin of equatorial coordinate system (the center of Earth). In case of a large number of sources distributed over the sky, we integrate Eq. (2.11) over the two sphere as given by

$$h_{ab}(t, \vec{x}) = \sum_A \int_{-\infty}^{\infty} df \int_{S^2} d\hat{\Omega} e_{ab}^A(\hat{\Omega}) h_A(f, \hat{\Omega}) e^{2\pi i f(t + \hat{\Omega} \cdot \vec{x}/c)} . \quad (2.12)$$

If we assume that the observed GW signal is independent of direction on the sky and also of polarizations, then we can characterize the expectation value of GW strain power spectrum as,

$$\langle \tilde{h}_A^*(f, \hat{\Omega}) \tilde{h}_{A'}(f', \hat{\Omega}') \rangle = H(f) \delta(f - f') \delta_{AA'} \delta(\hat{\Omega} - \hat{\Omega}') , \quad (2.13)$$

where $\delta(f - f')$ and $\delta(\hat{\Omega} - \hat{\Omega}')$ are Dirac delta functions and $\delta_{AA'}$ is Kronecker delta function. Here $H(f)$ represents signal power spectrum.

The energy density in GWs is given by [116]

$$\rho_{gw} = \frac{c^2}{32\pi G} \langle \dot{h}_{ab}(t, \vec{x}) \dot{h}^{ab}(t, \vec{x}) \rangle , \quad (2.14)$$

and using Eqs. (2.12), (2.13), we can write it as

$$\rho_{gw} = \frac{4\pi^2 c^2}{G} \int_0^{\infty} df f^2 H(f) . \quad (2.15)$$

Using Eqs. (2.1), (2.2) and (2.15), we get

$$H(f) = \frac{3H_0^2}{32\pi^3} |f|^{-3} \Omega_{gw}(|f|) , \quad (2.16)$$

which relates the signal power spectrum to the dimensional spectrum $\Omega_{gw}(f)$.

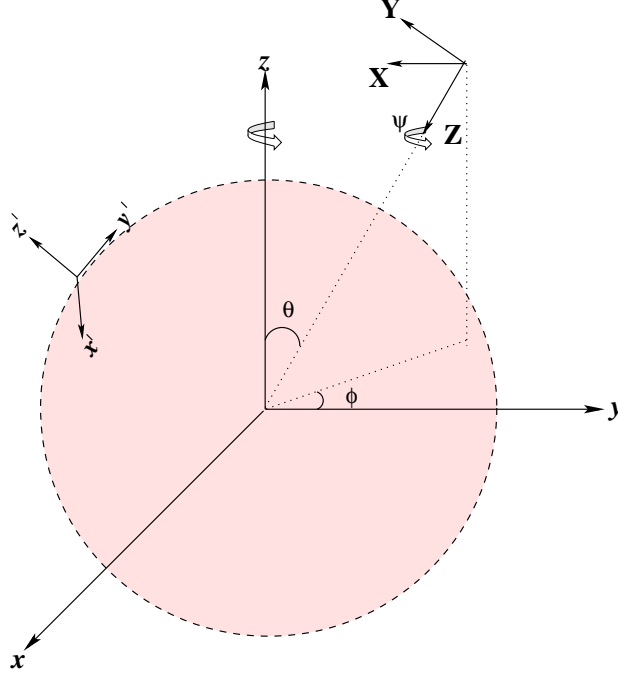


Figure 2.2: The above figure shows different coordinate systems and angles referred in Section 2.2. For the calculation in Section 2.2, we assume $\psi = 0$.

In Eq. (1.14), $e^{+, \times}$ are defined in the wave frame (X, Y, Z) while in Eqs. (2.11) and (2.12), they are defined in the Earth frame (cf. Figure 2.2). In spherical coordinates (θ, ϕ, Ω) defined in the Earth frame, the rotation matrix $R: (X, Y, Z) \rightarrow (x, y, z)$ is

$$R = \begin{pmatrix} -\cos \theta \cos \phi & -\sin \phi & -\cos \phi \sin \theta \\ -\cos \theta \sin \phi & \cos \phi & -\sin \theta \sin \phi \\ \sin \theta & 0 & -\cos \theta \end{pmatrix}. \quad (2.17)$$

Here θ , called declination, is measured from the north pole (\hat{z}) of Earth and ϕ , called right ascension, is measured from vernal equinox (\hat{x}). By using a similarity transformation we

can write the polarizations tensors as

$$e^+(\hat{\Omega}) = R \cdot \begin{pmatrix} 1 & 0 & 0 \\ 0 & -1 & 0 \\ 0 & 0 & 0 \end{pmatrix} \cdot R^T, \quad e^\times(\hat{\Omega}) = R \cdot \begin{pmatrix} 0 & 1 & 0 \\ 1 & 0 & 0 \\ 0 & 0 & 0 \end{pmatrix} \cdot R^T, \quad (2.18)$$

where the source direction $\hat{\Omega}$ is given by

$$\hat{\Omega} = \cos \phi \sin \theta \hat{x} + \sin \theta \sin \phi \hat{y} + \cos \theta \hat{z}, \quad (2.19)$$

and the wave propagation is in $-\hat{\Omega}$.

The response of a detector I , at \vec{x} , to a GW with metric perturbation h_{ab} is

$$h_I(t) = h_{ab}(t, \vec{x}) d_I^{ab}(t), \quad (2.20)$$

where the detector tensor d_I is given by [19]:

$$d_I = \frac{1}{2}(\hat{x}'_I \otimes \hat{x}'_I - \hat{y}'_I \otimes \hat{y}'_I) . \quad (2.21)$$

The tensor d_I is defined in the detector frame (x', y', z') and needs to be transformed to equatorial coordinates system in which, owing to its simplicity, all the calculations are done. For this we can use a rotation matrix similar to the one given by Eq. (2.17), but using longitude and latitude of the detector location as the rotation angles. Also due to the rotation of Earth, there is an additional (time dependent) rotation of d_I and \vec{x}_I around \hat{z} axis. Here after we will assume that the above necessary rotations were done to bring all the quantities in Earth's frame.

Using Eqs.(2.12) and (2.20), the GW strain in detector I can be written as,

$$\tilde{h}_I(t) = \sum_A \int_{-\infty}^{\infty} df \int_{S^2} d\hat{\Omega} F_I^A(t; \hat{\Omega}) h_A(f, \hat{\Omega}) e^{2\pi i f(t + \hat{\Omega} \cdot \vec{x}/c)}, \quad (2.22)$$

where we have used detector response functions $F_I^A(t; \hat{\Omega})$ defined by:

$$F_I^A(t; \hat{\Omega}) := e_{ab}^A(\hat{\Omega}) d_I^{ab}(t) . \quad (2.23)$$

Since the detectors have intrinsic noise $n(t)$ in addition to any external signal $h(t)$, the data from each detector can be written as $s_I(t) := h_I(t) + n_I(t)$ detector. We define the cross-correlation estimator for a time segment M of length T as:

$$Y_M := \int_{t-T/2}^{t+T/2} dt' \int_{t-T/2}^{t+T/2} dt'' s_I(t') s_J(t'') Q(t', t'') , \quad (2.24)$$

where I, J correspond to two different detectors and $Q(t', t'')$ is a filter function which we will choose to maximize the signal-to-noise ratio of Y_M . At the end of this section, we will show that using Y_M we can get an estimate of $\Omega_{gw}(f)$. For simplicity, the rest of the derivation in this section is done in Fourier domain.

We define short time Fourier transform (SFT) of a time series $y(t)$ of length T and its inverse transform as,

$$\tilde{y}(t; f) := \int_{t-T}^{t+T} dt' y(t') e^{-2\pi i f t'} , \quad (2.25)$$

$$y(t) := \int_{-\infty}^{\infty} df \tilde{y}(t; f) e^{2\pi i f t} . \quad (2.26)$$

Unlike normal Fourier transform which is defined on the interval $[-\infty, \infty]$, here we use finite amount of data and hence to distinguish it from normal Fourier transform we reference it using the time segment t used for the Fourier transform. Note that the above two definitions are compatible with each other.

Using the above definitions of Fourier transform, Eq. (2.24) can be written as

$$Y_M := \int_{-\infty}^{\infty} df \int_{-\infty}^{\infty} df' \delta_T(f - f') \tilde{s}_I^*(t; f) \tilde{s}_J(t; f') \tilde{Q}(f') , \quad (2.27)$$

where finite-time approximation to Dirac delta function $\delta_T(f)$ is defined as,

$$\delta_T(f) := \int_{-T/2}^{T/2} dt' e^{-2\pi i f t'} = \frac{\sin(\pi f T)}{\pi f}. \quad (2.28)$$

As the duration of the data segment $T \rightarrow \infty$, $\delta_T(f)$ approaches Dirac delta function $\delta(f)$. But for a finite time interval T , this function has the property that $\delta_T(0) = T$.

The mean value of Y (here after we omit the subscript M) is then given by,

$$\mu = \langle Y \rangle = \int_{-\infty}^{\infty} df \int_{-\infty}^{\infty} df' \delta_T(f - f') \langle \tilde{s}_I^*(t; f) \tilde{s}_J(t; f') \rangle \tilde{Q}(f'). \quad (2.29)$$

Since $\tilde{s}_I(t; f) = \tilde{n}_I(t; f) + \tilde{h}_I(t; f)$, the expectation value of $\langle \tilde{s}_I^*(t; f) \tilde{s}_J(t; f') \rangle$ can be written in terms of four expectation values involving all combinations of $\tilde{n}_{I,J}(t; f)$ and $\tilde{h}_{I,J}(t; f)$. If we assume that the noise is uncorrelated between two detectors and also uncorrelated with the GW signal then only $\langle \tilde{h}_I^*(t; f) \tilde{h}_J(t; f') \rangle$ term survives (i.e., the signal correlates with itself) and other terms vanish. Then Eq. (2.29) becomes

$$\mu = \int_{-\infty}^{\infty} df \int_{-\infty}^{\infty} df' \delta_T(f - f') \langle \tilde{h}_I^*(t; f) \tilde{h}_J(t; f') \rangle \tilde{Q}(f'). \quad (2.30)$$

Using Eqs. (2.22) and Eq. (2.13) in the above equation, we get,

$$\begin{aligned} \mu &= \sum_A \sum_{A'} \int_{S^2} d\hat{\Omega} \int_{S^2} d\hat{\Omega}' \int_{t-T/2}^{t+T/2} dt' \int_{t-T/2}^{t+T/2} dt'' \int_{-\infty}^{\infty} df \int_{-\infty}^{\infty} df' \\ &\langle h_A^*(f, \hat{\Omega}) h_{A'}(f', \hat{\Omega}') \rangle e^{2\pi i(f t' - f' t'')} e^{-2\pi i f(t' + \hat{\Omega} \cdot \vec{x}_I/c)} \\ &e^{2\pi i f'(t'' + \hat{\Omega}' \cdot \vec{x}_J/c)} F_I^A(t'; \hat{\Omega}) F_J^{A'}(t''; \hat{\Omega}') \tilde{Q}(f') \end{aligned} \quad (2.31)$$

$$\begin{aligned} &= \sum_A \int_{-\infty}^{\infty} df \int_{-\infty}^{\infty} df' \int_{S^2} d\hat{\Omega} H(f') \delta_T(f' - f) \delta_T(f - f') \\ &e^{-2\pi i f'(\hat{\Omega} \cdot (\vec{x}_I - \vec{x}_J)/c)} F_I^A(t; \hat{\Omega}) F_J^A(t; \hat{\Omega}) \tilde{Q}(f') \end{aligned} \quad (2.32)$$

By replacing one of the $\delta_T(f)$ by Dirac delta function and evaluating the above expres-

sion, we get

$$\mu = \sum_A \int_{-\infty}^{\infty} df \int_{S^2} d\hat{\Omega} H(f) e^{-2\pi i f \hat{\Omega} \cdot \Delta \vec{x}_{IJ}/c} F_I^A(t; \hat{\Omega}) F_J^A(t; \hat{\Omega}) \tilde{Q}(f) \quad (2.33)$$

$$= \frac{3H_0^2}{20\pi^2} T \int_{-\infty}^{\infty} |f|^{-3} \Omega_{gw}(|f|) \gamma(|f|) \tilde{Q}(f) df \quad (2.34)$$

where we have used Eq. (2.16) and the definition $\Delta \vec{x}_{IJ} := \vec{x}_I - \vec{x}_J$. Here we also have defined $\gamma(f)$, called the *overlap reduction function*, as

$$\gamma(f) = \frac{5}{8\pi} \sum_A \int_{S^2} d\hat{\Omega} e^{-2\pi i f \hat{\Omega} \cdot \Delta \vec{x}_{IJ}/c} F_I^A(t; \hat{\Omega}) F_J^A(t; \hat{\Omega}) \quad (2.35)$$

The overlap reduction function characterizes the sensitivity loss due to the separation and relative orientation between the detector I, J . The factor $\frac{5}{8\pi}$ is chosen such that $\gamma(f) = 1$ for a pair of colocated and coaligned detectors. As shown in [19], analytically it can be written as a sum of three Bessel functions. Figure 2.3 shows the $\gamma(f)$ for the colocated and non-colocated pairs of LIGO detectors.

Now we calculate the variance of Y which is defined as $\sigma_Y^2 := \langle Y^2 \rangle - \langle Y \rangle^2$. If we assume that the noise intrinsic to the detectors $P_1(f)$ and $P_2(f)$ are much greater than the signal $H(f)$, then we can neglect the $\langle Y \rangle^2$ term in the definition of σ_Y^2 . This is called small signal limit and in this limit:

$$\begin{aligned} \sigma_Y^2 &= \int_{-\infty}^{\infty} df \int_{-\infty}^{\infty} df' \int_{-\infty}^{\infty} dk \int_{-\infty}^{\infty} dk' \delta_T(f' - f) \delta_T(k' - k) \\ &\quad \langle \tilde{s}_1^*(f') \tilde{s}_2(f) \tilde{s}_1^*(k') \tilde{s}_2(k) \rangle \tilde{Q}(f') \tilde{Q}(k') \end{aligned} \quad (2.36)$$

Using the fact that for mean zero, Gaussian random variables (x_1, x_2, x_3, x_4) ,

$$\langle x_1 x_2 x_3 x_4 \rangle = \langle x_1 x_2 \rangle \langle x_3 x_4 \rangle + \langle x_1 x_3 \rangle \langle x_2 x_4 \rangle + \langle x_1 x_4 \rangle \langle x_2 x_3 \rangle, \quad (2.37)$$

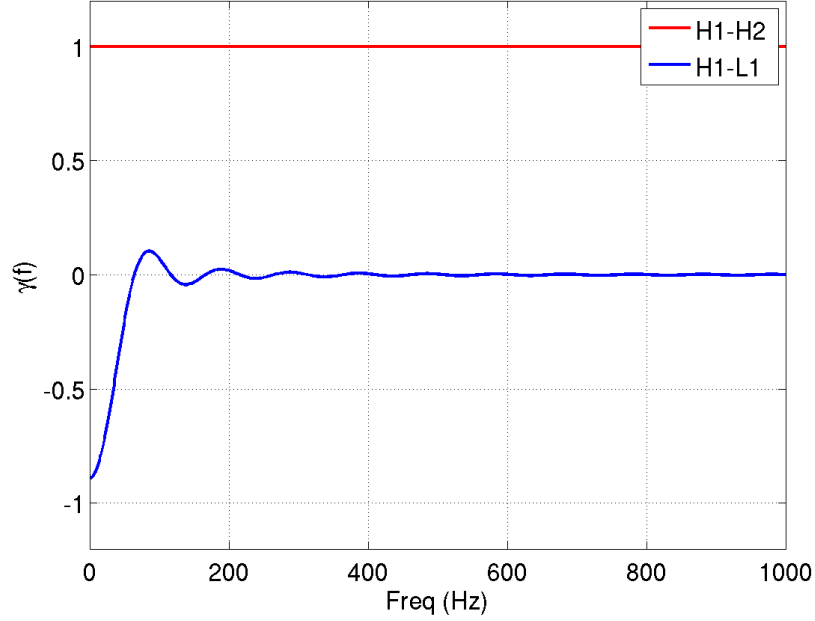


Figure 2.3: The above figure shows overlap reduction functions for colocated, coaligned H1-H2 LIGO detector pair as well as non-colocated and differently oriented H1-L1 LIGO detector pair.

and $n_1(t)$, $n_2(t)$ are independent of each other and of the signal $h(t)$, we get

$$\begin{aligned} \sigma_Y^2 &= \int_{-\infty}^{\infty} df \int_{-\infty}^{\infty} df' \int_{-\infty}^{\infty} dk \int_{-\infty}^{\infty} dk' \delta_T(f' - f) \delta_T(k' - k) \\ &\quad \langle \tilde{n}_1^*(f') \tilde{n}_1^*(k') \rangle \langle \tilde{n}_2(f) \tilde{n}_2(k) \rangle \tilde{Q}(f') \tilde{Q}(k') \end{aligned} \quad (2.38)$$

We define *one sided noise power spectrum* as

$$\langle n_I(t) n_I(t') \rangle := \frac{1}{2} \int_{-\infty}^{\infty} df e^{i2\pi f(t-t')} P_I(|f|) \quad (2.39)$$

Using the definition of SFT, we can rewrite the above definition in Fourier domain as

$$\langle \tilde{n}_I^*(t; f) \tilde{n}_I(t; f') \rangle = \frac{1}{2} \int_{-\infty}^{\infty} df'' P_I(t; |f|) \delta_T(f'' - f') \delta_T(f'' - f) \quad (2.40)$$

in the limit of a large observation time, $T \rightarrow \infty$, the above expression reduces to the familiar

form

$$\langle \tilde{n}_I^*(t; f) \tilde{n}_I(t; f') \rangle = \frac{1}{2} \delta(f - f') P_I(t; |f|) \quad (2.41)$$

while for a finite observation time T , it becomes

$$\langle \tilde{n}_I^*(t; f) \tilde{n}_I(t; f') \rangle = \frac{T}{2} P_I(t; |f|) \quad (2.42)$$

Using Eq. (2.42) and reality condition of $n_I(t)$ i.e, $\tilde{n}_I^*(t; f) = \tilde{n}_I(t; -f)$, σ_Y in Eq. (2.38) becomes

$$\sigma_Y^2 \approx \frac{1}{4} \int_{-\infty}^{\infty} df P_1(|f|) P_2(|f|) |\tilde{Q}(f)|^2 \quad (2.43)$$

As shown in [19], by maximizing over SNR ($:= \frac{Y}{\sigma_Y}$), we can show that the filter function $\tilde{Q}(f)$ takes the form,

$$\tilde{Q}(f) = \mathcal{N} \frac{\gamma(f) \Omega_{\text{gw}}(f)}{f^3 P_1(f) P_2(f)} . \quad (2.44)$$

where \mathcal{N} is a normalization constant. Here we see that the optimal filter $\tilde{Q}(f)$ depends on the signal model itself. This is a generalization of the fact that any optimal data analysis pipeline would require all the information about the signal we are looking for [88]. For our analyses described in this chapter we use a power-law model given by Eq. (2.3). We also define the normalization constant \mathcal{N} such that $\langle Y \rangle = T \Omega_\alpha$. In the next sections, we apply this statistics to search for SGWB signals using data from LIGO detectors.

2.3 Analysis pipeline

In the previous section we derived a cross-correlation statistics that can be applied to detector data to get a measurement of $\Omega_{\text{gw}}(f)$. In this section we will look at some practical issues and considerations in doing the analysis. The real detector data suffers from various instrumental and environmental correlations that would affect the efficiency of the cross-correlation statistic. Hence steps need to be taken to mitigate such correlations. Below is an outline of the analysis pipeline we used that includes such mitigation efforts:

- Initial data selection accounting for known bad periods of data;

- Data quality cuts (time and frequency domain);
- Applying cross-correlation technique to smaller time segments;
- Combining results from individual segments (and also from different detector pairs, if required);
- Final result is considered significant if its SNR is high (for example, > 5), otherwise it is just noise fluctuation and hence set an upper limit.

Apart from the above steps we also perform software and hardware injections to check for the consistency of the pipeline. Hardware injections are artificial signals injected into the interferometers via mechanical couplings while software injections are synthetic signals added to the interferometer data, just before the analysis.

2.3.1 Initial data selection

For our analyses, we used LIGO data acquired during the science run S5, which took place between November 5, 2005 and September 30, 2007. During this period all three LIGO detectors (H1, H2 and L1) were operational, albeit with different up-time, and we analyzed all three possible pairs. Due to the complexity of H1-H2 pair analysis (more on this in Section 2.5), here we present the analyses and results in two parts: one for two non-colocated pairs H1-L1 and H2-L1 and another for colocated H1-H2 pair.

For all the three pairs, we rejected time periods when:

- there were problems with the calibration of the data;
- the interferometers were within 30 s of loss of lock;
- there were artificial signals inserted into the data for calibration and characterization purposes;
- various data acquisition overflows were observed.

With these cuts, we obtained coincident data of ~ 292 days for H1-L1 pair, ~ 294 days for H2-L1 pair and ~ 357 days for H1-H2 pair.

2.3.2 Data quality cuts

After the initial data selection, we applied several frequency domain cuts to remove problematic frequencies from the analyses. There were well known narrow band instrumental lines (frequencies) that were expected to have significant correlation between the detectors. For example, the 60 Hz power line and its harmonics were strongly correlated between the detectors, even for well separated H1-L1 and H2-L1 pairs. To identify these correlated instrumental lines we used coherence and time-shift methods, which are described below. Results of applications of these methods to various detector pairs are given in Section 2.4 and Section 2.5.

Coherence analysis

The simplest method for identifying correlated noise between two detectors is to calculate the magnitude squared coherence, $\Gamma_{12}(f) \equiv |\gamma_{12}(f)|^2$, between the detectors where

$$\gamma_{12}(f) \equiv \frac{2}{T} \frac{\langle \tilde{s}_1^*(f) \tilde{s}_2(f) \rangle_N}{\sqrt{\langle P_1(f) \rangle_N \langle P_2(f) \rangle_N}}. \quad (2.45)$$

Here T denotes the duration of a single segment of data, and angle brackets $\langle \rangle_N$ denotes an average over N segments. The quantity $(\tilde{s}_1^*(f) \tilde{s}_2(f))$ is the cross-spectral density (CSD) between detectors 1,2 and $P_1(f)$, $P_2(f)$ are the power-spectral densities (PSD) of detectors 1, 2 respectively. For uncorrelated Gaussian data, the expected value of $\Gamma_{12}(f)$ is equal to $1/N$. This method is especially useful at finding narrowband features that stick out above the expected $1/N$ level. Since we expect the stochastic GW background to be broadband, with relatively little variation in the LIGO band (~ 40 – 1000 Hz), most of these narrowband features can be attributed to instrumental and/or environmental correlations.

Time-shift analysis

A second method for identifying narrowband correlated noise is to *time-shift* the time-series output of one detector relative to that of the other detector before doing the cross-correlation analysis [73]. By introducing a shift of ± 1 second, which is significantly larger

than the correlation time for a broadband GW signal (~ 10 ms, cf. Figure 2.8) we eliminate broadband GW correlations while preserving narrowband noise features.

2.3.3 Applying cross-correlation statistic

In the derivation of Y we used Fourier transforms of detector data of duration T . In theory, there is no restriction on T one could use. But in practice, it is limited by the non-stationarity (fluctuations in noise levels) of the data. For our analyses we used $T = 60$ sec which was within the fluctuation time scales. Apart from choosing the duration of segments, we also had to remove noisy low frequency contents (due to high seismic noise floor). So we decimated initial 16,384 Hz data to 512 Hz and high-pass filtered it with a 6th order Butterworth filter with 32 Hz knee frequency. Also each analysis segment was Hann-windowed before doing Fourier transform to avoid spectral leakage and *ringing* effects. To recover the loss of signal-to-noise due to Hann-windowing, segments were 50% overlapped. At the end, a weighted average was performed over all segments, with inverse variances as weights, properly accounting for overlapping effects [107, 86].

If Y_M and $\sigma_{Y_M}^2$ are the mean and variance of segment M , then the final estimate and its variance are given by,

$$Y_{\text{final}} = \frac{\sum_M \sigma_{Y_M}^{-2} Y_M}{\sum_M \sigma_{Y_M}^{-2}} \quad (2.46)$$

$$\sigma_{\text{final}}^{-2} = \sum_M \sigma_{Y_M}^{-2} \quad (2.47)$$

A similar weighted average is used to combine data from different pairs of detectors. In our analyses we calculated $\sigma_{Y_M}^2$ using two adjacent segments (averaged) instead of the segment from which Y_M was calculated. This was done to avoid the bias in the estimate of both Y_M and $\sigma_{Y_M}^2$ [86].

Stationarity cut

Apart from the data quality cuts defined in Section 2.3.2, we also applied a stationarity cut requiring that $\sigma_{Y_M}^2$ be consistent between neighboring segments. In this cut we reject segments M for which

$$\Delta\sigma = \frac{|\sigma_{Y_M} - \sigma_{Y_M}^*|}{\sigma_{Y_M}} > \epsilon \quad (2.48)$$

where σ_{Y_M} is calculated using two segments neighboring to M and $\sigma_{Y_M}^*$ is calculated using the segment M itself. The threshold ϵ was chosen such that it produces a Gaussian distribution for remaining Y_M . For our analyses we found that $\epsilon = 0.2$ was suitable to use.

Effect of windowing and overlapping

When we calculate Fourier transforms as required by the cross-correlation statistic, we first window the time series with Hann window to avoid spectral leakage from strong low frequencies and other known instrumental lines. With window function included, the Fourier transform is now defined as,

$$\tilde{y}(t; f) := \int_{t-T}^{t+T} dt' w(t') y(t') e^{-2\pi i f t'} \quad (2.49)$$

where $w(t)$ is the window function. With this modification, the new Y_M and its variance $\sigma_{Y_M}^2$ become $\bar{w}^2 Y_M$ and $\bar{w}^4 \sigma_{Y_M}^2$, respectively. For overlapping segments, there is also another correction that need to be included when combining results from individual overlapping segments M using Eqs. (2.46) and (2.47) [107].

Apart from the above corrections due to overlapping, there is also a bias factor associated with σ_{Y_M} . In our analysis, Y_M is calculated using Fourier transform of whole T sec of data while σ_{Y_M} is calculated using *pwelch* method which subdivides T sec into smaller segments before calculating Fourier transforms. Hence σ_{Y_M} has to be corrected for it; the relation between true and measured σ^2 is given by [86]

$$\sigma_{true}^2 \approx \sigma_{measured}^2 \left(1 + \frac{\kappa}{(N_{avg})_1 + (N_{avg})_2} \right), \quad (2.50)$$

where κ is 1 for non-overlapping segments and 11/9 for overlapping segments. Here $(N_{avg})_{1,2}$ correspond to number of (sub-)segments used to calculate $P_{1,2}$. For our analysis we used $T = 60$ and frequency bin width $\Delta f = 0.25$ (corresponding to 4 sec sub-segments) which correspond to $N_{avg,(1,2)} = 29$ 50% overlapping sub-segments. This gives a bias factor of 1.021.

Upper limit calculations

In case of non-detection i.e., if the signal-to-noise ratio of the observed Ω_α , $Y_{\text{final}}/\sigma_{\text{final}}$, is small (for example ≤ 5), then we set an upper limit on Ω_α using a Bayesian approach. The upper limit $\Omega_{\alpha,UL}$ at a certain confidence level (C.L) is obtained from the likelihood function $p(\Omega_\alpha|\Omega_{\alpha,obs}, \sigma_{\alpha,obs})$ by requiring that

$$\int_0^{\Omega_{\alpha,UL}} p(\Omega_\alpha|\Omega_{\alpha,obs}, \sigma_{\alpha,obs})p(\Omega_\alpha)d\Omega_\alpha = \text{C.L} , \quad (2.51)$$

where the likelihood function

$$p(\Omega_\alpha|\Omega_{\alpha,obs}, \sigma_{\alpha,obs}) = \frac{1}{\sqrt{2\pi}\sigma_{\alpha,obs}} \exp \left[-\frac{(\Omega_{\alpha,obs} - \Omega_\alpha)^2}{2\sigma_{\alpha,obs}^2} \right] , \quad (2.52)$$

and $p(\Omega_\alpha)$ is prior information on the expected Ω_α spectrum. Here $\Omega_{\alpha,obs}$ ($= Y_{\text{final}}/T$) and $\sigma_{\alpha,obs}$ ($=\sigma_{\text{final}}/T$) correspond to the observed GW spectrum and its error bar respectively. In reality, there are also systematic and statistical uncertainties on the measured values of $\Omega_{\alpha,obs}$ and $\sigma_{\alpha,obs}$ which would affect the likelihood function. If the uncertainties can be characterized by a Gaussian distribution with mean 1 and standard deviation f (which is the case for calibration uncertainties), then the new marginalized likelihood function can be written as [62],

$$p(\Omega_\alpha|\Omega_{\alpha,obs}, \sigma_{\alpha,obs}) = \frac{1}{\sqrt{2\pi}\sigma_{\alpha,obs}} \exp \left[-\frac{(\Omega_{\alpha,obs} - \Omega_\alpha)^2}{2(\sigma_{\alpha,obs}^2 + f^2\Omega_{\alpha,obs}^2)} \right] . \quad (2.53)$$

2.4 Results using non-located LIGO detectors

In this section we present analysis and results using non-located LIGO detector pairs H1-L1 and H2-L1. We applied all the time and frequency domain cuts described in Section 2.3. As mentioned in Section 2.3.1 for this analysis we used data acquired during the science run S5, which took place between November 5, 2005 and September 30, 2007.

2.4.1 Data quality cuts

Figure 2.4 and Figure 2.5 shows coherence calculated between detector pairs H1-L1 and H2-L1 using Eq. (2.45). For Gaussian noise, the distribution of Γ_{12} is expected to follow an exponential distribution. Since we downsample the detector raw time-series from 16 kHz to 512 Hz, which amounts to averaging, the resulting data is expected to be almost Gaussian. From the coherence plots we see that once we remove the outliers, the remaining frequency bins indeed follow an exponential distribution. These calculations revealed several instrumentally correlated lines between each pair of interferometers: 16 Hz harmonics (associated with the data acquisition clock), 60 Hz harmonics (AC power line), and injected simulated pulsar signals (52.75 Hz, 108.75 Hz, 148 Hz, 193.5 Hz, and 265.5 Hz). These lines were excluded from the final calculations of Y_{final} (zero-lag analysis).

Stationarity cut

With a 20% threshold ($\epsilon = 0.2$), the stationarity cut removed around 3% of total segments. The Y_I of remaining segments were in good agreement with Gaussian distribution as expected (cf. Figure 2.6). The data quality selection was performed blindly, using an un-physical 0.5-sec time-shift between the two interferometers.

2.4.2 Software and Hardware injections

The search algorithm used for this analysis was verified using signal simulations. The hardware simulations were performed using short and strong signals (to avoid downtime in observing for astrophysical signals). The software simulations were performed by adding a

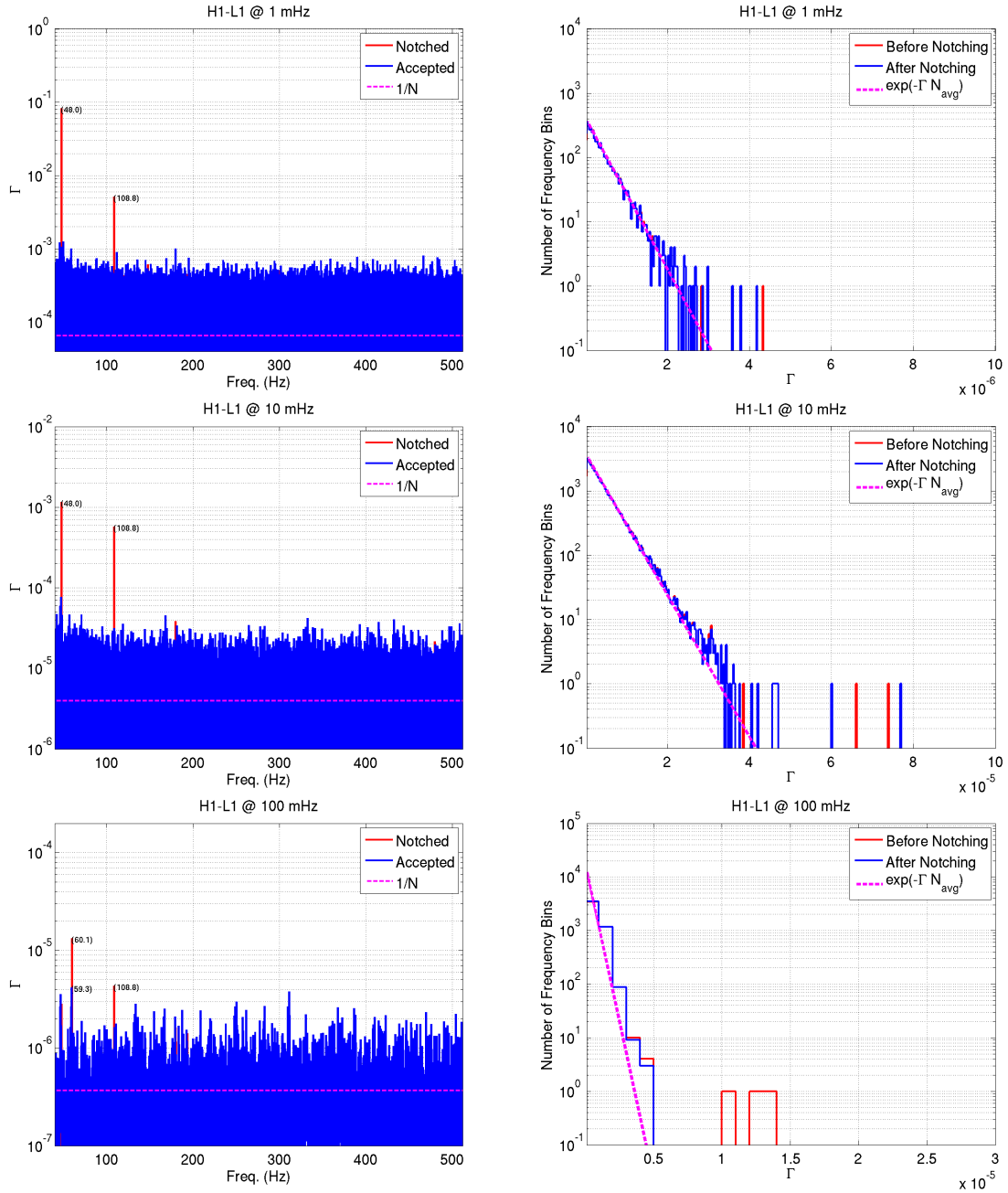


Figure 2.4: Coherence Γ_{12} between H1 and L1 computed in the frequency band 40–512 Hz using all of the S5 data, for three different frequency resolutions: 1 mHz, 10 mHz, and 100 mHz (top-to-bottom). Plots on the left show Γ_{12} as a function of frequency while plots on the right show distribution of Γ_{12} . The distribution of Γ_{12} is expected to follow an exponential distribution for Gaussian noise. Here ‘accepted’ refers to the frequencies that were used for calculating Y_{final} .

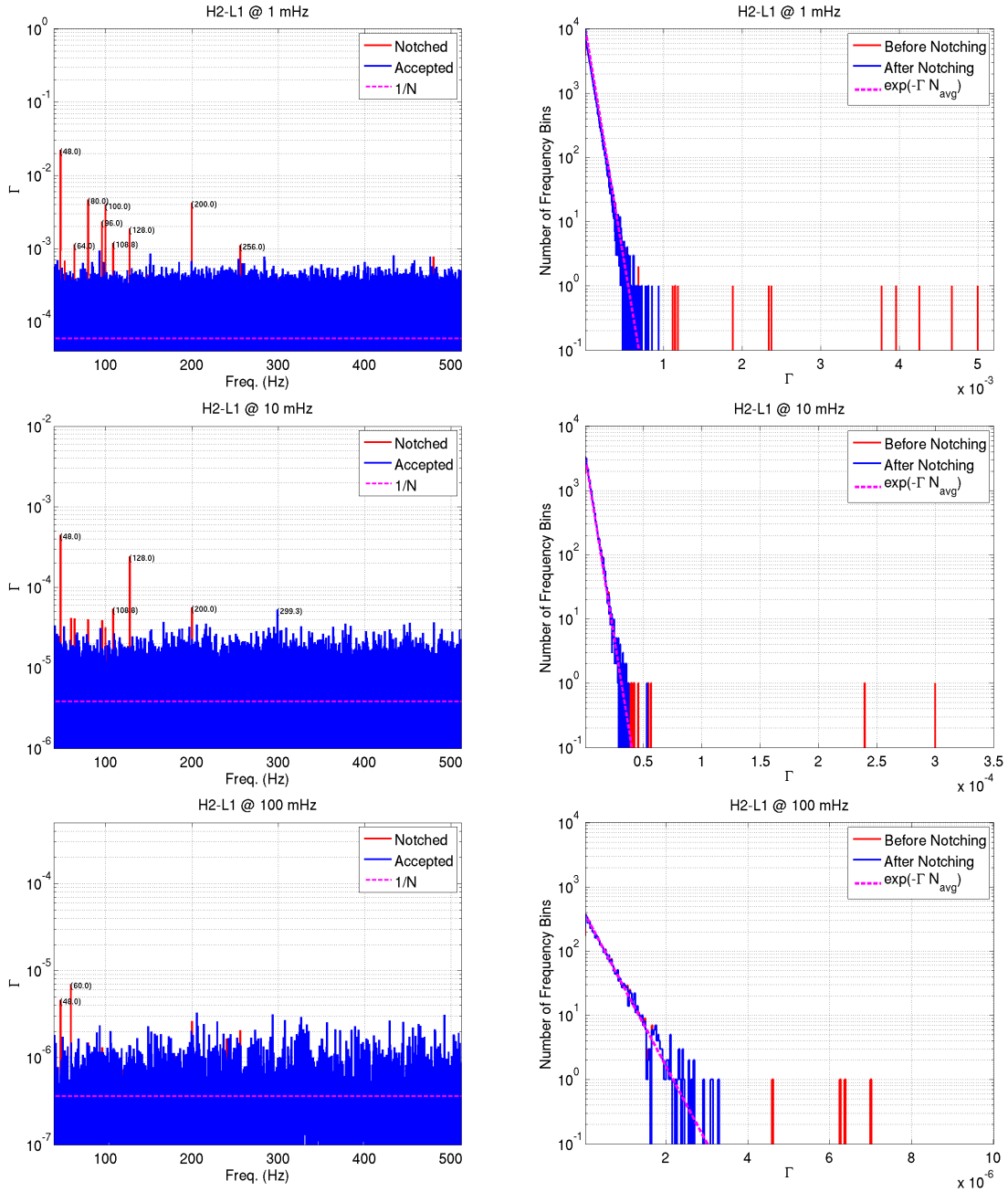


Figure 2.5: Coherence Γ_{12} between H2 and L1 computed in the frequency band 40–512 Hz using all of the S5 data, for three different frequency resolutions: 1 mHz, 10 mHz, and 100 mHz (top-to-bottom). Plots on the left show Γ_{12} as a function of frequency while plots on the right show distribution of Γ_{12} . The distribution of Γ_{12} is expected to follow an exponential distribution for Gaussian noise. Here ‘accepted’ refers to the frequencies that were used for calculating Y_{final} .

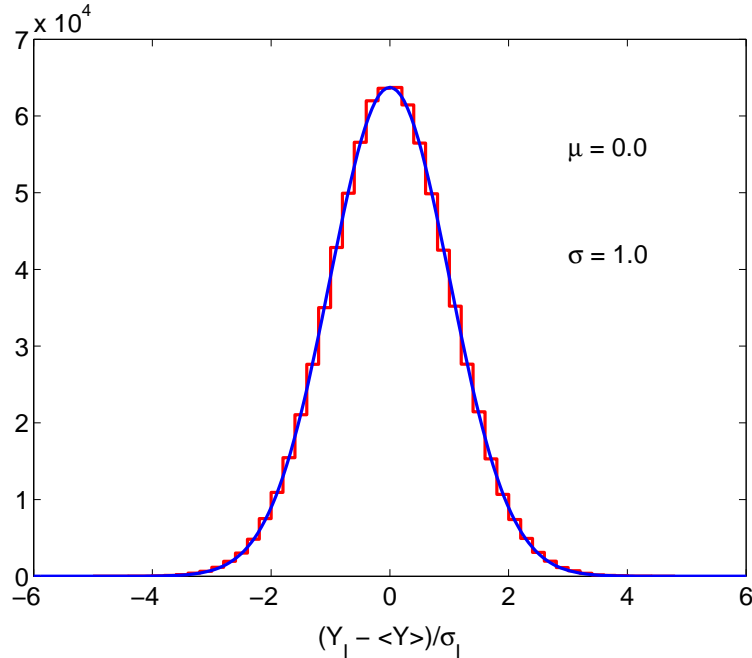


Figure 2.6: Histogram of the fluctuations of the estimator Y_I over segments I around the mean, normalized by the standard deviation σ_{Y_I} is shown in red (for the H1-L1 pair). The blue curve shows the Gaussian fit to the histogram, which has zero mean and unit variance. The Kolmogorov-Smirnov test statistic (comparing the histogram and the fit) is 0.2 for H1-L1 (0.4 for H2-L1), indicating that the data is indeed Gaussian-distributed, and that the estimate of the theoretical variance $\sigma_{Y_I}^2$ is reliable. Figure published in [42].

long and relatively weak stochastic signal to the interferometer data. Three hardware simulations were performed, with amplitudes of $\Omega_0 \approx 2$ (20 min long), 2×10^{-2} (20 min long), and 6.5×10^{-3} (~ 3.8 hours long) and they were successfully recovered (within experimental uncertainties) for both H1-L1 and H2-L1 pairs. A software simulation was performed and successfully recovered using about 1/2 of the H1-L1 data, with the amplitude of $\Omega_0 = 3.8 \times 10^{-5}$. Figure 2.7 and Figure 2.8 demonstrate the recovery of both hardware and software simulations.

2.4.3 Final results and implications

Figure 2.9 shows the final spectra for $Y(f)$ and $\sigma(f)$ (for a $\Omega_{gw}(f)$ spectrum with $\alpha = 0$ and $f_{ref} = 100$ Hz) after combining the results from H1-L1 and H2-L1 pairs. Integrated

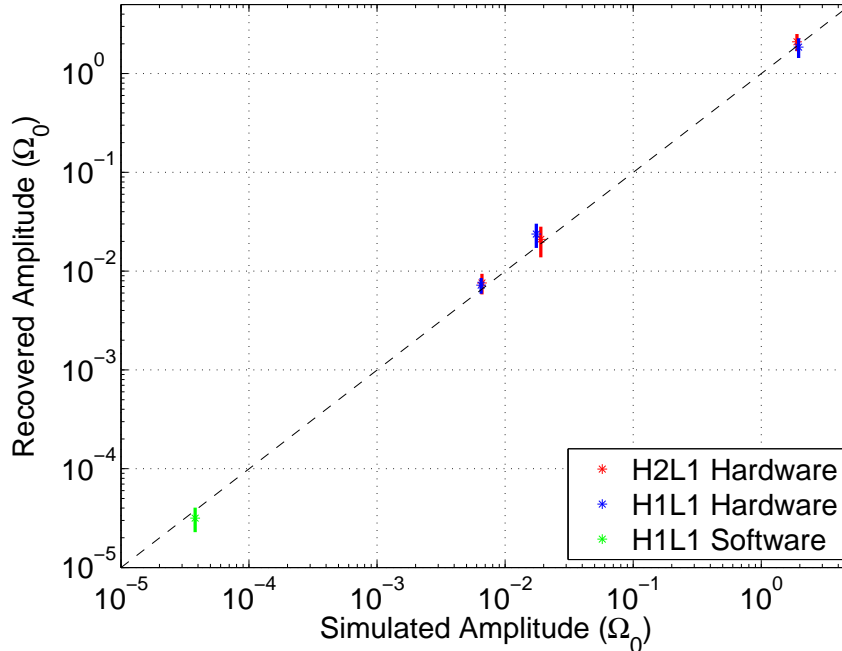


Figure 2.7: Stochastic signal simulations in hardware for H1-L1 (blue) and H2-L1 (red), and in software (H1-L1, green) are shown. The error bars denote 2σ ranges. Figure published in [42].

over the frequency band 41.5-169.25 Hz, which contains 99% of the sensitivity this lead to the final estimate for the frequency independent GW spectrum: $\Omega_0 = (2.1 \pm 2.7) \times 10^{-6}$, where the quoted error is statistical. For Hubble parameter, we use the value of 72 km/(Mpc – sec) [27]. We calculate the Bayesian posterior distribution for Ω_0 using this result. For the prior distribution of Ω_0 we use our previously published posterior distribution from the earlier S4 run [7]. As described in Section 2.3.3, we marginalize over the calibration uncertainty, which was the dominant systematic error in this analysis and was estimated to be 13.4% for L1 and 10.3% for H1 and H2. With these assumptions, the final 95% confidence upper limit was $\Omega_0 < 6.9 \times 10^{-6}$ [42]. Figure 2.10 shows the 90% confidence upper limit as a function of the power index α in the range between -3 and 3. These results constitute more than an order of magnitude improvement over the previous LIGO result in this frequency region [7]. Figure 2.11 shows this result in comparison with other observational constraints and some of the cosmological SGWB models.

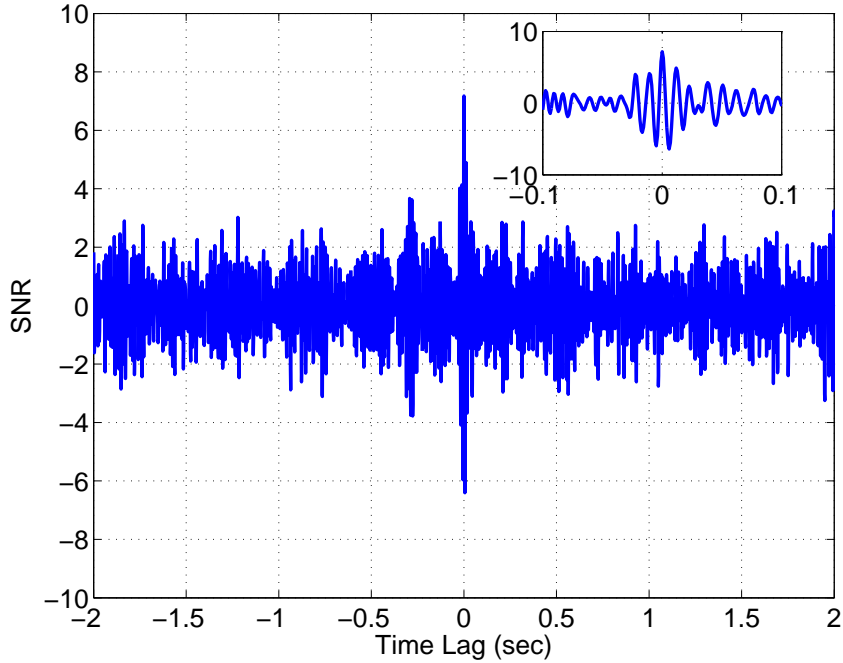


Figure 2.8: Signal-to-noise ratio for the recovery of a software simulation with H1-L1 data with $\Omega_0^{simulated} = 3.8 \times 10^{-5}$ is shown as a function of the time-lag between the two interferometers. The inset shows the zoom-in around zero-lag: the signal is recovered well for zero-lag ($\text{SNR} \approx 7.2$), but it disappears quickly with time-lag of ± 30 ms. Figure published in [42].

Prior to the result described here, the most constraining bounds on the SGWB in the frequency band around 100 Hz came from the BBN and CMB measurements (cf. Section 2.1.3). In the LIGO frequency band, 41.5 - 169.25 Hz, and for $\alpha = 0$, these bounds become: $\Omega_0^{\text{BBN}} < 1.1 \times 10^{-5}$ and $\Omega_0^{\text{CMB}} < 9.5 \times 10^{-6}$. Our result presented here surpasses these bounds and is considered one of the major results from initial LIGO analyses. Moreover, the BBN and CMB bounds apply only to backgrounds generated prior to the BBN and the CMB decoupling respectively, while the LIGO bound also probes the SGWB produced later (this is the case, for example, in cosmic strings models and astrophysical models).

Our result also constrains models of the early universe evolution. While the evolution of the universe following the BBN is well understood, there is little observational data probing the evolution prior to BBN, when the universe was less than one minute old. The GW spectrum $\Omega_{\text{gw}}(f)$ carries information about this epoch in the evolution. In particular,

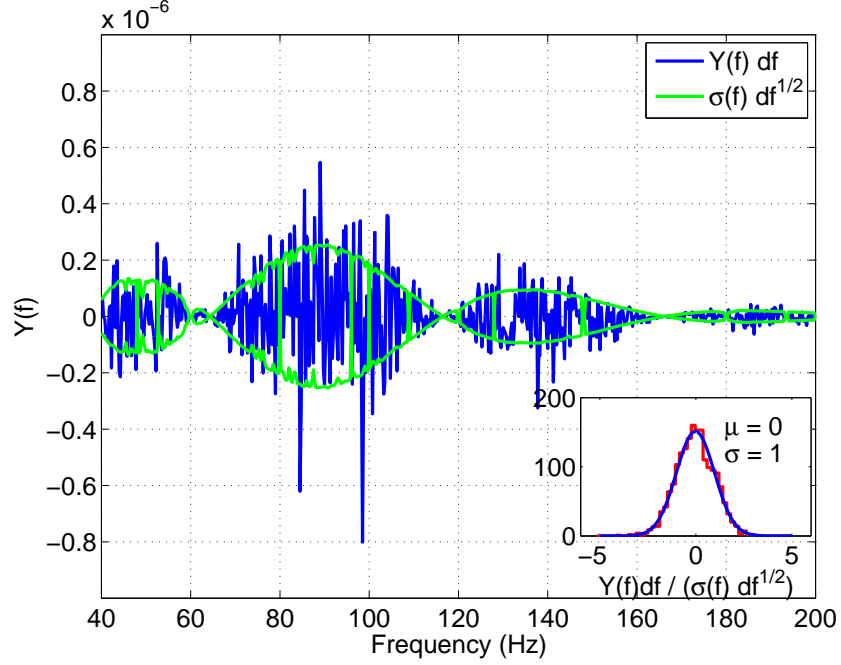


Figure 2.9: $Y(f)$ and $\sigma(f)$ obtained by combining the H1-L1 and H2-L1 data from the S5 run. The inset shows that the ratio of the two spectra is consistent with a Gaussian of zero mean and unit variance. Figure published in [42].

measuring $\Omega_{\text{gw}}(f)$ is the best way to test for existence of presently unknown “stiff” energy components in the early universe [32], for which a small density variation is associated with a large pressure change, which could carry information about the physics of the inflationary era [84]. In the framework of [32], the GW spectrum $\Omega_{\text{gw}}(f)$ is related to the parameters that govern the evolution of the universe by the relation:

$$\Omega_{\text{GW}}(f) = A f^{\hat{\alpha}(f)} f^{\hat{n}_t(f)} r \quad (2.54)$$

where

$$\hat{\alpha}(f) = 2 \frac{3\hat{w}(f) - 1}{3\hat{w}(f) + 1}, \quad (2.55)$$

r is the ratio of tensor and scalar perturbation amplitudes (measured by CMB experiments), $\hat{n}_t(f)$ and $\hat{w}(f)$ are effective (average) tensor tilt and equation of state parameters respectively, and A is a constant depending on various cosmological parameters. Hence,

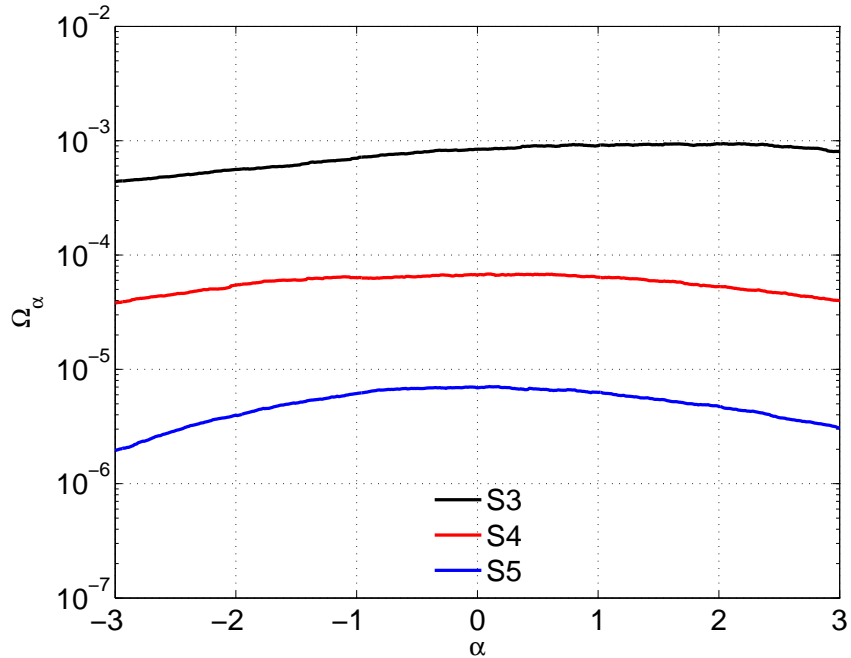


Figure 2.10: 90% confidence upper limit is shown as a function of the power index α for several LIGO results: based on the previous runs S3 and S4 and the S5 result presented here. Figure published in [42].

the measurements of Ω_{gw} and r can be used to place constraints in the $\hat{w} - \hat{n}_t$ plane, *independently* of the cosmological model. The Figure 2.12 shows the $\hat{w} - \hat{n}_t$ plane for $r = 0.1$. The regions above the curves are excluded. Also shown is the expected reach of Advanced LIGO [71]. Note that these bounds apply to different frequency bands, so their direct comparison is meaningful only if $\hat{n}_t(f)$ and $\hat{w}(f)$ are frequency independent. We note that for the simplest single-field inflationary model that still agrees with the cosmological data, $V(\phi) = m^2\phi^2/2$, $r = 0.14$ and $n_t(100 \text{ Hz}) = -0.035$ [100], implying a LIGO bound on the equation-of-state parameter of $\hat{w}(100 \text{ Hz}) < 0.59$. The recent Planck measurements [41] exclude the $V(\phi) = m^2\phi^2/2$ model with 95% confidence, so this may not be very useful.

Figure 2.13 shows our result, along with other observations, constraining the parameters in the cosmic string models (cf. Section 2.1.1). The network of cosmic strings is usually parametrized by the string tension $G\mu$, and reconnection probability p . If the size of the cosmic string loops is determined by the gravitational back-reaction [147], the size of the

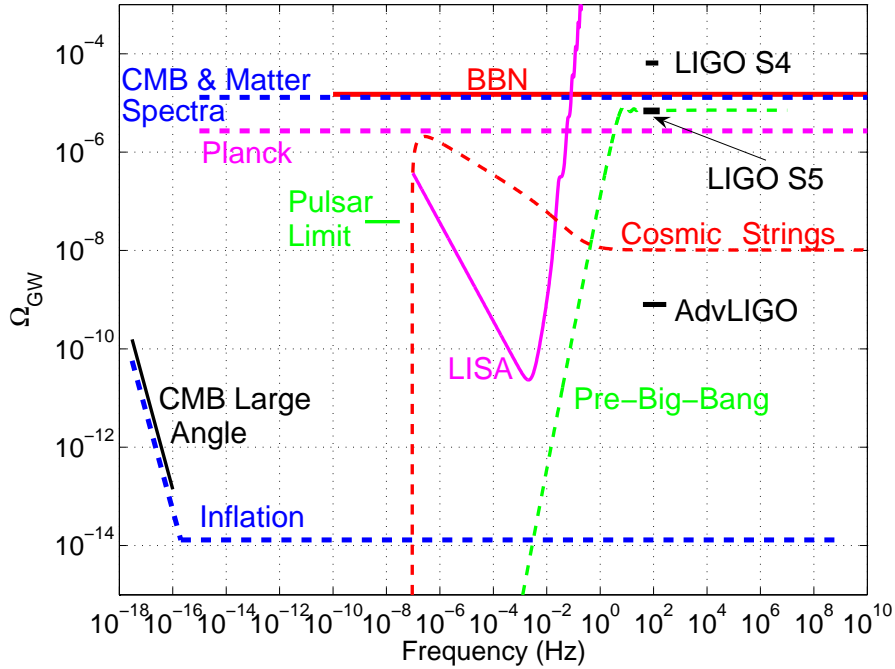


Figure 2.11: The result shown here (LIGO S5) applies in the frequency band around 100 Hz, and is compared to the previous LIGO S4 result [7] and to the projected Advanced LIGO sensitivity [71] in this band. The indirect bounds due to BBN [112, 18] and CMB and matter power spectra [153] apply to the integral of $\Omega_{\text{gw}}(f)$ over the frequency bands denoted by the corresponding dashed curves. Projected sensitivities of the satellite-based Planck CMB experiment [153] and LISA GW detector [25] are also shown. Figure published in [42].

loop can be parametrized by a parameter ϵ [49] which is essentially unconstrained. The Figure 2.13 shows constraints from different experiments, including our current result. While our result is currently excluding a fraction of the allowed parameter space, Advanced LIGO [71] is expected to probe most of the parameter space.

Figure 2.14 shows constraints on the Pre-Big-Bang models (cf. Section 2.1.1) using our results, along with constraints from BBN and CMB measurements. Currently BBN and CMB bounds are the most constraining ones, but Advanced LIGO [71] is expected to surpass them.

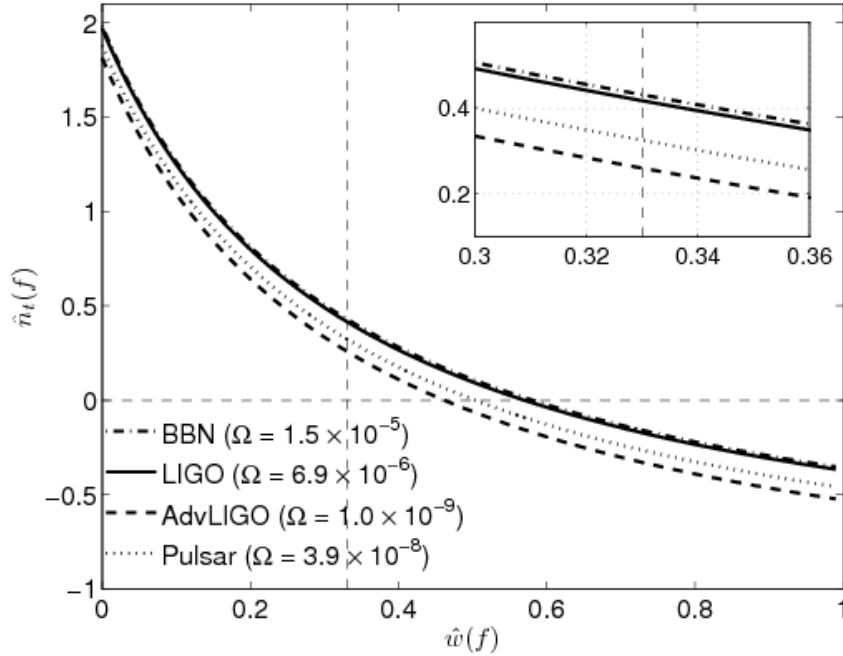


Figure 2.12: The above figure shows the $\hat{w} - \hat{n}_t$ plane for $r = 0.1$. The regions excluded by the BBN [47], LIGO, and pulsar [126] bounds are above the corresponding curves (the inset shows a zoom-in on the central part of the figure). The BBN curve was calculated in [32]. We note that the CMB bound [153] almost exactly overlaps with the BBN bound. Also shown is the expected reach of Advanced LIGO [71]. Figure published in [42].

2.5 Results using colocated LIGO detectors

At the end of Section 2.2 on cross-correlation statistic, we obtained an optimal filter that maximizes the signal-to-noise ratio of the final estimate $\langle Y \rangle (= T\Omega_\alpha)$. The optimal filter given by Eq. (2.44) is proportional to the overlap reduction function $\gamma(f)$ (Eq. (2.35)) which is shown in Figure 2.3. From the Figure 2.3, we see that for non-colocated detector pairs overlap reduction function is significant only in a small frequency band while for the colocated detector pair it is maximum and constant over all the frequencies. Hence by using a colocated detector pair we would be able improve SGWB measurement by at least an order magnitude, depending the frequency band we analyze. Thus, the colocated H1-H2 pair is not only another pair we can analyze, but is the most sensitive of all the three pairs. However this comes with a price of high noise correlation between the colocated detectors

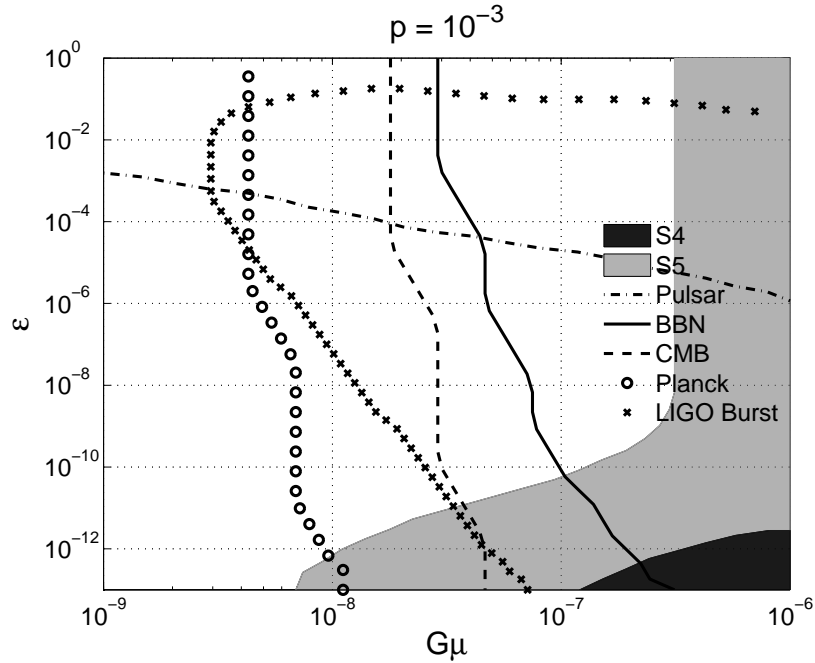


Figure 2.13: The above figure shows how different experiments probe the $\epsilon - G\mu$ plane for a typical value of $p = 10^{-3}$ [167] (p is expected to be in the range $10^{-4} - 1$). The excluded regions (always to the right of the corresponding curves) correspond to the S4 LIGO result [7], current result, BBN bound [18, 47], CMB bound [153], and the pulsar limit [126]. In particular, the bound presented here excludes a new region in this plane ($7 \times 10^{-9} < G\mu < 1.5 \times 10^{-7}$ and $\epsilon < 8 \times 10^{-11}$), which is not accessible to any of the other measurements. The entire plane shown here will be accessible to Advanced LIGO [71] SGWB search. Figure published in [42].

due to the local environment, which cannot be easily distinguished from a GW signal.

Most of the previous LIGO searches for stochastic GWs, including the one described in the previous section, had used physically-separated Hanford and Livingston detectors and assumed that common noise between the non-colocated detectors was inconsequential. The only exception was the first LIGO analysis (S1) searching for SGWB which studied the possibility of using colocated H1-H2 detectors and concluded that further investigations were required before using the colocated H1-H2 pair [6]. This assumption that common (or correlated) noise between non-colocated detectors is negligible was strongly supported by observations—i.e., none of the coherence measurements performed to date between these two detectors revealed the presence of correlations other than those known to be introduced

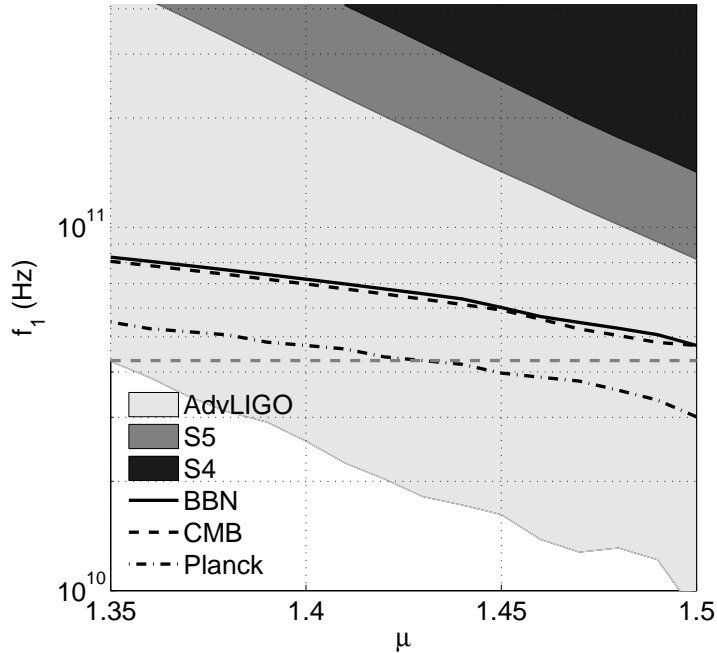


Figure 2.14: The above figure shows the $f_1 - \mu$ plane for a representative value of $f_s = 30$ Hz in Pre-Big-Bang models. Excluded regions corresponding to the S4 result and to the result presented here are shaded. The regions excluded by the BBN [18, 47] and the CMB [153] bounds are above the corresponding curves. The expected reaches of the Advanced LIGO [71] and of the Planck satellite [153] are also shown. Figure published in [42].

by the instrument itself (for example, harmonics of the 60 Hz power line). But for the colocated detector pair this is not the case and as concluded in the S1 paper [6], this pair suffers from excess correlated noise at many frequencies.

Even though non-colocated detector pairs do not suffer from strong correlations, as mentioned in Section 2.4.1, 60 Hz harmonics and other instrumental lines do affect the widely separated LIGO detectors. These lines could be problematic for other GW searches looking for short and/or narrowband GWs such as CBC signals. In order to discriminate between such local noise lines and GWs, in addition to the interferometers, each of the LIGO observatory sites is supplemented with a set of sensors to monitor the local environment [6, 12]. Seismometers and accelerometers measure vibrations of the ground and various interferometer components; microphones monitor acoustic noise; magnetometers monitor magnetic fields that could couple to the test masses via the magnets attached to the test masses

to control their positions; radio receivers monitor radio frequency (RF) power around the laser modulation frequencies and voltage line monitors record fluctuations in the AC power. These physical environment monitoring (PEM) channels are used to detect instrumental and environmental disturbances that can couple to the GW strain channel.

Information provided by the PEM channels is used in many different ways. The most basic application is the creation of numerous *data quality flags* identifying stretches of data that are corrupted by instrumental or environmental noise [29], some of which were used in the initial selection of data described in Section 2.3.1.

2.5.1 PEM coherence studies

In Section 2.3.2 we described a couple of methods for identifying contaminated frequencies in the cross-correlated data. Here we describe another method, called PEM-coherence method, based on the information from PEM channels. This method was applied only to colocated H1-H2 detector pair (due to expected high correlations).

New definitions of signal estimators

Before describing the method, we first (re-)define the signal estimator and its variance in each frequency bin to simplify the process of removing noisy frequency bins. The definition used in Eq. (2.33) is not convenient, because it is defined as an integral and not as a weighed sum over frequency bins. Using Eqs. (2.16), (2.33) and (2.44), we define the estimator of Ω_α as,

$$\hat{\Omega}_\alpha(f) \equiv \frac{2}{T} \frac{\Re[\tilde{s}_1^*(f)\tilde{s}_2(f)]}{\gamma(f)S_\alpha(f)}, \quad (2.56)$$

where T is the duration of the data segments used for Fourier transforms, $\tilde{s}_1(f)$, $\tilde{s}_2(f)$ are the Fourier transforms of the strain time-series from the two detectors, $S_\alpha(f)$ is the assumed spectral shape given by

$$S_\alpha(f) \equiv \frac{3H_0^2}{10\pi^2} \frac{1}{f^3} \left(\frac{f}{f_{\text{ref}}} \right)^\alpha. \quad (2.57)$$

We note that the previous estimator defined by Eq. (2.33) and the new estimator defined here are the same, except for the factor of T (cf. end of Section 2.2). The variance of Ω_α is given by,

$$\sigma_{\hat{\Omega}_\alpha}^2(f) \approx \frac{1}{2T\Delta f} \frac{P_1(f)P_2(f)}{\gamma^2(f)S_\alpha^2(f)}, \quad (2.58)$$

where $P_1(f)$, $P_2(f)$ are the one-sided PSDs of the detector time-series. For a frequency band consisting of several bins of width Δf , the optimal estimator and corresponding variance are given by the weighted sum

$$\hat{\Omega}_\alpha \equiv \frac{\sum_f \sigma_{\hat{\Omega}_\alpha}^{-2}(f) \hat{\Omega}_\alpha(f)}{\sum_{f'} \sigma_{\hat{\Omega}_\alpha}^{-2}(f')}, \quad \sigma_{\hat{\Omega}_\alpha}^{-2} \equiv \sum_f \sigma_{\hat{\Omega}_\alpha}^{-2}(f). \quad (2.59)$$

This is similar to the weighted sum given by Eq. (2.46), but Eq. (2.46) is defined for combining data from different time segments, while (2.59) is defined for combining estimates from different frequencies. This definition of signal estimator unifies the way we combine time and frequency domain data.

PEM-coherence method

In this new method we first try to identify the noise sources that couple into the individual detector outputs by calculating the coherence of \tilde{s}_1 and \tilde{s}_2 with various PEM channels \tilde{z}_I :

$$\gamma_{iI}(f) \equiv \frac{2}{T} \frac{\langle \tilde{s}_i^*(f) \tilde{z}_I(f) \rangle_N}{\sqrt{\langle P_i(f) \rangle_N \langle P_I(f) \rangle_N}}. \quad (2.60)$$

Here $i = 1, 2$ labels the detector outputs and I labels the PEM channels. For our analysis we used 172 PEM channels located near the two interferometers. The Fourier transforms are calculated for each minute of data ($T = 60$ s), and the average CSDs and PSDs are computed for extended time-periods—weeks, months, or the entire run. We then perform the following maximization over all PEM channels, for each frequency bin f , defining:

$$\gamma_{12,\text{PEM}}(f) \equiv \max_I \Re[\gamma_{1I}(f) \times \gamma_{I2}(f)]. \quad (2.61)$$

Note that by construction $\gamma_{12,\text{PEM}}(f)$ is real.

As discussed in [72], $\gamma_{12,\text{PEM}}(f)$ is an estimate of the instrumental or environmental contribution to the coherence between the GW channels of H1 and H2. This estimate is only approximate and suffers from systematic errors for a few reasons. First, the PEM coverage of the observatory may be incomplete—i.e., there may be environmental or instrumental effects that are not captured by the existing array of PEMs. Second, some of the PEM channels may be correlated. Hence, a rigorous approach would require calculating a matrix of elements $\gamma_{IJ}(f)$, and then inverting this matrix. In practice, due to the large number of channels and the large amount of data, this is a formidable task. Instead, we simply maximize, frequency-by-frequency, over the contributions from different PEM channels and use this maximum as an estimate of the overall environmental contribution to $\gamma_{12}(f)$. Since the measured signal-to-noise ratio for the estimator $\hat{\Omega}_\alpha(f)$ can be written as

$$\text{SNR}(f) = \sqrt{2T\Delta f} \Re[\gamma_{12}(f)] , \quad (2.62)$$

we can simply approximate the contribution of the PEM channels to the stochastic GW signal-to-noise ratio as

$$\text{SNR}_{\text{PEM}}(f) \equiv \sqrt{2T\Delta f} \gamma_{12,\text{PEM}}(f) , \quad (2.63)$$

remembering that $\gamma_{12,\text{PEM}}(f)$ is real. The PEM contribution to the estimators $\hat{\Omega}_\alpha(f)$ is then given by

$$\hat{\Omega}_{\alpha,\text{PEM}}(f) \equiv \text{SNR}_{\text{PEM}}(f) \sigma_{\hat{\Omega}_\alpha}(f) , \quad (2.64)$$

where $\sigma_{\hat{\Omega}_\alpha}(f)$ is the statistical uncertainty defined by Eq. (2.58). We can use the PEM coherence calculations in two complementary ways. First, we can identify frequency bins with particularly large instrumental or environmental contributions by placing a threshold on $|\text{SNR}_{\text{PEM}}(f)|$ and excluding them from the analysis. Second, the frequency bins that are not removed by this data-quality cut may still contain some residual environmental contamination. We can estimate at least part of this residual contamination by using $\hat{\Omega}_{\alpha,\text{PEM}}(f)$ in these remaining frequency bins.

As a part of the analysis procedure, we were able to identify the PEM channels that were responsible for the largest coherent noise between the GW channels in H1 and H2 for each frequency bin. We found that microphones and accelerometers in the central building near the beam splitters of each interferometer registered the most significant noise. Within approximately 1 Hz of the 60-Hz harmonics, magnetometers and voltage line monitors registered the largest correlated noise, but these frequencies were already removed from the analysis due to significant coherence levels (cf. Figure 2.15).

We emphasize here that the PEM channels only monitor the instrument and the environment, and are not sensitive to GWs. Similarly, the time-shift analysis, with a time-shift of ± 1 sec, is insensitive to broad-band GW signals. Hence, any data-quality cuts based on the PEM and time-shift studies will not affect the astrophysical signatures in the data—i.e., they do not bias our estimates of the amplitude of stochastic GW background.

2.5.2 Data quality cuts

We present here the results from coherence and time-shift studies performed to identify and remove narrowband correlations similarly to what was done for non-colocated detector pairs.

Coherence studies

Figure 2.15 shows coherence calculations done for the H1-H2 pair. Plots of $\Gamma_{12}(f)$ for three different frequency resolutions are shown in Figure 2.15, for the frequency band 80–160 Hz. In Figure 2.15, note the relatively wide structure around 120 Hz, which is especially prominent in the bottom panel where the frequency resolution is 100 mHz. This structure arises from low-frequency noise (dominated by seismic and other mechanical noise) up-converting to frequencies around the 60 Hz harmonics via a bilinear coupling mechanism. While these coupling mechanisms were not fully understood, we rejected the band 102–126 Hz from our analysis, given the elevated correlated noise seen in this band. A closer look at the coherence also identified smaller structures at 86–90 Hz, 100 Hz, 140–141 Hz, and 150 Hz. A followup analysis of PEM channels revealed that the highlighted bands in Figure 2.15 were highly contaminated with acoustic or seismic (upconverted) noise. So we

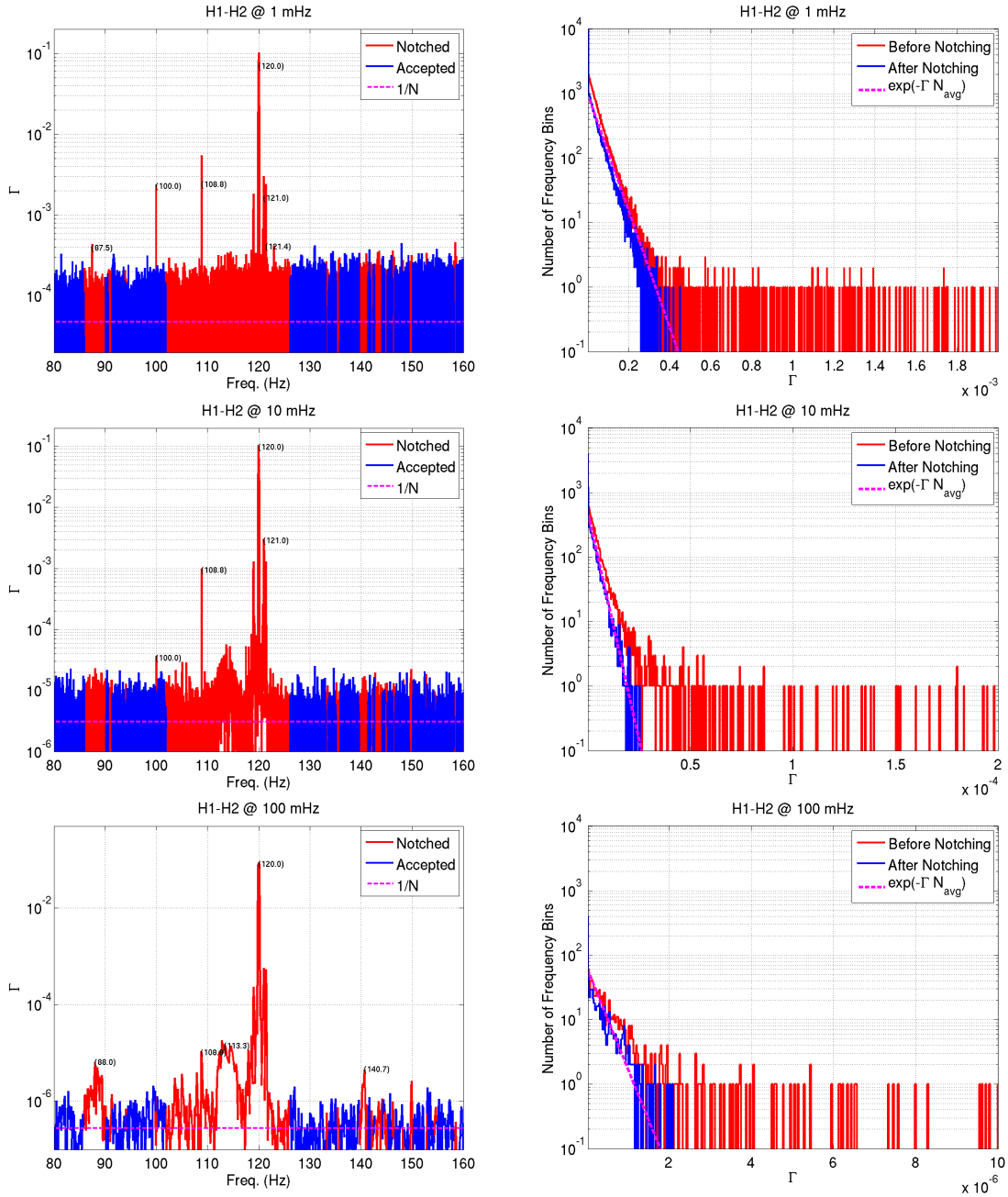


Figure 2.15: Coherence Γ_{12} between H1 and H2 computed in the frequency band 80–160 Hz using all of the S5 data, for three different frequency resolutions: 1 mHz, 10 mHz, and 100 mHz (top-to-bottom). Plots on the left show Γ_{12} as a function of frequency while plots on the right show distribution of Γ_{12} . The distribution of Γ_{12} is expected to follow an exponential distribution for Gaussian noise. Here 'accepted' refers to the frequencies that were used for further analyses.

rejected these frequency bands also from subsequent analysis.

Time-shift

Using segments of duration $T = 1$ sec and time-shift of ± 1 sec, we calculated the time-shifted estimators $\hat{\Omega}_{\alpha, \text{TS}}(f)$, variance $\sigma_{\hat{\Omega}_{\alpha, \text{TS}}(f)}^2$, and signal-to-noise ratio $\text{SNR}_{\Omega_{\alpha, \text{TS}}(f)} \equiv \hat{\Omega}_{\alpha, \text{TS}}(f)/\sigma_{\hat{\Omega}_{\alpha, \text{TS}}(f)}$. The calibration and conditioning of the data was performed in same way as for the non-colocated detectors. We removed frequency bin with $|\text{SNR}_{\Omega_{\alpha, \text{TS}}(f)}|$ greater than 2 (a threshold based on studies done on a test data set).

2.5.3 Hardware and software injections

We validated our analysis procedure by injecting simulated stochastic GW signals into the strain data of the two detectors. Both hardware and software injections were performed. During S5 there was one stochastic signal hardware injection when both H1 and H2 were operating in coincidence. A stochastic background signal with spectral index $\alpha = 0$ and amplitude $\Omega_0 = 6.60 \times 10^{-3}$ was injected for approximately 3 hours. In performing the analysis, frequency bins were excluded based on the standard H1-H2 coherence calculations. No additional frequency bins were removed using SNR_{PEM} . The recovered signal was $\Omega_0 = (6.49 \pm 0.04) \times 10^{-3}$, consistent with the injected amplitude within 3σ . We also performed ten software injection trials with an injection amplitude of $\Omega_0 = 1.10 \times 10^{-5}$. In each trial, we time-shifted the output of one interferometer relative to the other before adding the simulated stochastic signal. The time-shift was different in each trial, allowing for an independent realization of the noise in each trial. In Figure 2.16 (left panel), the inverse Fourier transform of $\hat{\Omega}_0(f)$ is shown for one of the ten trials; the presence of the signal is clear from the sharp peak at zero-lag. Figure 2.16 (right panel) shows the recovered amplitudes for the 10 trials.

2.5.4 Final Results

The H1-H2 analysis was done in two parts corresponding to searches for stochastic GW background with spectral index $\alpha = 0$ (80–160 Hz) and $\alpha = 3$ (400 – 1000 Hz). Since the

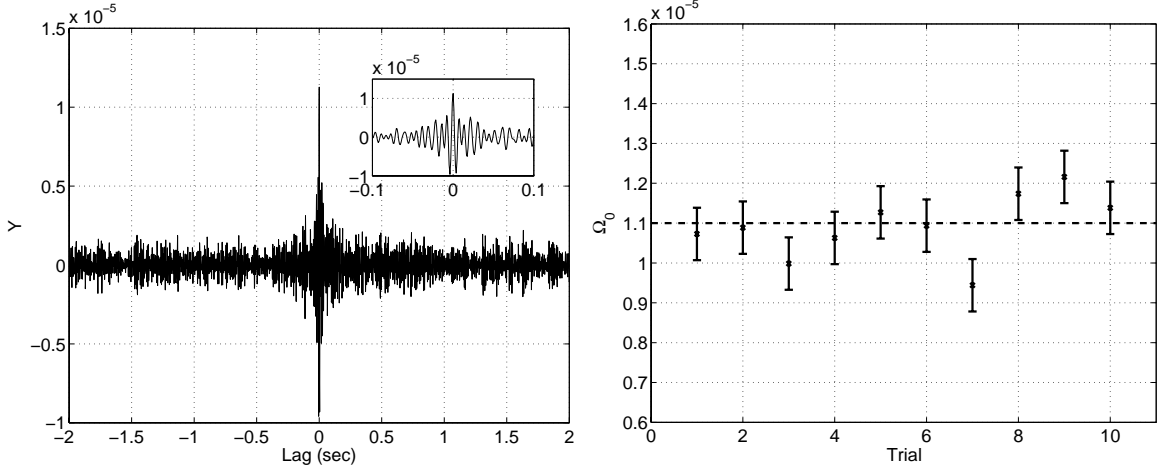


Figure 2.16: Left panel: The inverse Fourier transform of $\hat{\Omega}_0(f)$ for an $\text{SNR}_{\Omega_0} \approx 15$ software signal injection in the H1-H2 data with $\Omega_0 = 1.10 \times 10^{-5}$. Note that the signal decoheres on a time-scale of order 10 ms, which justifies the ± 1 s time-shifts used to identify noise correlations in the time-shift method. Right panel: Recovered amplitudes for 10 software injection trials, along with $\pm \sigma_{\hat{\Omega}_0}$ error bars. The injected signal, denoted by the dashed line, in each case was $\Omega_0 = 1.10 \times 10^{-5}$.

strain power output of an interferometer due to GWs, $S_{gw}(f) \propto f^{\alpha-3}$ (see Eq. (2.57)), $\alpha = 0$ case is dominated by low frequencies while $\alpha = 3$ case is independent of frequency. In this thesis we only report analysis and results of the low frequency region and make occasional remarks on the high frequency region when necessary.

Below are the five stages of noise removal we performed in this analysis.

- Step 1: Initial data selection as described in Section 2.3.1.
- Step 2: Identification and removal of segments with short noise transients using Kleine Welle algorithm [39].
- Step 3: Noisy frequency bins removal using coherence and time-shift methods.
- Step 4: Stationarity cut with $\epsilon = 0.2$ (removed about 22% of the data)
- Step 5: Removal of additional frequency bins using PEM-coherence method. This was done on weekly, monthly and full run basis.

To illustrate the effect of the various noise removal methods enumerated above, below we provide the results as different stages of cuts were applied to the data (see Table 2.1 for the definition of different stages). The cut threshold values used at stage III came from an initial study performed using playground data to understand the effectiveness of PEM-coherence and time-shift methods in finding problematic frequency bins. Hence those results were considered as *blind analysis* results. But a post-unblinding study showed that we could lower the SNR_{PEM} threshold to values as low as 0.5 and were used at stage IV. These results were considered as post-unblinding results and were used in the final estimates. For threshold values < 0.5 , the PEM-coherence contribution, $\hat{\Omega}_{\alpha, \text{PEM}}$, varied rapidly as the threshold was changed indicating the statistical noise limit of the PEM-coherence method.

Stage	Steps	% of data vetoed
I	Step 1	8.51
II	Steps 1–4	56.01
III	Steps 1–5 with $ \text{SNR}_{\text{PEM}} > 2$, $ \text{SNR}_{\text{TS}} > 2$	72.06
IV	Steps 1–5, with $ \text{SNR}_{\text{PEM}} > 0.5$, $ \text{SNR}_{\text{TS}} > 2$	76.34

Table 2.1: Definition of various stages of noise removal in terms of the analysis steps described in Section 2.5.4. Here stage III is corresponds to the blind analysis and stage IV to post-unblinding analysis.

Table 2.2 summarizes the results for the low-frequency analysis after applying several stages of noise removal as defined in Table 2.1. Figure 2.17 shows the results obtained by applying the noise removal cuts in four stages. The left column of plots contains the estimators, $\hat{\Omega}_0(f)$ and $\hat{\Omega}_{0, \text{PEM}}(f)$ along with the statistical error bar $\pm \sigma_{\hat{\Omega}_0}(f)$, and the right column of plots shows the estimator $\hat{\Omega}_0(f)$ as a function of time lag between the two detectors. If there was no correlation between the detectors, we would expect no structure in those plots. For un-correlated noise there is no preferred time lag while for GW signal as well as for correlated noise zero-lag corresponds to maximum correlation and the correlation decreases as we move away from zero-lag. Also for broadband GW signal the correlation

Stage	$\hat{\Omega}_0$ ($\times 10^{-6}$)	$\hat{\Omega}_{0,\text{PEM}}$ ($\times 10^{-6}$)	$\sigma_{\hat{\Omega}_0}$ ($\times 10^{-6}$)	std/ σ_{Ω_0}
I	5.50	-0.41 [†]	0.39	5.82
II	-1.53	-0.81	0.56	1.78
III	-1.94	-0.70	0.70	1.56
IV	-0.99	-0.20	0.75	1.58

Table 2.2: The different rows correspond to results obtained after various stages of noise removal. [†] The PEM-coherence estimate on stage I also excludes frequencies (such as 60 Hz harmonics) and time segments similar to stages II-IV.

decreases much faster than any relatively narrowband noise correlation. Thus the structures we see in time-lag Vs Ω_0 plots correspond to correlated noise. This indicates the presence of residual correlated noise even after all the time-shift and PEM-coherence noise removal cuts are applied. In contrast, we observed no such structure in the high-frequency plots after all the cuts applied.

Since we could not remove all the correlated noise in the 80 – 160 Hz band even after applying all the noise removal cuts, in this band we place a 95% upper C.L. limit on the sum of GW energy density and residual correlated noise of $\Omega_0 + \eta_0 < 7.0 \times 10^{-6}$ with $\alpha = 0$ (preliminary; under internal review). But for the 460 – 1000 Hz band, we were able mitigate the effects of correlated noise, and so we place a 95% upper C.L. limit on the GW energy density alone in this band of $\Omega_3 < 8.4 \times 10^{-4}$ (preliminary; under internal review). This limit improves on the previous best limit in the high-frequency band by a factor of > 350 [5]. Figure 2.18 shows the upper-limits from the current analysis and from previous stochastic analyses, along with the projected limit using advanced LIGO.

2.6 Summary

In this chapter, we described searches for stochastic GWs using data acquired by three LIGO detectors. The result from non-colocated detector pairs (H1-L1 and H2-L1) set a 95% C.L. upper limit $\Omega_0 < 6.9 \times 10^{-6}$ surpassing BBN and CMB limits in LIGO frequency band (41.5 – 169.25 Hz). The colocated detector pair suffered from high correlated noise and we

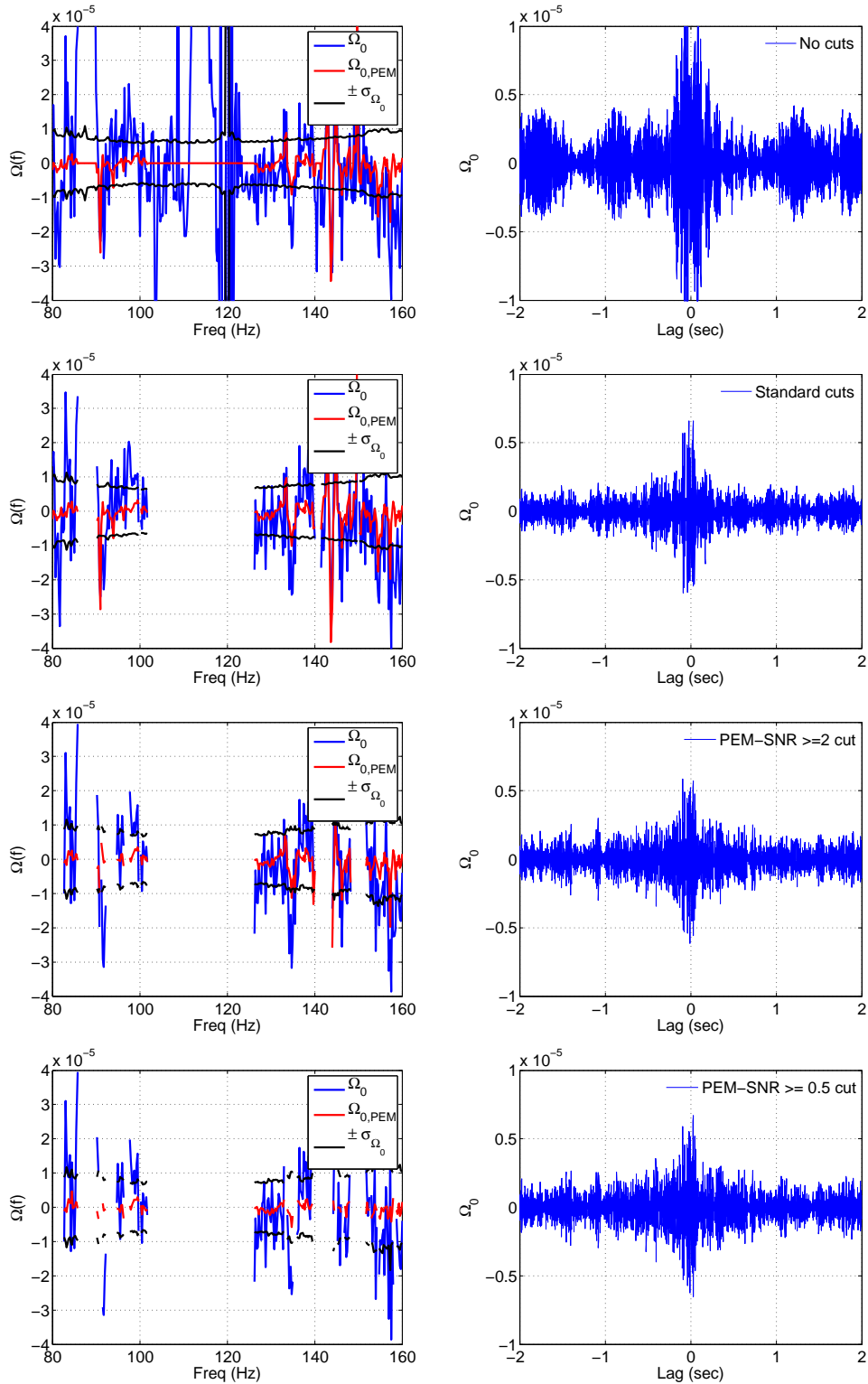


Figure 2.17: Plots of $\hat{\Omega}_0(f)$ and $\hat{\Omega}_{0,PEM}(f)$ (left), and the inverse Fourier transform of $\hat{\Omega}_0(f)$ (right) for the 80–160 Hz band after various stages of noise removal were applied to the data. The four rows correspond to four different stages of cleaning defined in Table 2.1.

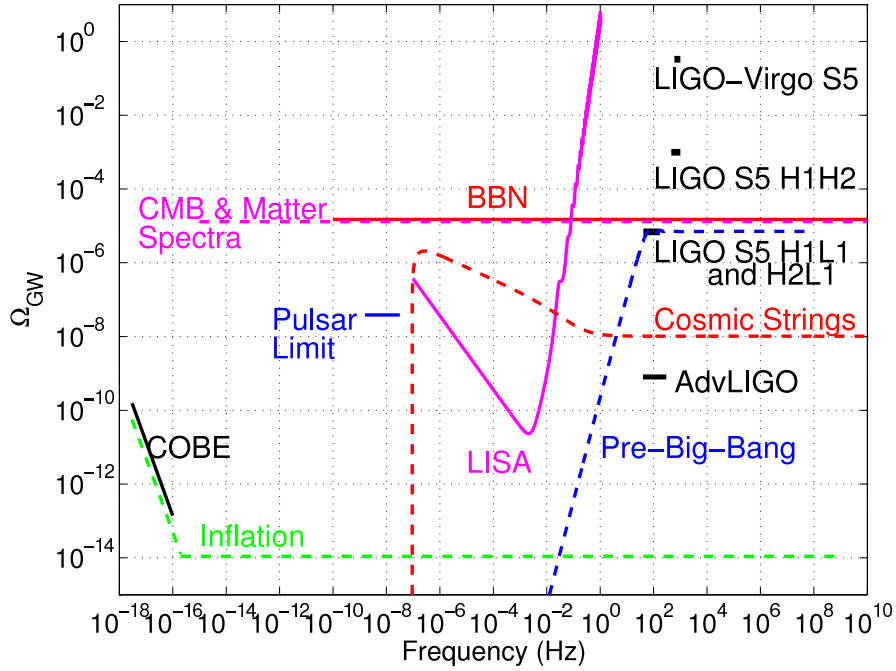


Figure 2.18: The above figure shows upper limits from current/past SGWB analyses, as well as indirect limits from Big Bang Nucleosynthesis (BBN), and projected limits using Advanced LIGO. Indirect limits from BBN apply to SGWBs present in the early universe at the time of BBN, but not to SGWBs of astrophysical origin created more recently. The $\alpha = 3$ bound on astrophysical SGWB presented here improves on the previous best limit by a factor of $>350x$. It complements the indirect bound from the BBN, which is only sensitive to cosmological SGWBs from the early universe, as well as direct $\alpha = 0$ measurements using lower-frequency observation bands [14].

applied, in addition to methods used for non-co-located pairs, a new PEM-coherence method to identify and remove some of those noise correlations. The methods proved to be useful in cleaning the high-frequency band, but not sufficient in the low-frequency band. The high frequency result set a 95% C.L. upper limit $\Omega_3 < 8.4 \times 10^{-4}$ (preliminary; under internal review) in the frequency band 400 – 1000 Hz which is $>350x$ better than the previous limit in this band.

Chapter 3

Searches for long GW transients

Gravitational waves with time scales ranging from milliseconds to weeks are called GW transients. The upper limit of weeks is not a strict one but if they extend far beyond that then they are considered as continuous or persistent signals. For example, stochastic GW signals that we discussed in Chapter 2 are examples of persistent signals. As we discussed in Section 1.2, searches for GW transients can be divided into two categories: searches for transients whose precise waveforms are hard to model and searches for transients such as compact binary coalescences whose waveforms can be easily predicted. Historically, searches for GW transients with unknown waveforms focus on signals with duration $\lesssim 1$ s [2].

In this chapter, we focus on *long* GW transients whose duration may range from many seconds to weeks. There exist many compelling models of astrophysical scenarios that predict emission of long GW transients [124, 45, 130, 162]. There are not many analysis pipelines that could be used to search for long GW transients (for example see [132, 64, 104]). Here we introduce a new pipeline based on cross-correlation between two detectors.

In Section 3.1, we survey a range of mechanisms for GW emission that may lead to long transients. These include long-lived turbulent convection in protoneutron stars (PNSs), rotational instabilities in rapidly spinning PNSs and in double neutron-star merger remnants, magnetoturbulence and gravitational instabilities in gamma-ray bursts (GRBs) accretion torii, r -modes associated with accreting and newborn neutron stars, as well as, perhaps more speculatively, pulsar glitches and soft-gamma-repeater (SGR) outbursts.

In Section 3.2, we introduce an analysis framework utilizing frequency-time (ft)-maps

of GW strain cross-power created using data from two spatially separated detectors. The framework is then extended to include multiple detectors, and we show that it is a generalization of the GW radiometer algorithm [8]. In Section 3.3, we study pixel distributions of ft -maps and compare ft -cross-power maps of GW data (time-shifted to remove astrophysical content) with Monte Carlo simulations of idealized detector noise.

In Section 3.4, we describe methods to search for long GW transients in ft -cross-power maps using pattern recognition algorithms and illustrate the method using “box search” [20] as an example algorithm. We also briefly discuss a few other algorithms and use of the new analysis tool to identify environmental noise artifacts in LIGO data. In Section 3.5 we apply the transient GW pipeline developed here to search for GWs from gamma-ray bursts and provide preliminary results. Summary of the chapter is given in Section 3.6.

3.1 Sources of Long GW Transients

In this section, we review a few of the astrophysical sources of long GW transients. For a comprehensive review please refer to [124, 110, 159] and references therein. The astrophysical sources of long GW transients, in general, can be associated with one or more of three types of objects: core-collapse supernovae (CCSNe), compact binary inspirals, or isolated neutron stars.

3.1.1 Core-collapse supernovae

Massive stars at the end of their life undergo violent explosions releasing copious amount of energy in the form of electromagnetic radiation, neutrinos and mass ejecta. It is also widely believed that such violent explosions could be non-spherical in nature producing significant amount of GW radiation.

Currently there are two plausible scenarios by which massive stars, associated with strong electromagnetic emission called GRBs, could end their life. In the first scenario of collapsars [166], a massive star collapses to a black hole without explosion or with a weak explosion and fallback accretion. In the second scenario of protoneutron star [34, 157], after

a strong explosion the massive star forms a fast rotating intermediate nascent neutron star which then subsequently may form a black hole depending on accretion. In both scenarios, the accretion disk surrounding the black hole or PNS could undergo instabilities leading to GW emission [130, 162]. In addition to the instabilities in accretion disk, the PNS itself could undergo various non-axisymmetrical rotational instabilities producing GWs. Most of these mechanisms are expected to produce narrowband GWs with a slow frequency evolution. There are also other mechanisms such as PNS convection [124] that could produce GWs that are expected to be relatively broadband.

Accretion disk instabilities

In the collapsar scenario, the accretion disk surrounding the newly formed black hole undergoes various magneto-hydrodynamic instabilities leading to clumping or disk fragmentation. These clumps could inspiral towards the central black hole via viscous friction and/or GW emission. In [130], the authors predict maximum dimensionless strain amplitudes of $|h| \sim 2 \times 10^{-23} (f_{\text{GW}}/1000 \text{ Hz})^{2/3}$ for a system with fragment masses of $1M_{\odot}$, central black hole mass of $8M_{\odot}$, and at a distance of 100 Mpc. In this model, the frequency slowly increases over the emission interval, making the emission quasi-periodic and, thus, increasing its detectability by increasing its characteristic strain h_c up to $\mathcal{O}(\times 10^{-22})$ at $f_{\text{GW}} \sim 100 \text{ Hz}$.

It is also possible to have GW emission via magnetic coupling between accretion disk and the central black hole. In [161, 162, 163], the author proposes an extreme “suspended–accretion” scenario in which the central black hole and the accretion torus are dynamically linked by strong magnetic fields. In this model, the spin-down of central black hole powers both the GRB and GW emission. The GWs from such system are expected to be narrowband $((1 \sim 2 \text{ kHz})(1+z))$ at a redshift of z) with a strong frequency evolution [161]. The frequency is predicted to vary with time such that $df/dt = \text{const}$ [161]. The GW emission is expected to last from a few seconds to minutes with a strain of $h \sim 10^{-23}$ at 1 kHz [161].

PNS convection and other instabilities

PNS convection, in general, is turbulent and expected to occur at moderate to high Reynolds numbers leading to incoherent stochastic broadband GW transients. The typical expected GW strains are $h \sim 3 \times 10^{-23}$ at a galactic distance of 10 kpc [111, 124]. As mentioned before, the PNS, if born with large rotational speeds (10 – 100 msec), could also undergo rotational instabilities. Depending on the ratio of rotational kinetic energy (T) and gravitational energy (W), there are various rotational instabilities that could occur [125, 142, 124]. If $T/|W| \gtrsim 0.27$, nonaxisymmetric deformation will occur dynamically lasting a few dynamical times of $\mathcal{O}(\text{ms})$ (see, e.g., [23, 146]) producing GWs on that timescale. At $T/|W| \gtrsim 0.14$, a secular gravitational-radiation reaction or viscosity-driven instability may set in, leading to nonaxisymmetric deformation which could last $\sim 10 - 100$ s [106, 45] producing GWs on that time scale.

R -modes are another type of instabilities, called quasi-toroidal oscillations, that could also occur in PNS. These oscillations are unstable to growth by gravitational-radiation reaction via the secular Chandrasekhar-Friedman-Schutz instability [38, 74] and can produce GWs of very long duration. The typical expected strain amplitudes are [128],

$$h \sim 4.4 \times 10^{-24} \alpha (\Omega_{\text{NS}} / \sqrt{\pi G \bar{\rho}})^3 (20 \text{ Mpc} / D) \quad ,$$

where Ω_{NS} is the PNS angular velocity, D is the distance to the source and $\bar{\rho}$ is the mean neutron star density. The parameter $\alpha \in [0, 1]$ is the dimensionless saturation amplitude of the r -modes and most recent work [31, 30] suggests that $\alpha \ll 0.1$.

3.1.2 Postmerger evolution of compact binaries

In Section 3.1.1, we discussed a variety of scenarios for long GW transients in the context of single massive star producing PNS and/or black-hole – accretion-disk systems. A similar situation could also arise in the postmerger stage of compact binaries. Depending on the masses of binary constituents, the resultant object could be a black hole or PNS [99]. As in the case of massive stars, the resultant PNS or black-hole – accretion-disk systems in the

post-merger stage could produce GWs due to various instabilities described in Section 3.1.1.

In some cases, such as highly eccentric black hole binaries (BBH), the pre-merger stage is hard to model and hence standard matched filtering techniques used for compact binary mergers could not be used for GW detection. According to some models [121], a significant fraction of BBH form dynamically with high eccentricities ($\epsilon > 0.9$) leading to an Advanced LIGO event rate of $\sim 1 - 100 \text{ yr}^{-1}$. Hence we might need new detection algorithms to look for such GW signals, which is the topic of this chapter.

3.1.3 Isolated neutron stars

Isolated neutron stars are another potential source of long GW transients. There are two sub-categories that are most promising: pulsar glitches and soft-gamma repeater flares.

Pulsar glitches are sudden speed-ups in the rotation of pulsing neutron stars observed by radio and X-ray observatories. The fractional change in rotational frequency ranges $10^{-10} < \Delta f/f < 5 \times 10^{-6}$, corresponding to rotational energy changes of $\lesssim 10^{43} \text{ erg}$ [102, 117]. The speed-up, which takes place in $< 2 \text{ min}$, is followed by a period of relaxation (typically weeks) during which the pulsar slows to its pre-glitch frequency [114]. The mechanism by which pulsar glitches occur is not yet understood well, but if we assume that the relaxation occurs mainly due to the emission of GWs, we expect strains of $h \sim 8 \times 10^{-24}$ at 3.8 kHz [21] from such phenomena. This is six times below the Advanced LIGO noise floor and hence can be ruled out as a candidate for possible detection, unless there is a radically different glitch mechanism than the one considered in [21].

Soft-gamma repeaters (SGRs) are caused by seismic events in the crusts of magnetars and are identified via their electromagnetic signature. These seismic events would also alter the moment of inertia of the magnetars and hence could produce GWs. Recent searches by LIGO have set limits on lowest-order quadrupole ringdowns in SGR storms [13] and in single-SGR events [15]. Current models of GW from SGRs [80, 108, 150, 127, 92, 50, 93] are very preliminary, but even if we assume that only 0.1% of the 10^{46} erg of electromagnetic energy in a nearby SGR flare is converted into GWs, the SGRs could be observable via GWs in the advanced detector era.

3.2 An excess cross-power statistic

In Section 2.2 of Chapter 2 we derived a cross-correlation statistic integrating over all sky directions and frequencies which was then used for SGWB searches. Here we are interested in astrophysical sources with definite sky position and characteristic frequency evolution. Hence we want to develop a statistic similar to Section 2.2 but without integrating over sky directions and frequencies (but only want to integrate over a desired set of frequencies).

We start with the definition of metric perturbation coming from a particular direction in the sky:

$$h_{ab}(t, \vec{x}) = \sum_A \int_{-\infty}^{\infty} df e_{ab}^A(\hat{\Omega}) \tilde{h}_A(f) e^{2\pi i f(t + \hat{\Omega} \cdot \vec{x}/c)}. \quad (3.1)$$

As before A is the polarization state and $\{e_{ab}^A\}$ are the GW polarization tensors with Cartesian indices ab , (see Appendix A.1.1 for additional details).

Similar to Eq. (2.13), we define GW strain power spectrum in each polarization by

$$H_{AA'}(t; f) = 2 \langle \tilde{h}_A^*(t; f) \tilde{h}_{A'}(t; f) \rangle. \quad (3.2)$$

The factor of 2 comes from the fact that $H_{AA'}(t; f)$ is one-sided power spectrum. It is convenient to characterize the source with a single spectrum that includes contributions from both $+$ and \times polarizations. We therefore define

$$H(t; f) \equiv \text{Tr}[H_{AA'}(t; f)], \quad (3.3)$$

so as to be invariant under change of polarization bases. This definition is a generalization of the two-sided power spectrum for unpolarized sources defined in Eq. (2.13).

Here we are interested in defining an estimator $\hat{\mathcal{Y}}_{\Gamma}(\Omega)$ that can be used to search for signals that have characteristic shapes (Γ) in the frequency-time (ft)-maps: a two dimensional array of pixels in which each column is obtained by Fourier transform of segment of length T . Since our data consists of discrete time-series, the frequency column is also

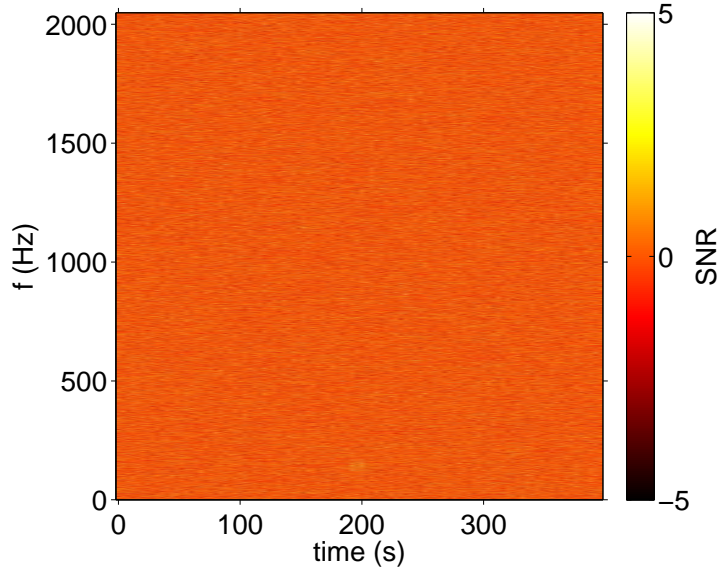


Figure 3.1: An example ft -map of $\text{SNR}(t; f, \hat{\Omega})$ using simulated data with $T = 4$ sec and $\delta F = 0.25$ Hz resolution (see (3.10)).

discrete. Figure 3.1 shows an example ft -map. In Section 3.2.3, we describe how $\hat{\mathcal{Y}}_{\Gamma}$ can be constructed by combining *clusters* of ft -map pixels, corresponding to evolution of GW signal. It is equivalent to extending the stochastic-search formalism developed in Section 2.2 beyond models of persistent unpolarized sources to include polarized and unpolarized transient sources. This is meant to bridge the gap between searches for short $\mathcal{O}(s)$ signals and stochastic searches for persistent GWs.

3.2.1 A single ft -map pixel

In Appendix A.1.2, we derive the form of an estimator \hat{Y} for GW power $H(t; f)$ in a single ft -pixel by cross-correlating the strain time series $s_I(t)$ and $s_J(t)$ from two spatially separated detectors, I and J , for a source at a sky position $\hat{\Omega}$ ¹. We find that

$$\hat{Y}(t; f, \hat{\Omega}) \equiv \text{Re} \left[\tilde{Q}_{IJ}(t; f, \hat{\Omega}) C_{IJ}(t; f) \right], \quad (3.4)$$

¹For the sake of simplicity, the calculations in this section ignore effects from windowing and the use of overlapping segments.

where $C_{IJ}(t; f)$ is the one-sided cross-power spectrum

$$C_{IJ}(t; f) \equiv 2 \tilde{s}_I^*(t; f) \tilde{s}_J(t; f). \quad (3.5)$$

This is similar to Eq. (2.29), but without the integration over $\hat{\Omega}$ and f . Here the filter function $\tilde{Q}_{IJ}(t; f, \hat{\Omega})$ depends on the source direction and polarization (as opposed to $\tilde{Q}(f)$ in Section 2.2 which is independent of $\hat{\Omega}$). For unpolarized sources (see Appendix A.1.2),

$$\tilde{Q}_{IJ}(t; f, \hat{\Omega}) = \frac{1}{\epsilon_{IJ}(t; \hat{\Omega})} e^{2\pi i f \hat{\Omega} \cdot \Delta \vec{x}_{IJ}/c}. \quad (3.6)$$

where $\epsilon_{IJ}(t; \hat{\Omega}) \in [0, 1]$, the ‘‘pair efficiency,’’ is

$$\epsilon_{IJ}(t; \hat{\Omega}) \equiv \frac{1}{2} \sum_A F_I^A(t; \hat{\Omega}) F_J^A(t; \hat{\Omega}). \quad (3.7)$$

Here $F_I^A(t; \hat{\Omega})$ is the ‘‘antenna factor’’ for detector I and $\Delta \vec{x}_{IJ} \equiv \vec{x}_I - \vec{x}_J$ is the difference in position vectors of detectors I and J ; (see Appendix A.1.1). Pair efficiency is defined such that a GW with power H will induce a strain cross-power of $\epsilon_{IJ}H$ between two detectors I, J . It is unity only in the case where both interferometers are optimally oriented so that the change in arm length is equal to the strain amplitude. For additional details see Appendix A.1.1 and Appendix A.1.2.

The variance of \hat{Y} is calculated in Appendix A.1.3. Then in Appendix A.1.4, we show that the following expression for $\hat{\sigma}_Y^2(t; f, \hat{\Omega})$ (motivated by analogy of Eq. (2.43)) is an estimator for the variance of \hat{Y} ,

$$\hat{\sigma}_Y^2(t; f, \hat{\Omega}) = \frac{1}{2} |\tilde{Q}_{IJ}(t; f, \hat{\Omega})|^2 P_I^{\text{adj}}(t; f) P_J^{\text{adj}}(t; f), \quad (3.8)$$

where P_I^{adj} is the average one-sided auto-power spectrum in neighboring pixels,

$$P_I^{\text{adj}}(t; f) \equiv 2 \overline{|\tilde{s}_I(t; f)|^2}. \quad (3.9)$$

The overline denotes an average over neighboring pixels ².

From Eqs. (3.8) and (3.4), we define the signal to noise ratio $\text{SNR}(t; f, \hat{\Omega})$ for a single ft -map pixel:

$$\begin{aligned} \text{SNR}(t; f, \hat{\Omega}) &\equiv \hat{Y}(t; f, \hat{\Omega}) / \hat{\sigma}_Y(t; f, \hat{\Omega}) \\ &= \text{Re} \left[\frac{\tilde{Q}_{IJ}(t; f, \hat{\Omega})}{|\tilde{Q}_{IJ}(t; f, \hat{\Omega})|} \frac{C_{IJ}(t; f)}{\sqrt{\frac{1}{2} P_I^{\text{adj}} P_J^{\text{adj}}}} \right] \end{aligned} \quad (3.10)$$

It depends on the phase of $\tilde{Q}_{IJ}(t; f, \hat{\Omega})$, but not on the magnitude. Thus, a single ft -pixel taken by itself contains no information about the polarization properties of the source, since the polarization does not affect the phase of \tilde{Q} . This degeneracy is broken when we combine ft -pixels from different times or from different detector pairs. In Appendix A.1.5, we derive an analytical expression for the distribution of $\text{SNR}(t; f, \hat{\Omega})$ for the cases with $\delta F = 1/T$, where δF is the frequency resolution.

3.2.2 Energy, fluence and power

One of the most interesting intrinsic properties of a transient source of GWs is the total energy emitted in gravitational radiation, E_{GW} . By measuring E_{GW} (and, when possible, comparing it to the observed electromagnetic energy, E_{EM}), we can make and test hypotheses about the total energy associated with the event as well as constrain models of GW production. Thus, it is useful to relate $\hat{Y}(t; f, \hat{\Omega})$ to E_{GW} and the related quantity of fluence. If the GW energy is emitted isotropically (in general it is not) then [145],

$$E_{\text{GW}} = 4\pi R^2 \frac{c^3}{16\pi G} \int dt \left(\dot{h}_+^2(t) + \dot{h}_\times^2(t) \right), \quad (3.11)$$

²In order to chose a suitable number of neighboring pixels to average over, one must typically take into account the stationarity of the detector noise.

where R is the distance to the source. It follows that the equivalent isotropic energy is related to our cross-power estimator as follows:

$$\hat{E}_{\text{GW}}(t; f, \hat{\Omega}) = 4\pi R^2 \frac{\pi c^3}{4G} (Tf^2) \hat{Y}(t; f, \hat{\Omega}), \quad (3.12)$$

which is same as Eq. (1.22) with $h^2(f) \simeq Y(f)$.

$\hat{E}_{\text{GW}}(t; f, \hat{\Omega})$ may contain significant uncertainty about the distance to the source or the isotropy of the GW emission. It is therefore useful to define a statistic that contains only uncertainty associated with the strain measurement. The natural solution is to construct a statistic for GW fluence, $\hat{F}_{\text{GW}}(t; f, \hat{\Omega})$, which is given by

$$\begin{aligned} \hat{F}_{\text{GW}}(t; f, \hat{\Omega}) &= \frac{\hat{E}_{\text{GW}}(t; f, \hat{\Omega})}{4\pi R^2} \\ &= Tf^2 \left(\frac{\pi c^3}{4G} \right) \hat{Y}(t; f, \hat{\Omega}). \end{aligned} \quad (3.13)$$

In the subsequent section, we show how multiple pixels can be combined to calculate the average power inside some set of pixels. The same calculation can be straightforwardly extended to calculate the total fluence. This is done by reweighting $\hat{Y}(t; f, \hat{\Omega})$ and $\hat{\sigma}(t; f, \hat{\Omega})$ by $(\pi c^3/4G)(Tf^2)$. Also Eqs. (3.15) and (3.17) must be scaled by the number of pixels in a set, N ; (otherwise we obtain average fluence instead of total fluence).

3.2.3 Multi-pixel statistic

We now generalize from our single-pixel statistic to accommodate transients persisting over N pixels in some set of pixels, Γ . We define H_Γ to be the average power inside Γ ,

$$H_\Gamma \equiv \frac{1}{N} \sum_{t; f \in \Gamma} H(t; f). \quad (3.14)$$

A minimum-variance estimator for the GW power in Γ can be straightforwardly constructed from a weighted sum of $\hat{Y}(t; f, \hat{\Omega})$ for each pixel in Γ ,

$$\hat{\mathcal{Y}}_{\Gamma}(\hat{\Omega}) = \frac{\sum_{t;f \in \Gamma} \hat{Y}(t; f, \hat{\Omega}) \hat{\sigma}_Y(t; f, \hat{\Omega})^{-2}}{\sum_{t;f \in \Gamma} \hat{\sigma}_Y(t; f, \hat{\Omega})^{-2}}. \quad (3.15)$$

Here we assume that the power is either evenly or randomly distributed inside Γ , which is to say $\langle H(t; f) \rangle = \langle H(t'; f') \rangle \equiv H_0$ and so $\langle H_{\Gamma} \rangle = H_0$. Thus,

$$\begin{aligned} \langle \hat{\mathcal{Y}}_{\Gamma}(\hat{\Omega}) \rangle &= \left\langle \frac{\sum_{t;f \in \Gamma} \hat{Y}(t; f, \hat{\Omega}) \hat{\sigma}_Y(t; f, \hat{\Omega})^{-2}}{\sum_{t;f \in \Gamma} \hat{\sigma}_Y(t; f, \hat{\Omega})^{-2}} \right\rangle \\ &= \frac{\sum_{t;f \in \Gamma} \langle \hat{Y}(t; f, \hat{\Omega}) \rangle \hat{\sigma}_Y(t; f, \hat{\Omega})^{-2}}{\sum_{t;f \in \Gamma} \hat{\sigma}_Y(t; f, \hat{\Omega})^{-2}} \\ &= H_0 \left(\frac{\sum_{t;f \in \Gamma} \hat{\sigma}_Y(t; f, \hat{\Omega})^{-2}}{\sum_{t;f \in \Gamma} \hat{\sigma}_Y(t; f, \hat{\Omega})^{-2}} \right) = \langle H_{\Gamma} \rangle. \end{aligned} \quad (3.16)$$

Here we have additionally assumed that there are no correlations between $\hat{Y}(t; f, \hat{\Omega})$ in different pixels. If the GW signal in different pixels is correlated, then the $\{\hat{Y}(t; f, \hat{\Omega})\}$ are correlated and Eq. (3.15) should, in theory, be modified to include covariances between different pixels. In practice, however, the covariance matrix is not known, and so we must settle for this approximation, which gives the estimator a higher variance than could be achieved if the covariance matrix was known.

The associated estimator for the uncertainty is

$$\hat{\sigma}_{\Gamma}(\hat{\Omega}) = \left(\sum_{t;f \in \Gamma} \hat{\sigma}_Y(t; f, \hat{\Omega})^{-2} \right)^{-1/2}. \quad (3.17)$$

The choice of the set of pixels Γ to include in the sum in Eq. (3.15) is determined by the signal model. For example, a slowly varying narrowband signal can be modeled as a line of pixels on the ft -map. We explore this and other choices for Γ in greater detail in Section 3.4.

The SNR for given a set of pixels Γ is given by

$$\text{SNR}_\Gamma(\hat{\Omega}) = \frac{\hat{\mathcal{Y}}_\Gamma(\hat{\Omega})}{\hat{\sigma}_\Gamma(\hat{\Omega})}. \quad (3.18)$$

Since SNR_Γ is the weighted sum of many independent measurements, in case of pure noise we expect, due to the central limit theorem, that the distribution of SNR_Γ will be increasingly well-approximated by a normal distribution as the volume of Γ increases and more pixels are included in the sum ³.

3.2.4 Multi-detector statistic

It is straightforward to generalize $\hat{\mathcal{Y}}_\Gamma$ for a detector network \mathcal{N} consisting of $n \geq 2$ spatially separated detectors. First, we generate $n(n-1)/2$ ft -maps for each pair of interferometers. Then we extend the sum over pixels in Eq. (3.15) to include a sum over unique detector pairs $p(I, J)$:

$$\hat{\mathcal{Y}}_\Gamma^{\mathcal{N}}(\hat{\Omega}) = \frac{\sum_{p(I,J)} \sum_{t;f \in \Gamma} \hat{Y}_{IJ}(t; f, \hat{\Omega}) \hat{\sigma}_{IJ}(t; f, \hat{\Omega})^{-2}}{\sum_{p(I,J)} \sum_{t;f \in \Gamma} \hat{\sigma}_{IJ}(t; f, \hat{\Omega})^{-2}}. \quad (3.19)$$

By construction, the expectation value is

$$\langle \hat{\mathcal{Y}}_\Gamma^{\mathcal{N}} \rangle = H_\Gamma. \quad (3.20)$$

The associated uncertainty is

$$\hat{\sigma}_{\hat{\mathcal{Y}}_\Gamma^{\mathcal{N}}}(\hat{\Omega}) = \left(\sum_{p(I,J)} \sum_{ft} \hat{\sigma}_{IJ}(t; f, \hat{\Omega})^{-2} \right)^{-1/2}. \quad (3.21)$$

Adding new detectors to the network improves the statistic by mitigating degeneracies in sky direction and polarization parameters and also by improving sensitivity to H_Γ by increasing the number of pixels contributing to $\hat{\mathcal{Y}}_\Gamma^{\mathcal{N}}$.

³Here we also assume that the probability density function for each pixel is the same, which is to say that the noise and signal are approximately stationary.

3.2.5 Relationship to the GW radiometer

The multi-pixel statistic \hat{Y}_Γ is straightforwardly related to the GW radiometer technique, which has been used to look for GWs from neutron stars in low-mass X-ray binaries [8]. By constructing a rectangular set of pixels consisting of one or more frequency bins and lasting the entire duration of a science run, we recover the radiometer statistic as a special case.

It is instructive to compare the unpolarized radiometer statistic [8] with our \hat{Y}_Γ :

$$\hat{Y}^{\text{rad}}(t; f, \hat{\Omega}) \equiv \int_{-\infty}^{\infty} df \tilde{Q}_{IJ}^{\text{rad}}(t; f, \hat{\Omega}) \tilde{s}_I^*(t; f) \tilde{s}_J(t; f) \quad (3.22)$$

$$\tilde{Q}_{IJ}^{\text{rad}}(t; f, \hat{\Omega}) \equiv \lambda_t \frac{\gamma_{IJ}(t; f, \hat{\Omega}) \bar{H}(f)}{P_I(f) P_J(f)} \quad (3.23)$$

$$\gamma_{IJ}(t; f, \hat{\Omega}) \equiv \epsilon_{IJ}(t; \hat{\Omega}) e^{2\pi i f \hat{\Omega} \cdot \Delta \vec{x}_{IJ}/c}. \quad (3.24)$$

Here $\gamma_{IJ}(t; f, \hat{\Omega})$ is the so-called overlap reduction factor, λ_t is a normalization factor and $\epsilon_{IJ}(t; \hat{\Omega})$ is the pair efficiency, which we define in Eq. (A.18) and Eq. (3.7).

There are two things worth noting here. First, the extra factor of $H(f)/P_I(f)P_J(f)$ in the expression for $\tilde{Q}_{IJ}^{\text{rad}}$ does not appear in our expression for \tilde{Q}_{IJ} (see Eq. (A.17)). The factor of $1/P_I(f)P_J(f)$ is proportional to $\sigma(f)^{-2}$, and so it is analogous to the weighting factors in Eq. (3.15). The difference is that \hat{Y}^{rad} builds this weighting into the filter function whereas we opt to carry out the weighting when combining pixels. We used similar formalism in searches for SGWB using colocated detectors (see Section 2.5.1). The factor of $\bar{H}(f)$ in $\tilde{Q}_{IJ}^{\text{rad}}$ is the expected source power spectrum. When we choose a set of pixels Γ , we effectively define $H(f)$ such that $H(f) = \text{const}$ inside Γ and $H(f) = 0$ outside Γ .

Second, we note that apparently $\tilde{Q}_{IJ}^{\text{rad}} \propto \epsilon$ whereas our filter scales like $\tilde{Q}_{IJ} \propto 1/\epsilon$. It turns out that both filters scale like $1/\epsilon$ because the radiometer normalization factor $\lambda \propto \epsilon^{-2}$. The historical reason for this is that the radiometer analysis was developed by analogy with isotropic analyses [19], which includes an integral over all sky directions. The inclusion of $\gamma(t; f, \hat{\Omega})$ in the expression for $\tilde{Q}_{IJ}^{\text{rad}}$ serves to weight different directions as more or less

important just like the factor of $1/P_I(f)P_J(f)$ weights different frequencies.

3.2.6 Relation to other search frameworks

This is not the first time that ft -maps of data have been proposed to search for GWs. The literature on this subject is extensive and diverse. We concentrate on comparison with “excess power” methods, (see e.g., [20, 152, 96]). The key difference between our framework and others is that we cross-correlate data from two interferometers *before* they are rendered as ft -maps. Previous implementations such as [152] and [96] instead form ft -maps by auto-correlating data from each interferometer individually and then correlating regions of significance in these maps. For Gaussian noise, neither of these ways of combining data from different detectors is optimal. Instead, the optimal multi-detector method incorporates both autocorrelated and cross-correlated components [20] (however if we just compare auto-power and cross-power methods, in [20] for CBC signals it is shown that cross-power analyses perform better than coherent auto-power analyses). Real interferometric GW data, however, is not Gaussian. Rather, there is an underlying Gaussian component with frequent non-Gaussian bursts called “glitches.” For situations of this type, our approach has two advantages.

First, noise bursts in both detectors that coincide in time and frequency increase the false-alarm rate for statistics with auto-correlated components, but are suppressed in our cross-correlation analysis unless the waveforms of the burst themselves are correlated in phase like a true GW. Second, even when noise bursts are present, the pixel values in an ft -map of cross-correlated data are well approximated by a simple model. This is unlike ft -maps with auto-correlated components, for which there is a no simple description. Thus, while our statistic is sub-optimal for Gaussian data, we expect it to perform well for real interferometer data. Moreover, even in the case of Gaussian noise, we do not sacrifice much sensitivity compared to the optimal excess-power statistic, or even to matched filtering, as demonstrated in [159].

3.3 Distribution of signal and background

In order to determine if a candidate event warrants further examination, it is necessary to determine the threshold above which an event is elevated to a GW candidate. This threshold is usually phrased in terms of a false-alarm rate (FAR). In Section 3.2, we argued that ft -maps of cross-power provide a convenient starting point for searches for long transients because cross-correlation yields a reasonably well-behaved $\text{SNR}(t; f, \hat{\Omega})$ statistic whose probability density function (PDF) we can model semi-analytically or numerically, thus allowing straightforward calculation of a nominal detection threshold in the presence of Gaussian noise. We now assess this claim quantitatively.

There are two limits in which we can semi-analytically derive the expected distribution of pixel $\text{SNR}(t; f, \hat{\Omega})$, assuming Gaussian noise for initial time-series. First limit is when the frequency resolution of ft -map is inversely proportional to the length of each segment i.e., $\delta F = \frac{1}{T}$. In this case the distribution can be derived easily (see Appendix A.1.5 for the derivation) and Figure 3.2 shows the distribution of $4\text{ s} \times 0.25\text{ Hz}$ size pixels. The other limit is when we average over a large number of frequency bins i.e., $\delta F \gg \frac{1}{T}$. Since we are averaging over a large number of frequency bins, according to central limit theorem the distribution will converge to a Gaussian distribution. Figure 3.3 shows distribution of $\text{SNR}(t; f, \hat{\Omega})$ for $52\text{ s} \times 0.25\text{ Hz}$ size pixels.

3.4 Pattern recognition

In this section we apply the cross-power statistic developed in Section 3.2 for a set of rectangular manifolds (called ‘boxes’) in a given ft -map in order to search for broadband astrophysical GW signals (PNS convection type signals). In Section 3.5, we introduce another type of algorithm, called burst cluster, to look for narrowband signals.

3.4.1 Broadband box search

We demonstrate how a box-shaped set of pixels can be used to search for a broadband GW transient source. For illustrative purposes, we consider a simple model based on protoneutron

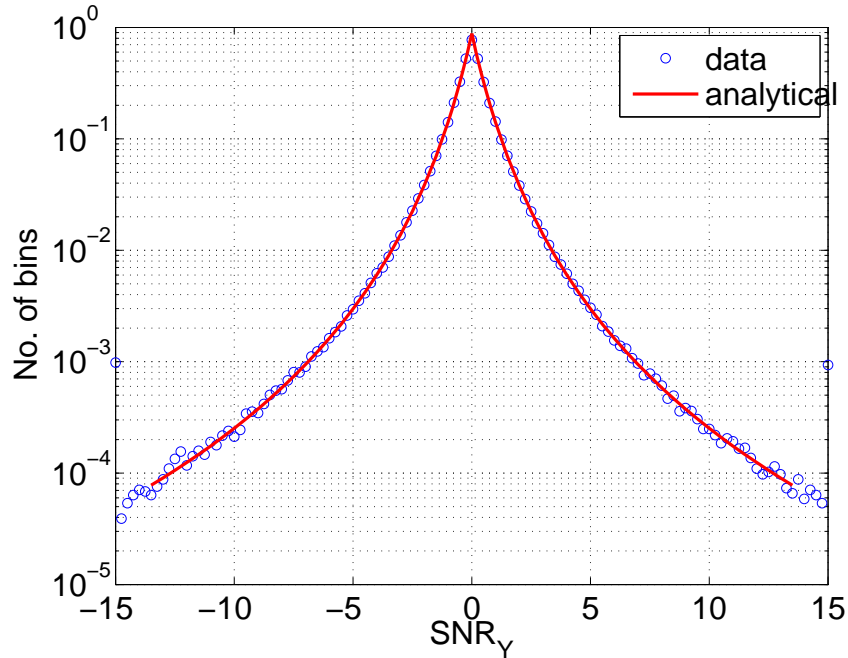


Figure 3.2: Distribution of $\text{SNR}(t; f, \hat{\Omega})$ for the case of $4\text{ s} \times 0.25\text{ Hz}$ size pixels with Monte Carlo data. For this plot we used 2 neighboring segments to calculate $\hat{\sigma}_Y(t; f, \hat{\Omega})$.

star (PNS) convection with a spectrum produced in an axisymmetric PNS model assuming a non-rotating, $15 M_{\odot}$ progenitor [124] (see Figure 3.4). We simulate a $d = 4.5\text{ kpc}$ source in the direction of $\text{ra} = 17\text{ hrs}$, $\text{decl} = 30^{\circ}$ at 00:00 GMST on top of simulated detector noise comparable to the design sensitivity for initial LIGO. We calculate the cross-power statistic $\hat{\mathcal{Y}}_{\Gamma}$ utilizing a $200\text{ Hz} \times 16\text{ s}$ box constructed with the H1L1 detector network. We use $4\text{ s} \times 0.25\text{ Hz}$ pixels, and for each pixel we use 20 adjacent segments to calculate $\hat{\sigma}(t; f, \hat{\Omega})$, (10 on each side). We tile the ft -map and record the $\hat{\mathcal{Y}}_{\Gamma}$ within each box. We find that the signal can be recovered with $\text{SNR}(t; f, \hat{\Omega}) = 8$. The results are summarized in Figure 3.5.

3.4.2 Other algorithms

In Section 3.4.1 we have, for illustrative purposes, presented one of the many pattern recognition algorithms that may be applied to the problem of looking for features in ft -maps of cross-power. There is a diverse and extensive literature devoted to the study of cluster identification, (see, e.g., [91, 97]). There are typically both advantages and disadvantages

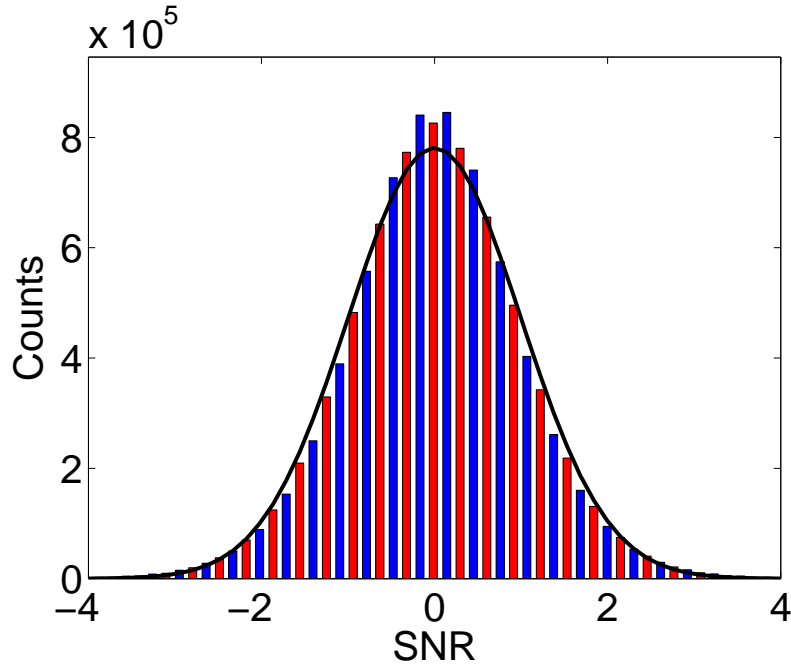


Figure 3.3: Histogram of $\text{SNR}(t; f, \hat{\Omega})$ using $52 \text{ s} \times 0.25 \text{ Hz}$ pixels comparing S5 data with an unphysical time-shift (blue) to Monte Carlo data (red) and a normal distribution with mean = 0 and $\sigma = 1$ (black). Here we used 2 neighboring segments to calculate $\hat{\sigma}_Y(t; f, \hat{\Omega})$. Figure taken from [159].

associated with each algorithm, which means that each one lends itself to different applications.

There are other algorithms that are currently being used for GW signal identification in LIGO data such as Radon algorithm [76], locust and Hough algorithms [133], burst cluster [97], burstegard [131] etc. The Radon algorithm uses Radon transform [51] to convert line-like structures in a 2D map into points in Radon space. A bright point in Radon space corresponds to a strong line in the original 2D ft-map. An example plot can be seen in reference [159]. The Hough algorithm is similar to the Radon algorithm, except that it can be extended to fit tracks described by arbitrarily high-order polynomials. By introducing additional fit parameters, the tracks tend to be reconstructed more accurately. However, by adding more parameters, the significance of a line-like event with little or no curvature can be less than the value obtained by the Radon algorithm.

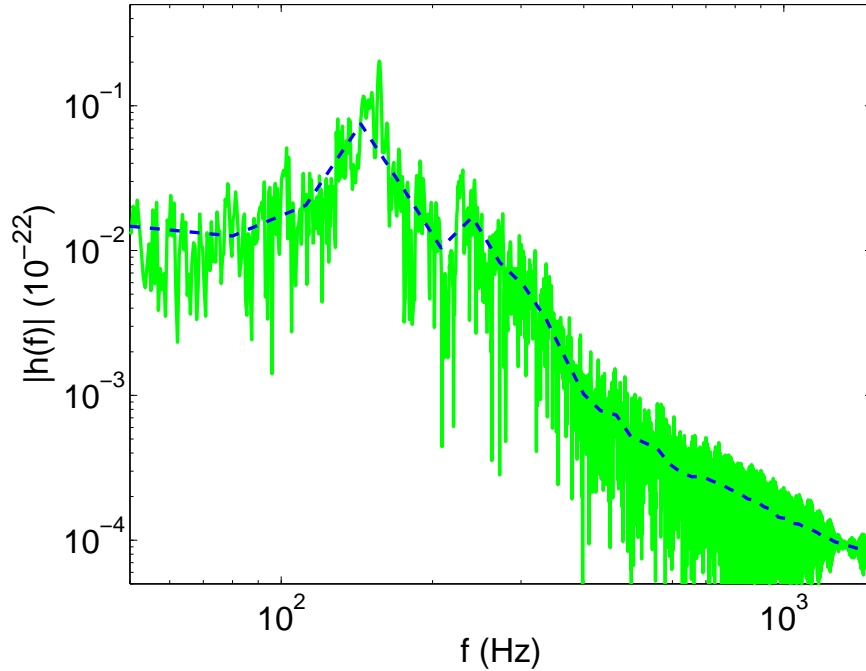


Figure 3.4: GW strain amplitude spectrum due to PNS convection in an axisymmetric PNS model at a typical galactic distance of 10 kpc [124]. This plot was generated using the data simulated in [124] available at [123]. Figure published in [159].

The locust algorithm is a local wandering algorithm, which integrates the ft -map along a chain of local maxima. This algorithm has the advantage that it can reconstruct arbitrary-shaped tracks without large numbers of free parameters. Since it relies on local maxima, however, the Radon and Hough algorithms are more robust if the GW power is spread diffusely over many pixels.

Burst cluster is a density based clustering algorithm that connects different regions of ft -map based on the number of pixels exceeding a threshold. It can be used to search for both narrowband and broadband signals. Burstegard is a derivative of burst cluster and uses ‘closeness’ of pixels exceeding a threshold to cluster them. Similar to burst cluster, burstegard can also be used to search for narrowband and broadband signals. Compared to burst cluster, burstegard is better in identifying very narrow, single pixel, tracks in ft -maps while burst cluster is better at identifying weak broadband signals.

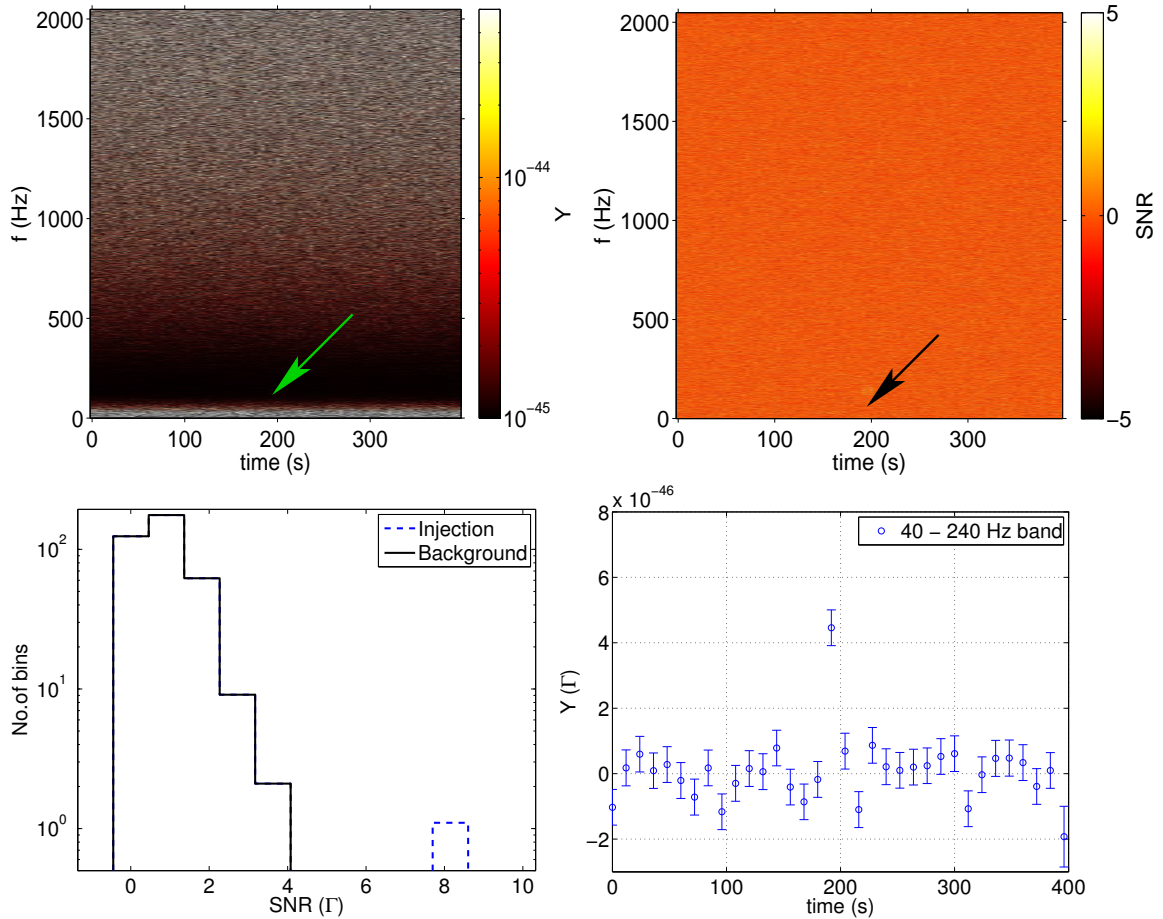


Figure 3.5: PNS signal injection and recovery using with the box-search algorithm. Top-left: an ft -map of $\hat{Y}(t; f, \hat{\Omega})$. The injected signal (not visible by eye) is indicated with a green arrow. Top-right: an ft -map of $\text{SNR}(t; f, \hat{\Omega})$. The injected signal (not visible by eye) is indicated with a black arrow. Bottom-left: a histogram of SNR_Γ for a $200 \text{ Hz} \times 12 \text{ s}$ box. The blue dashed line corresponds to the injection. Though the signal is weak in each pixel, the signal obtained by combining every pixel in Γ is large. Bottom-right: \hat{Y}_Γ as a function of time. Figure published in [159].

3.4.3 Application to environmental noise identification

While our discussion until now has been focused on the detection of GW transients, the same formalism can be applied to look for structure in ft -maps of cross-power between any two data channels. In particular, it is illuminating to study the cross-power between an interferometer’s GW-strain channel, (which we denote s_{GW}) and a physical environmental monitoring (PEM) channel such as a seismometer or a magnetometer channel located near the interferometer. Since PEM channels are not sensitive to GWs, statistically significant features in an ft -map of PEM- s_{GW} cross-power are likely due to environmentally-induced noise artifacts.

Transient artifacts are called “glitches” whereas persistent narrowband features are often called “lines” or “wandering lines” when the frequency slowly changes over time. Glitches and wandering lines can be problematic for searches for bursts / compact binary coalescences and for pulsars respectively, see, e.g., [149, 11, 10]. (They also produce non-Gaussian noise for our cross-power statistic.) It is thus desirable to identify and when possible mitigate these noise features.

For illustrative purposes, we considered a special class of noise artifacts induced by passing airplanes. These “airplane events,” are relatively well understood. The existing LIGO airplane veto system (called `planemon`) has been shown to flag airplanes observed in microphone channels, and these flags have been shown to agree with airplane flight data [81], though the existing `planemon` algorithm does not determine if the passing airplane affects $s_{\text{GW}}(t)$. Since we already understand a lot about airplane events, it is straightforward to assess if our algorithms are consistent with what we already know.

Since these airplane artifacts look more like straight lines, we used Radon transform to identify these events in ft -maps created by correlating GW channel and acoustic channels (these PEM channels are sensitive to the sound produced by the passing by airplanes). By using a large set of ft -maps (~ 600), we found that Radon transform was able to recover most of the airplane like events and in some cases even performed better than `planemon`. Figure 3.6 shows an example ft -map with an airplane event and its identification using Radon algorithm. With this study we were able to show the usefulness of current pipeline

not only in searching for GW transients, but also in identifying noise transients in detector data.

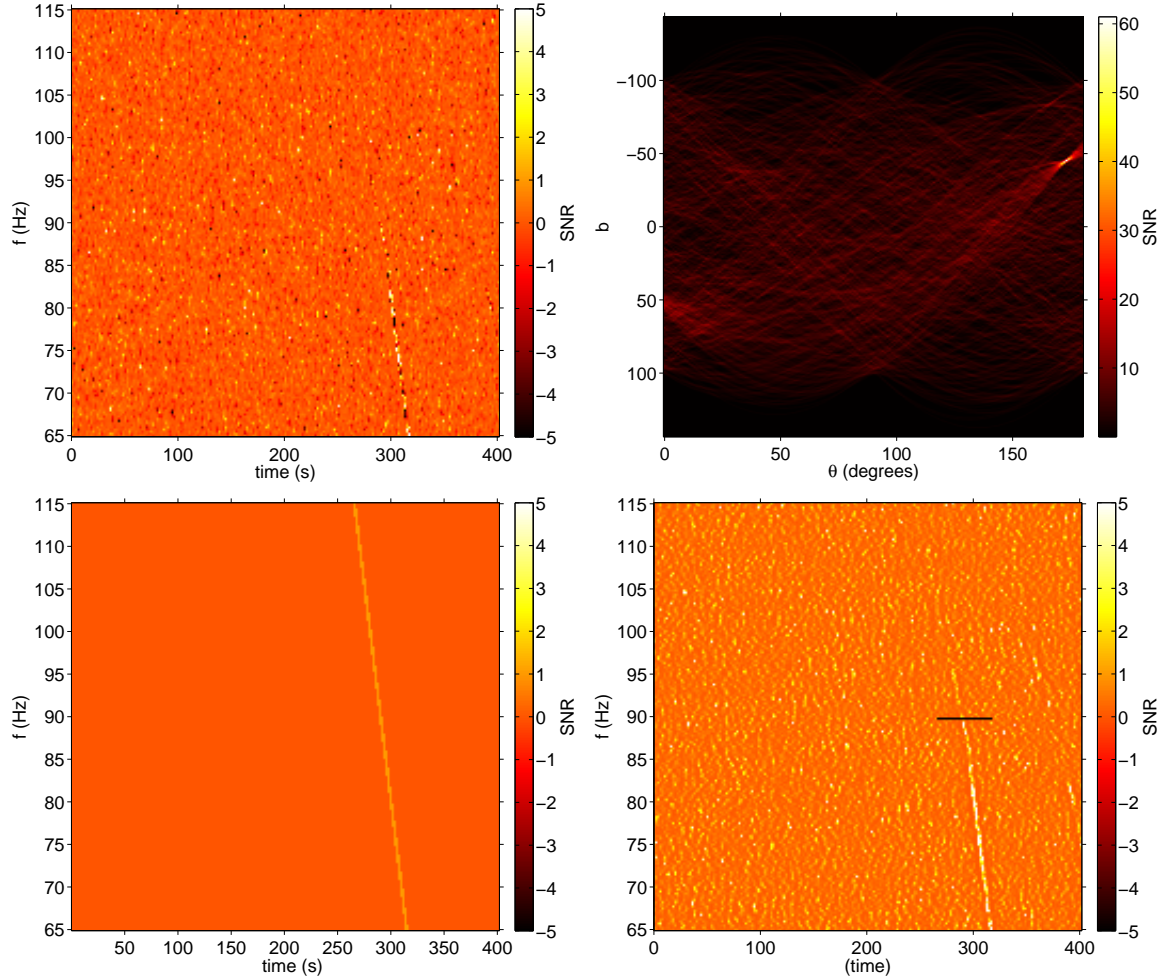


Figure 3.6: Top-left: a 400s-duration map of $\text{SNR}(t; f)$ (see Eq. (3.10)) created with $4\text{ s} \times 0.25\text{ Hz}$ pixels and using s_{GW} cross-correlated with a microphone. The slightly curved track on the right side of the plot is caused by the Doppler-shifted acoustic signal from a passing airplane. Top-right: the associated Radon map. Note the bright spot on the mid-right corresponding to the airplane track. Bottom-left: ft -map of the reconstructed track using the maximum $\text{SNR}(t; f)$ pixel in Radon space. Bottom-right: ft -map of the magnitude of $\text{SNR}(t; f)$ including a black line corresponding to the veto window. These data are from the beginning of LIGO’s S5 science run. . Figure taken from [159].

3.5 Searches for long GW transients from GRBs

In the previous section we derived a detection statistic and developed an analysis pipeline to look for long GW transients by cross-correlating data from two or more detectors. In this section we describe a method that could be used to look for long GW transients from Gamma-ray bursts.

3.5.1 Gamma-ray bursts

Gamma-ray bursts are intense flashes of high energy electromagnetic radiation from distant astrophysical sources. They are considered as the brightest of electromagnetic events known to occur in our observable universe. GRBs are most commonly detected at distances corresponding to $z \approx 1 - 2$ [79], though, nearby GRBs have been detected as close as 37 Mpc [77]. The GRBs are generally divided into two classes [101, 78] depending on their (t_{90}) duration: short gamma-ray bursts and long gamma-ray bursts. Short gamma-ray bursts, lasting upto ~ 2 secs and characterized by hard gamma-ray spectra (higher end of gamma-ray spectrum), are expected to arise from the merger of compact binaries while long gamma-ray bursts, lasting more than ~ 2 secs and characterized by soft gamma-ray spectra, are expected to be produced by the collapsars (collapse of massive stars). In Section 3.1, we described these two scenarios, protoneutron star and collapsar, as plausible sources of GWs. In this section we mainly focus on the detection of GWs from such sources using electromagnetic observations as triggers.

3.5.2 Methodology and preliminary results

Here we are interested in the detection of GWs from GRBs using electromagnetic observations as triggers, particularly in the detection of narrowband long duration (~ 100 secs) GW signals. The motivation behind the search for such narrowband signals is that some models predict GWs with considerably higher strain ($\sim 10^{23}$) upto source distances of ~ 100 Mpc [161, 130] which are potentially observable with initial and advanced LIGO. Other models of broadband GW transients, such as PNS convection, predict either smaller

strain or require closer sources. We note here that there were previous LIGO GRB analyses [16, 3, 4, 9, 156] that searched for GWs in coincident with GRBs, but they mainly focused on sub-second burst signals. Here, however, we are interested in signals that last upto ~ 100 seconds.

First we produce ft-maps centered around GRB triggers using data from H1 and L1 LIGO detectors obtained during their fifth science run. The GRB triggers consisting of GPS start time, right ascension (RA), and declination (dec) are obtained from the *swift* satellite [119]. We then search for largest cluster in SNR ft-maps for every GRB trigger, using clustering algorithms described in Section 3.4.2. We compare the SNRs of the largest clusters found in ft-maps around each GRB trigger with SNRs obtained from similar clustering done on ft-maps obtained by time-shifting one of the detector's data. This process of time-shifting detector data is expected to decohere the GW signal between the two detectors producing ft-maps that consist of only noise. If the SNR of the largest cluster found in the ft-map around a GRB trigger is significantly greater than any of the SNRs observed from various time-shifted ft-maps then it will be considered as significant (and detection with further validation). In case of non-detection, we set upper limits using accretion disk instability (ADI) waveforms [138] produced based on [161, 163]. These waveforms are also used to test and optimize the parameters of clustering algorithms.

Figure 3.7 shows the recovery of an ADI injection using burst cluster algorithm with ft-maps of 40 sec duration, and 150 Hz band (100 - 250 Hz). The ADI signal used here corresponds to GW signals from a system consisting of an accretion disk fragmented into a pair of blobs of mass $m_b = 0.15M_\odot$ and a central black hole with mass $m_{BH} = 10M_\odot$ and dimensionless spin parameter $a^* = 0.95$ ($a^* = 1$ corresponds to maximally spinning black hole).

Figure 3.8 shows the distribution of largest cluster SNRs (on left) for simulated as well as time-shifted data and sensitivity curve (on right) for the ADI model described above using burst cluster algorithm with an optimal set of search parameters. The sensitivity curve was produced by injecting ADI signal with different strength (corresponding to varying source distance) in a time-shifted H1-L1 detector data and recording the SNRs of largest clusters.

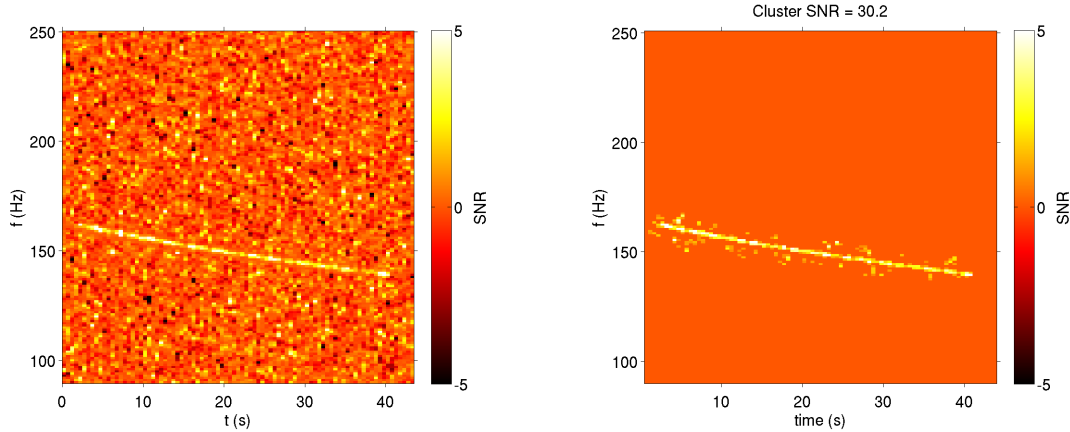


Figure 3.7: Injection and recovery of ADI signals using burst cluster algorithm. The plot on the left shows an ADI injection in timeshifted H1-L1 data and the plot on the right shows the recovery of largest cluster using burst cluster algorithm.

This was repeated 50 times and we used median of those SNRs to account for performance fluctuations in burst cluster algorithm. From the sensitivity curve plot, we can approximate that the distance upper limit (90%) for this particular ADI model in an optimal direction (used for making this plot) would be ~ 30 Mpc, which is the point at which the recovered cluster SNRs start to fluctuate (width of the blue line starts to increase). This is because, in the case of strong signal, the recovered cluster SNRs will be dominated by the ‘signal’ pixels, whereas in the case of weak signals (or distant sources) the ‘noise’ pixels that satisfy clustering parameter will also start to contribute. The above upper limit could also be estimated from comparing background distribution plot with the sensitivity plot. If do not detect a significant cluster in the direction of a GRB, then the SNR of largest cluster in that direction could be as large as ~ 30 (from the background distribution plot) and that corresponds to a source distance upper limit of ~ 33 Mpc. Any source closer than that would produce a cluster SNR larger than the largest background cluster SNR and hence can be identified as a significant cluster. With the same clustering parameters, we looked at the ft-map around the GRB 060110 and found the largest cluster SNR to be 12.9. This corresponded to a P-value of 0.3 (not a significant cluster) and 90% distance upper limit of 46 Mpc.

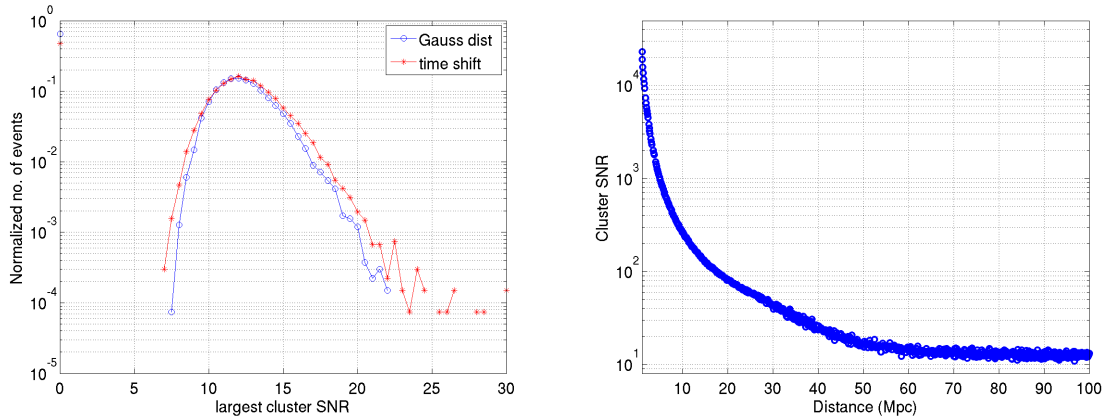


Figure 3.8: Left panel: Distribution of largest cluster SNRs using both simulated and time-shifted H1-L1 data. Right panel: Recovered largest cluster (median) SNR as a function of distance to an ADI signal (injected in timeshifted H1-L1 data).

In reference [43], a similar analysis was carried out, but with 1500 sec maps around 50 GRB triggers and using 1100 Hz frequency band (100 - 1200 Hz). The analysis also used a different clustering algorithm (burstegard). The analysis did not find any significant cluster and set 90% distance upper limits of $\sim 3 - 33$ Mpc, depending on the GRB trigger and ADI model used.

3.6 Summary

In this chapter, we reviewed a few scenarios of long-GW transients including proton-neutron star convection, accretion disk fragmentation, rotational instabilities in neutron stars, r -modes, pulsar glitches and soft gamma repeater flares. Many of the models we considered predict strain amplitudes detectable in the advanced-detector era.

Next, inspired by stochastic analyses, we introduced a new framework, which can be used to look for GW transients on timescales of seconds to weeks. This framework, which is a generalization of the GW radiometer [8], utilizes ft -maps of GW-strain cross-power using two or more spatially separated interferometers in order to look for statistically significant clustering. A comparison of simulated detector noise with time-shifted data revealed that ft -cross-power-maps made with real interferometer data are well-behaved suggesting that

the threshold for candidate events can be determined analytically.

We illustrated how different pattern-recognition techniques can be used to identify GW signatures in ft -maps. We also pointed out that some of these techniques using ft -maps generated using a GW-strain channel cross-correlated with a LIGO PEM channel can be used to identify environmental noise transients in GW interferometers.

We used the new pipeline to search for long GW transients from GRBs and found no significant signals. For models with energy emission of $E_{\text{GW}} = 0.1M_{\odot}$ and in LIGO's sensitive frequency band 100 – 200 Hz, we were able set distance upper limits as large as $D \approx 30$ Mpc [43].

Chapter 4

Seismic waves and gravitational wave detectors

Seismic waves are elastic waves that propagate along Earth's surface or in its interior. They are produced by natural processes such as volcanoes, earthquakes, wind etc., and anthropogenic processes such as mining work, vehicular movement, explosions etc. Seismic waves couple to GW detectors via mechanical couplings through support structures of detectors as well as via direct Newtonian interactions (see in Section 4.1). They are one of the dominant noise sources at low frequencies (< 10 Hz) along with thermal noise and quantum noise (see Section 1.3.1 and Figure 4.3). Current generation of ground based GW detectors are already reaching down to 10 Hz, while next generation of detectors are expected (or desired) to have better sensitivities close to 1 Hz.

There are various reasons for trying to achieve better sensitivities at low frequencies: (i) the rotational frequencies of majority of observed pulsars are around 1 Hz [22]; (ii) sensitivity to SGWB with $\alpha = 0$ (corresponding to most cosmological models) increases with decrease in detector frequency (see Eq. (2.16)); and (iii) CBC signals could be observed over longer periods. With the developments in squeezed light techniques, now the quantum noise can be pushed down [1] while the improved quality of suspension wire material and cryogenic setup can be used to reduce suspension and other sources of thermal noise. Thus we are left with seismic and Newtonian noise. Seismic noise can also be reduced to some extent with new active and passive isolation systems, but currently there are no ways to shield GW detectors from Newtonian noise. A careful study of seismic fields around the detectors is

necessary to develop and implement Newtonian noise subtraction schemes [63, 94].

In Section 4.1, we discuss properties and classification of seismic waves and a simple description of Newtonian noise. Then in Section 4.2 we describe a 3D array of seismometers set up at Homestake Mine, South Dakota to study seismic wave propagation deep underground and present initial results obtained from analyzing the array data. In Section 4.3 we introduce some of the existing seismic wave analysis algorithms and also a new algorithm based on GW data analysis methods. We also provide some recent simulation results. Concluding remarks and summary are given in Section 4.5.

4.1 Seismic waves and Newtonian noise

Seismic waves span a wide range of frequencies and amplitudes. The lowest observable frequency is that of the free oscillations of the Earth (~ 54 mins) induced by large earthquakes while the highest frequency is ~ 20 Hz, which is a limit imposed by the attenuation of seismic waves in rocks. The amplitudes of seismic waves (maximum displacement of the ground) ranges from 10^{-10} to 10^{-1} meter. Seismic waves are classified into two broad categories: body waves and surface waves. Body waves are elastic waves that propagate in the interior of the Earth while surface waves, as the name suggest, are waves that propagate along the Earth's surface.

Body waves

Body waves are further classified into two: longitudinal and transverse waves. Similar to sound waves, longitudinal waves produce a series of compression and rarefaction along their direction of travel i.e, particle motion is along the direction of the wave. In seismology, they are also called P-waves (primary waves), because they represent the first set of waves that arrive from a distant earthquake. Transverse waves, also called shear or rotational waves, produce shear and rotation in the material they pass through (but no volume change). In this case the particle motion is perpendicular to the direction in which the wave is traveling. In seismology, they are also called S-waves (secondary waves), because they are the second

set of waves to be recorded from an earthquake.

The velocities of longitudinal waves, v_l , and of transverse waves, v_t , in a homogeneous and isotropic medium are given by the formulae

$$v_l = \sqrt{\frac{\lambda + 2\mu}{\rho}} \quad \text{and} \quad v_t = \sqrt{\frac{\mu}{\rho}}, \quad (4.1)$$

where λ and μ are the Lamé coefficients, and ρ is the density of the medium. For many elastic materials $\lambda = \mu$ and hence $v_l = \sqrt{3}v_t$ (thus P-waves travel faster than S-waves). This relation is widely used in seismology to triangulate the location of earthquakes. Typical speeds of body waves are 2-8 km/s. Similar to other elastic waves, body waves at a boundary, separating two layers of materials, are reflected, transmitted and are also changed from one type of wave to another.

Surface waves

Surface waves are the strongest waves from an earthquake and are responsible for most of the devastation. These waves are further classified into two types : Rayleigh waves (R-wave) and Love waves (L-wave). Rayleigh waves are elliptically polarized in the plane determined by the normal to the surface and the direction of propagation. Near the surface, for Rayleigh waves, the particle motion is a retrograde vertical ellipse (anticlockwise for a wave traveling to the right). Love waves are transverse waves with particle motion parallel to the surface (and perpendicular to the direction of travel). In the simplest case of isotropic half-space (at Earth-air interface with isotropic medium), the velocity of Rayleigh waves is slightly less than the transverse wave velocity, $v_R \approx 0.85v_t$ and is independent of frequency [134].

Surface waves, in general, are not new types of waves, but only interference phenomena of body waves. Therefore, in principle, we could construct the surface waves by summing body waves. However, this approach would be inconvenient if a large number of waves is to be taken into account (many additional waves are produced by the reflection and refraction at boundaries of different layers). Therefore, they are mostly dealt with as separate waves. Figure 4.1 shows an example of S, P and surface waves from a distance earthquake recorded

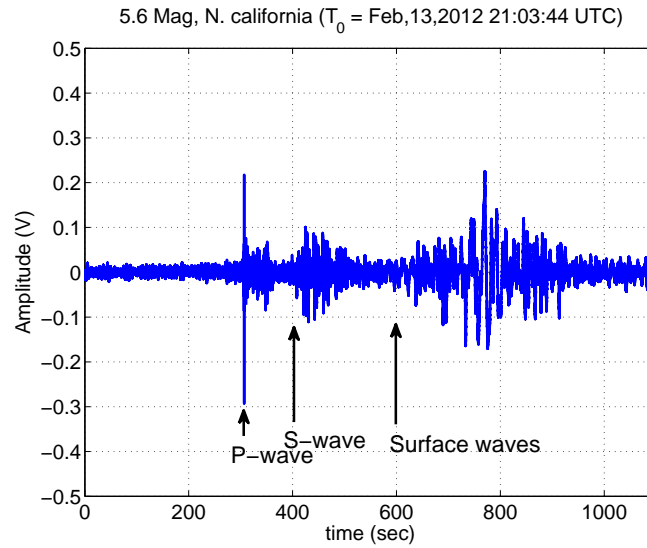


Figure 4.1: An earthquake data showing the arrival of P, S and surface waves. The above plot was made using data from the 2000ft-A station. This event corresponds to a 5.6 earthquake occurred in N. California on February 13, 2012 at a depth of 33 km.

by one of the seismometers set up at Homestake mine.

4.1.1 Newtonian noise

The surface variations produced by the seismic waves gravitationally couple to the suspended mirrors of interferometric GW detectors. Since the presence of a GW signal is measured by the movement of the mirrors along the interferometric arms, this coupling induces an unwanted error in the measurement and is called Newtonian noise. Figure 4.2 is a pictorial depiction of Newtonian noise. A similar coupling would also occur due to movements of other terrestrial masses such clouds, vehicles etc. Since this is a direct gravitational coupling, there are no known ways to screen the mirrors from such coupling. One possible solution is to reduce/control such density variations by building underground GW detectors (Newtonian noise due to seismic waves is dominant at the surface due to surface seismic waves). The other possible solution is to characterize the seismic wave fields and use it to subtract out the Newtonian noise effects. For the later, it is useful to study and characterize different seismic wave-fields which is the main topic of this chapter. Figure 4.3 shows the expected

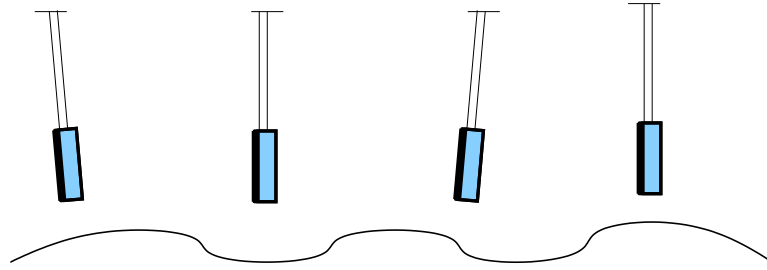


Figure 4.2: The above figure is a pictorial depiction of Newtonian noise. At low frequencies, the variations in the heights of Earth’s surface produces a considerable gravitational pull on the suspended mirrors of GW detectors mimicking the effect of GWs.

strain sensitivity curve advanced LIGO detectors. From the plot, we see that once we push down the quantum and thermal noise, Newtonian and seismic noise become the limiting noise at ~ 1 Hz.

4.2 Homestake seismic array

To study seismic wave fields and the possibility of reducing Newtonian noise in the next generation of GW detectors we have set up an array of broad-band seismometers in Homestake mine, a former gold mine in South Dakota [36]. This setup provides an opportunity to study the properties of seismic fields underground and understand the possible advantages of building underground GW detectors. The Homestake array initially included nine environmentally shielded and isolated seismic stations, three of which have been disassembled due to poor operating conditions. The remaining include one at 300 ft, one at 800 ft, two at 2000 ft and two at 4100 ft depth. Each station operated either a Trillium T240 or a Streckeisen STS-2 high-sensitivity broadband seismometer (one station operated relatively low-sensitive Guralp) [59]. During the initial setup all the stations were found to be in a plane configuration (see Figure 4.4), while in the current set up a new station at 4100-ft level was constructed to be away from the plane of the other stations and provide a 3D configuration.

Various measures were taken to optimize the response of seismometers to seismic waves. The seismometers were placed on granite tiles that were installed either on existing con-

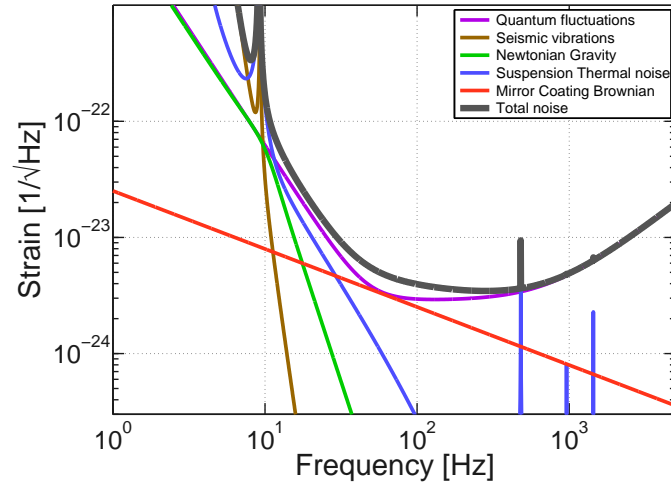


Figure 4.3: Expected strain sensitivity for advanced LIGO GW detectors. This plot was produced by Gravitational Wave Interferometer Noise Calculator (GWINC) using advanced LIGO configuration [87].

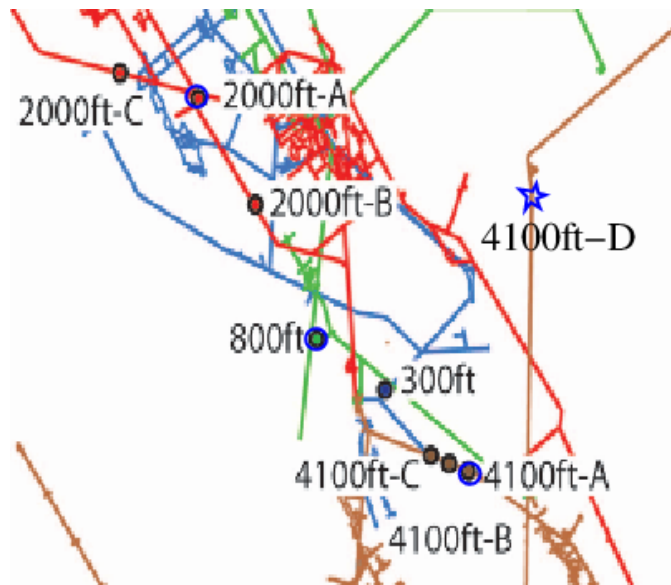


Figure 4.4: The above figure is a cross-sectional (top) view of the mine showing the locations of the seismic stations. The blue circles and blue star correspond to currently operating stations. The station at 4100-ft level marked by a star is the new station built to be away from the plane of the other stations. The map is aligned with cardinal directions (top is North).



Figure 4.5: Above photo, taken during the construction of 4100ft-D station, shows the two hut setup used for isolating seismometers and data acquisition systems.

Station	Seismometer	Position (E,N) [m]
300 ft	CMG-40T	(71,21)
800 ft	T240	(-88,124)
2000 ft A	T240	(-378,598)
2000 ft B	T240	(-234,380)
4100 ft A	STS-2	(347,-155)
4100 ft D	T-240	(187,-104)

Table 4.1: A table providing the location and type of seismometer used at each station. The location coordinates are measured with respect to the (Yates) mine-shaft elevator.

crete platforms or on new concrete platforms solidly connected to the underlying bed-rock. A multi-layer isolation made up of rigid thermal and acoustic insulation panels was built around each seismometer to further stabilize the thermal environment and to achieve suppression of acoustical signals and air currents. The data acquisition systems were setup in a separate chamber at least five feet away from the seismometer chambers to avoid electric and magnetic couplings (see Figure 4.5). Table 4.1 lists the locations (relative to surface, Yates office building) and types of seismometers used at each station. Seismometer positions were determined from mine maps and are expect to have errors $\lesssim 2$ m.

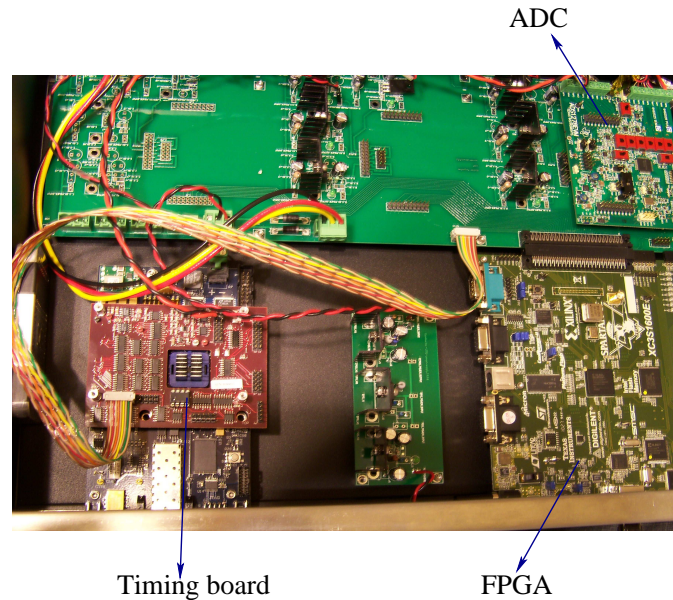


Figure 4.6: Internal view of the data read-out system. The boards that are not labeled are used for providing DC power.

Data read-out system

At each station, to read out data we are using a 24-bit data acquisition system (DAQ) designed by Vladimir Dergachev, at Caltech. It uses a 24-bit ADC (ADS1278, ± 2 V range, Texas instruments) and a FPGA (Spartan 1600, Digilent) to collect data samples from the seismometer (after amplified by an external amplifier) and pass it on to a computer via 100 Mbit ethernet cable. It uses an eight input ADC that can be triggered by the internal clock of the FPGA or with an external clock. For our setup we used an external trigger from a high precision timing board designed for advanced LIGO systems. Figure 4.6 shows an inside view of the DAQ system.

This is a low cost system, compared to standard data acquisition systems used in seismology, but with better precision and sampling rate. One issue with this system was that sometimes the board freezes (and no longer acquires data) and needs to be restarted (no plausible reason identified). At each station, we have installed a network power switch (remotely accessible) that can be used to restart different parts of the setup including the above data acquisition system to eliminate down-time.

User interface and data storage

The data from each seismometer is read out locally by the DAQ acquisition box. The data is then downsampled from 32 KHz to 512 by a small linux box, called Dreamplug, installed at each seismic station and then sent to a linux workstation at the surface via optical fibers. The surface machine collects data from all the working stations and combines them into a single file, producing 128 sec long data files in the LIGO data (frame) format. These LIGO data (frame) format files are used for further analyses.

Synchronization of data

One of the main problems in combining data from different stations is the uncertainty in the absolute and relative timing of individual stations. In the initial setup [59], we used Network Time Protocol (NTP) to synchronize different stations using an external time source providing an accuracy of \sim msec. In the new setup we use Precision Time Protocol daemon (PTPD) with an internal (to the LAN network) time source to get \sim 0.1 msec accuracy (timings are very important for determining wave velocities as well as for source localization). To further improve the timing accuracy we linear fit times of a large number of 128 sec data files. Figure 4.7 shows an example timing plot for the 4100ft-D station.

Figure 4.8 shows a complete data acquisition setup at one of the 4100-ft level stations.

4.2.1 Initial results

Our initial results show that the average seismic-noise spectra approach the global low-noise model [129] over a considerable fraction of the observation time. Apart from the local short seismic events, seismic spectral densities slowly vary over the course of weeks. Even the short event rates at Homestake mine are small compared to other sites and majority of them occurs during the daytime working hours. The secondary microseismic peak (one of the strong low frequency peaks at 0.3 Hz) is found to be correlated with the buoy data from the northern Pacific coast, with the exact buoy location varying over time [59]. This is the first time such correlation analysis was done. Figure 4.9 shows the suppression of

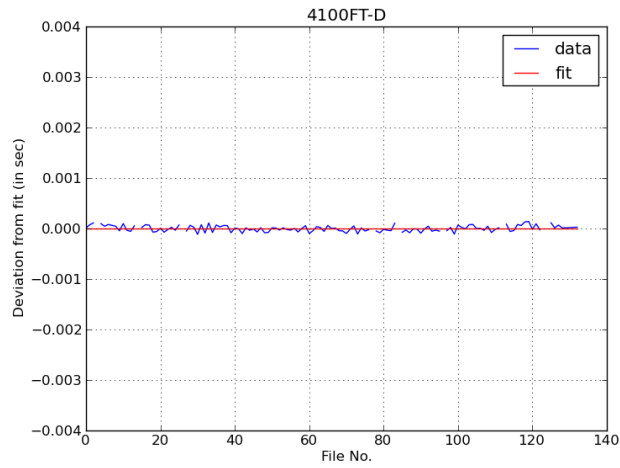


Figure 4.7: Timing plot of ~ 100 data files from 4100D-ft station. The blue curve is the time assigned to each of those files (adjusted for expected increase) by the Dreamplug and red curve is the linear fit. We see that the variation of the blue curve is of the order of 0.1 msec.

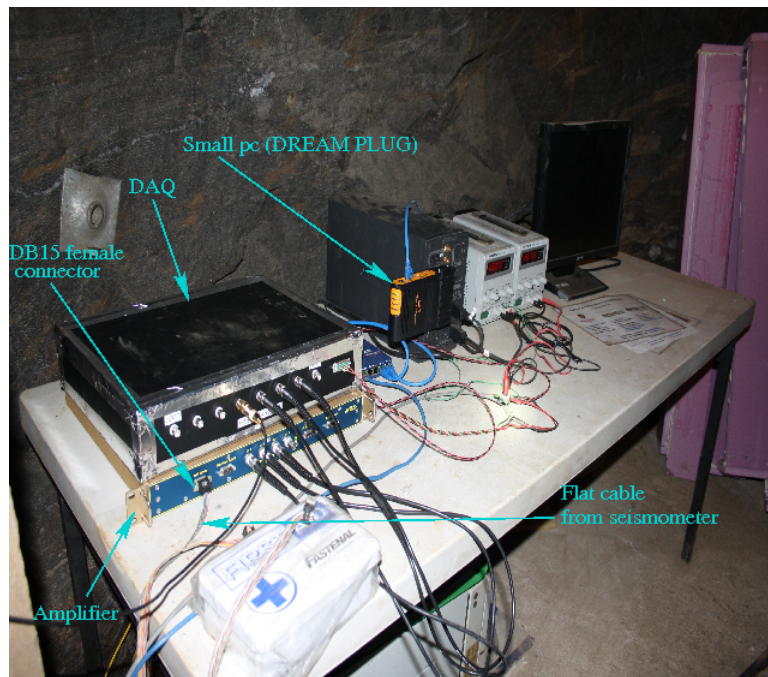


Figure 4.8: A photo of the 4100ft-A station showing the complete data acquisition setup. It is the only station where the data acquisition is set up in a natural cave like chamber. The seismometer is behind the the wall shown here.

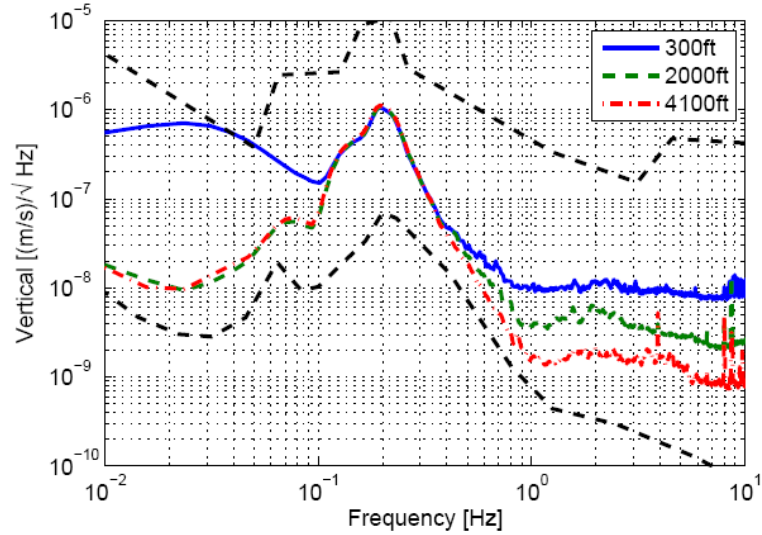


Figure 4.9: Seismic spectrum showing the reduction in high frequency noise (1 – 10 Hz) with depth. At 1 Hz we observe almost 10× reduction at 4100 ft as compared to the 300 ft depth, which is consistent with theoretical expectations for suppression of surface seismic waves with depth.

high frequency noise (1 – 10 Hz), which seems to stem from surface wind and anthropogenic sources, by an order of magnitude at 4100-ft level compared to near-surface station (300-ft).

The next step is to understand the different seismic noise fields and their propagation properties that would help us construct better Newtonian noise subtraction filters. These filters would need to provide another 100× suppression at 1 Hz in order to reduce the noise levels needed by the next generation GW detectors.

4.3 Seismic field decomposition

One of the important factors in implementing an optimal Newtonian noise filter is the understanding of short term and long term stability of different wave fields (for example, surface and body waves). The calculation of filter coefficients heavily depends on the temporal stability of the wave fields. Using a shorter data segment might prove to be too noisy and using a longer segment might average out the effects. Hence it is desirable to first understand

different wave fields and their structure, and then construct the filter coefficients.

To understand field composition and determine source locations there are various algorithms currently used in seismology. They are collectively known as beamforming methods and are common in many other branches of science involving signal extraction and source localization. All beamforming methods use the fact that signals with finite propagation velocity will reach different recording stations at different times and will affect the stations differently depending on how they are polarized.

Under the assumption of uniform propagation media, a set of time shifts that maximize the cross-correlation of data between all pairs of stations would uniquely identify the source location, provided there are at least three seismometers. The precision of identified locations would depend on local noise, timing accuracy and the number of seismometers used. Since a priori the signal source location is not known, a scan of all sets of possible time-shifts are performed and the one(s) that maximize cross-correlation between different pairs of seismometers are considered to correspond to source locations. Apart from the time shifts, the response functions of the seismometers can be used to extract additional details about the signals, such as its polarization. In general, time-shifts and response functions are used together to decipher signal properties.

There exist a variety of beam forming methods and in this section we look at some of them. For a comprehensive list, please refer to [137, 103]. We also discuss a maximum likelihood method generally used for GW analyses.

4.4 Beamforming methods

Let us assume a two-dimensional array with M seismometers with positions denoted by (x_m, y_m) (it is easy to extend this analysis to three dimensions). Also for simplicity let us assume a single point source emitting signal at a particular frequency f . In such a case the array propagation vector (also called array response function, which is a vector constructed

from individual seismometer response functions) $\mathbf{a}(f, \vec{\mathbf{k}}, \theta)$ can be written as,

$$\mathbf{a}(f, \vec{\mathbf{k}}, \theta) = \begin{bmatrix} e^{-i(k_x x_1 + k_y y_1)} \\ \vdots \\ e^{-i(k_x x_m + k_y y_m)} \end{bmatrix}, \quad (4.2)$$

where (k_x, k_y) are components of wave vector $\vec{\mathbf{k}}$ of the signal ($k = \frac{2\pi f}{v}$, v is speed of the signal) and θ is a set of signal parameters of interest (for example, amplitudes of different wave components). The recorded data $\mathbf{X}(f)$ at each seismometer is then given by

$$\mathbf{X}(f) = \mathbf{a}(f, \vec{\mathbf{k}}, \theta)s(f) + \mathbf{N}(f), \quad (4.3)$$

where, $s(f)$ is signal at source location and $\mathbf{N}(f)$ is local noise at each seismometer. The goal of various beamforming techniques is to recover the signal properties (location, speed etc.) from the observations $\mathbf{X}(f)$.

The beamforming methods can be broadly classified into two categories: spectral based methods (non-parametric methods) and parametric methods.

4.4.1 Spectral based methods

Spectral based methods, also called non-parametric methods, make minimum assumptions about the signal and try to recover signal parameters based on spectrum (Fourier transform) of observed data. Below we describe some of the most common non-parametric methods.

Conventional (Bartlett) beamformer

This is the simplest of all beamforming methods. In this method we maximize the sum of covariances between all pairs of seismometers using a set of $(\vec{\mathbf{k}}, \theta)$. In the presence of signal, a maximum would occur corresponding to signal parameters $(\vec{\mathbf{k}}_s, \theta_s)$. The quantity that is maximized in this method is given by [103]

$$P_{\text{BF}}(\vec{\mathbf{k}}, \theta) = \frac{\mathbf{a}^{\text{H}} \hat{\mathbf{R}} \mathbf{a}}{\mathbf{a}^{\text{H}} \mathbf{a}}, \quad (4.4)$$

where $\hat{\mathbf{R}}$ is the measured covariance matrix $[\mathbf{X}(f)\mathbf{X}^H(f)]$. This method is robust and simple, but lacks in accuracy (see Figure 4.12). Also suffers from strong aliasing effect (see Figure 4.11).

Capon Beamformer (MVDR)

This method is also known as minimum variance distortionless response (MVDR) beamformer. This comes under the class adaptive beamformers that are capable of steering the array in the direction of interest while suppressing the signals from other directions. The quantity used for maximization in this method is given by [103]

$$P_{\text{Capon}}(\vec{\mathbf{k}}, \theta) = \frac{1}{\mathbf{a}^H \hat{\mathbf{R}}^{-1} \mathbf{a}} . \quad (4.5)$$

There are many variants of Capon beamformer and each of them use a slightly different quantity for maximization. The one that uses (4.5) is called standard Capon method. Compared to Bartlett beamformer, Capon beamformers have better accuracy (see Figure 4.12) and suffer less from aliasing (see Figure 4.11).

Subspace based methods

In the previous methods we used the covariance matrix $\hat{\mathbf{R}}$ obtained from cross-correlating data from different pairs of seismometers without any modifications. But in reality not all components of $\hat{\mathbf{R}}$ are useful, some of them may not carry any information about the signal. In such cases we could condition the matrix $\hat{\mathbf{R}}$, for example using singular value decomposition. The singular value decomposition of \mathbf{R} is written as

$$\mathbf{R} = \mathbf{U}_s \mathbf{\Lambda}_s \mathbf{U}_s^H + \mathbf{U}_n \mathbf{\Lambda}_n \mathbf{U}_n^H , \quad (4.6)$$

where $(\mathbf{\Lambda}_s, \mathbf{\Lambda}_n)$ and $(\mathbf{U}_s, \mathbf{U}_n)$ are eigenvalues and eigenvectors of \mathbf{R} . Subscripts s and n correspond to signal and noise respectively. The eigenvalues corresponding to the signal would be in general larger than the eigenvalues corresponding to noise. Since a priori we do not know about the signal, we order the eigenvalues and select the ones with largest

standard deviation (outliers) as corresponding to signal. Then the projection operators to signal and noise space can then be written as

$$\mathbf{\Pi}^s = \mathbf{U}_s \mathbf{U}_s^H \quad \text{and} \quad \mathbf{\Pi}^n = \mathbf{U}_n \mathbf{U}_n^H . \quad (4.7)$$

Instead of \mathbf{R} we can use these projection operators for optimization to find $(\vec{\mathbf{k}}_s, \theta_s)$. Such methods of using projection operators to find signals are called sub-space based methods. One of those methods, called MUltiple SIgnal Classification (MUSIC), uses [103]

$$P_{\text{MUSIC}} = \frac{\mathbf{a}^H \mathbf{a}}{\mathbf{a}^H \hat{\mathbf{\Pi}}^n \mathbf{W} \hat{\mathbf{\Pi}}^n \mathbf{a}} \quad (4.8)$$

for maximization. For standard MUSIC method, $\mathbf{W} = \mathbf{I}$ (note $\mathbf{\Pi}^2 = \mathbf{\Pi}$). There are other MUSIC methods that use different \mathbf{W} .

4.4.2 Parametric methods

Unlike spectral based methods, parametric methods utilize a data model to look for signals. Assuming a data model has both advantages and disadvantages. If the model used is close to the actual one, we can recover the signal and determine signal properties with very high accuracy. But if the assumed model is not correct then this method would yield inconsistent results.

Maximum Likelihood

One of the prominent such methods is the maximum likelihood method. Assuming noise is stationary Gaussian white random process with variance σ^2 , a likelihood function for $\mathbf{X}(f)$ can be written as

$$L(\theta, s(t), \sigma^2) = \frac{1}{\sigma^{2M}} e^{-|\mathbf{X}(f) - \mathbf{a}(\theta)s(f)|^2 / \sigma^2} , \quad (4.9)$$

where M corresponds to the number of seismometers. By minimizing the negative log-likelihood of the above function, we get

$$\hat{\theta}_{\text{ML}} = \min_{\theta} \text{Tr} \left(\Pi_{\mathbf{a}}^n \hat{\mathbf{R}} \right) \quad (4.10)$$

where $\Pi_{\mathbf{a}}^n = \mathbf{I} - \mathbf{a}(\mathbf{a}^H \mathbf{a})^{-1} \mathbf{a}^H$. The set of parameters that minimize the above function will correspond to the signal.

There are also other methods that combine both maximum likelihood and sub-space methods and are generally called subspace fitting. We do not discuss them here.

Stochastic radiometer method

The cross-correlation method derived in Chapter 2 can also be used for seismic signal identifications and parametrization. Following the derivation in Section 2.2, we can write the average cross-power measured by a pair of seismometer channels α and β in a single frequency bin of width Δf as (see Eq. (2.33))

$$\langle Y_{i\alpha, j\beta}(f) \rangle = 2 T \Delta f \sum_A \int_{S^2} d\hat{\Omega} H_A(f, \hat{\Omega}) Q_{A, i\alpha}(f, \hat{\Omega}) Q_{A, j\beta}(f, \hat{\Omega}) e^{-2\pi i f \hat{\Omega} \cdot \Delta \vec{x}_{ij} / v_A}, \quad (4.11)$$

where H_A is the power spectra of wave component A and $Q_{A, i\alpha}$ is the response of α channel of seismometers i to the wave component A . There are a couple of key differences between Eq. (2.33) and Eq. (4.11). In Eq (2.33), we combined the cross-power from different polarization (here we call them as wave components) assuming they contribute equally and defined a polarization independent $H(f)$ (see Eq. (2.13)). Since here we want to decompose the signal into its wave components, we do not combine the power spectra (and also note that here they need not be equal). The second difference comes from the velocity term used in those equations. In Eq. (2.33), both $+$ and \times polarization travel at the same speed, speed of light, while here different wave components will travel at different speeds. Also note that here we have folded the antenna responses F_A , explicitly written in Eq. (2.33), into $Q_{A, i\alpha}$.

We can parametrize the amplitude spectra $H_A(\hat{\Omega})$ in terms of a basis $B_A(\hat{\Omega})$ to study

the spatial distribution of seismic wave component A :

$$H_A(\hat{\Omega}) = \sum_n S_{A,n} B_{A,n}(\hat{\Omega}), \quad (4.12)$$

where $S_{A,n}$ corresponds to ‘ A ’ component cross-power in basis element n .

There are two useful bases one can use: spherical harmonics basis, $B(\hat{\Omega}) = Y_{lm}(\hat{\Omega})$ and pixels basis, $B_{\hat{\Omega}_0}(\hat{\Omega}) = \delta(\hat{\Omega} - \hat{\Omega}_0)$. In either case, we can define

$$\gamma_{A,i\alpha,j\beta}(f) = \int_{S^2} d\hat{\Omega} B_A(\hat{\Omega}) Q_{A,i\alpha}(f, \hat{\Omega}) Q_{A,j\beta}(f, \hat{\Omega}) e^{-2\pi i f \hat{\Omega} \cdot \Delta \vec{x}_{ij} / v_A}, \quad (4.13)$$

so that Eq. (4.11) can be simplified as

$$\langle Y_{i\alpha,j\beta}(f) \rangle = 2T \Delta f \sum_A \gamma_{A,n,i\alpha,j\beta} S_{A,n}, \quad (4.14)$$

where repeated indices n are summed over. Since we are interested in estimating the coefficients $S_{A,n}$, we define the likelihood function,

$$L \propto \exp(-[Y_i^* - \gamma_{id}^* S_d] N^{-1} [Y_i - \gamma_{id} S_d]) \quad (4.15)$$

where i runs over all seismometer/channel pairs and d runs over all basis elements. If we assume that all seismometers and channels have similar noise floor, constant in time, N becomes proportional to identity matrix and we can ignore it in the likelihood maximization. The likelihood maximization of Eq. (4.15) then gives

$$\mathbf{S}_{\text{rad}} = (\gamma^\dagger \gamma)^{-1} \gamma^\dagger \hat{\mathbf{Y}}, \quad (4.16)$$

where \dagger corresponds to conjugate-transpose and $\hat{\mathbf{Y}}$ is the covariance (or) cross-correlation matrix $\hat{\mathbf{R}}$. The vector \mathbf{S}_{rad} is of length $A \times n$ and contains the cross-power due to each wave components A in every basis element n .

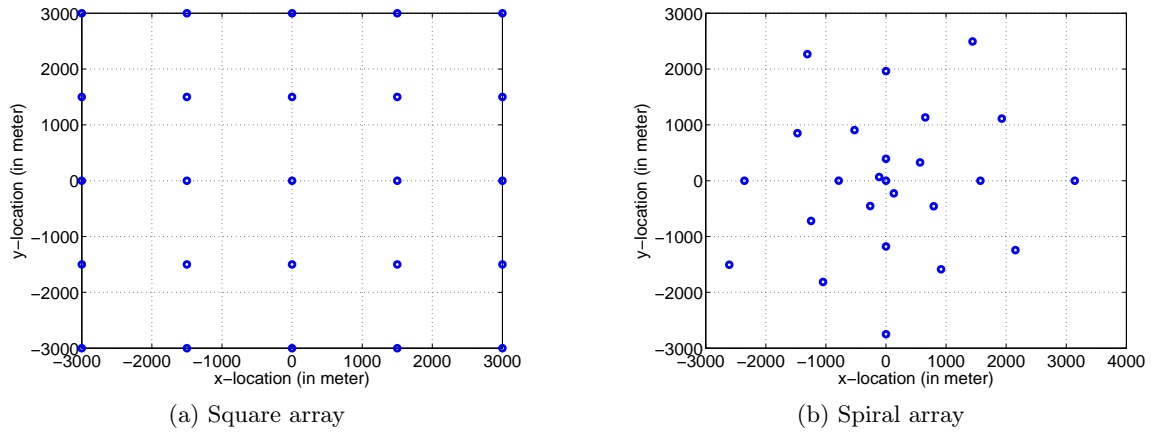


Figure 4.10: Plots of square (left) and spiral array (right), each consisting of 25 seismometers, used for 2D simulations.

4.4.3 Simulation results

To compare different beamforming methods we performed 2D and 3D simulations. For 2D simulations we used square and spiral arrays made up of 25 stations on the surface as shown in Figure 4.10.

Figure 4.11 and Figure 4.12 show simulations and recovery of single Rayleigh wave source (affecting only z -channels of seismometers) using four different methods described in Section 4.4 for square and spiral array set-ups. The frequency and the speed of seismic waves were 1 Hz and 2400 m/sec respectively. From Figure 4.11 and Figure 4.12, we find that a square array produces strong aliasing (multiple source location identification) in all four beamforming methods, while spiral array do not. Hence for later simulations we only used spiral or random arrays. Also from Figure 4.12, we note that signal recovery using Bartlett beamformer has larger spread than other three beamformers.

Figure 4.13 shows the simulation and recovery of four sources using spiral array of 25 seismometers placed on the surface. All the sources were placed far away from the array, so that we can use plane wave approximation. The frequencies of the simulated seismic waves were all 1 Hz, but had different velocities. From the simulations with four Rayleigh wave sources, we find that while Bartlett, MUSIC and GW radiometer methods perform

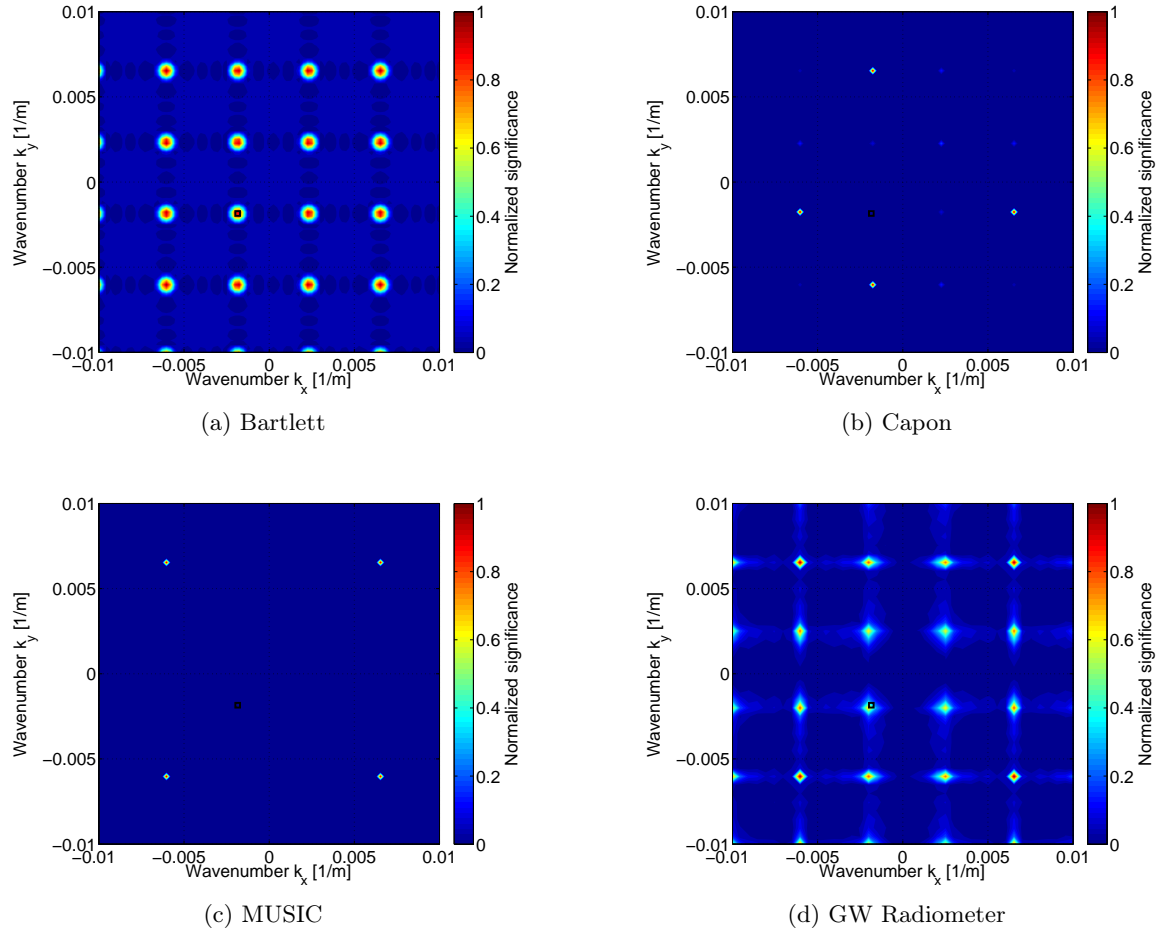


Figure 4.11: Simulation and recovery of single Rayleigh wave source using four different beamforming methods. For this simulation, we used a square array of 25 stations on the surface. The black marker shows the intended simulation location and the color indicates the likelihood of recovery ('red' corresponds to highly likely). We find that there is strong aliasing in all the four cases.

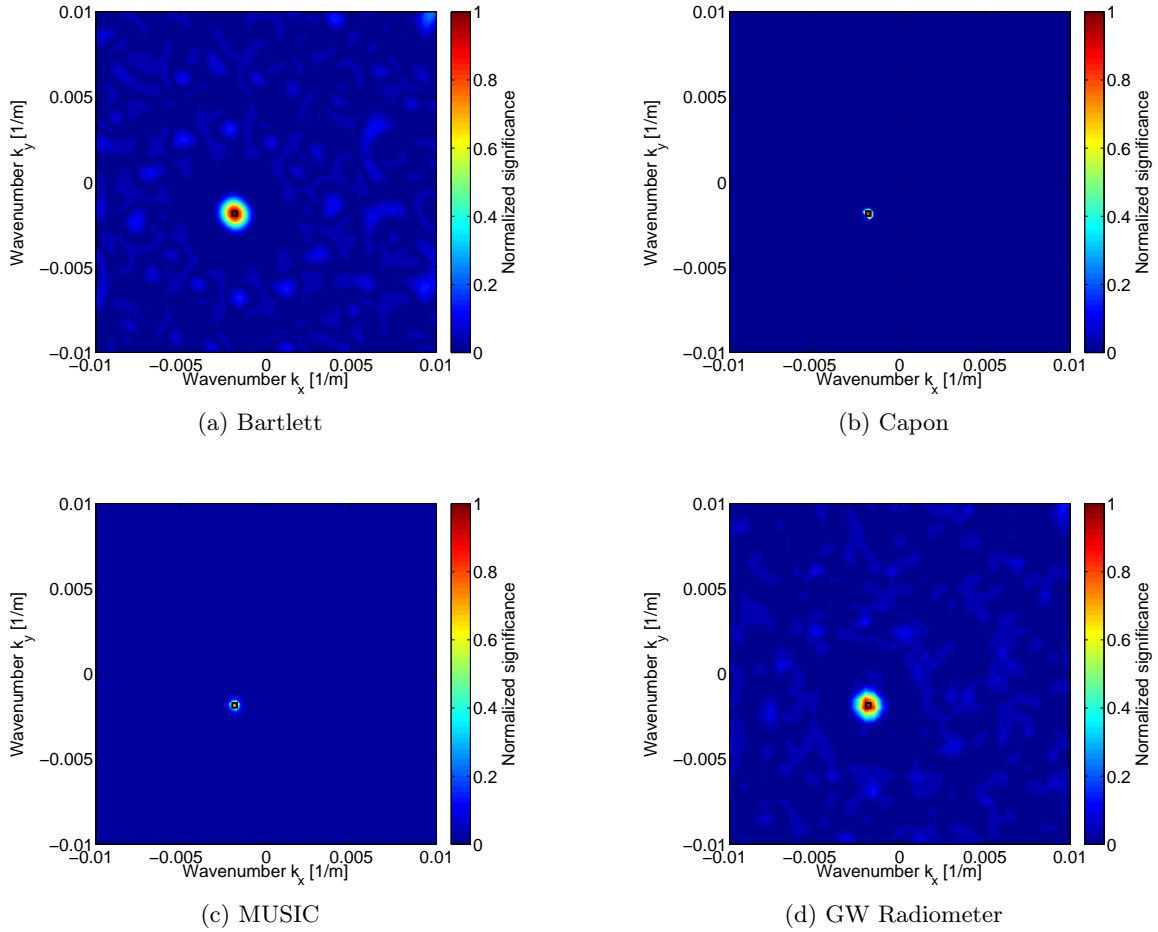


Figure 4.12: Simulation and recovery of single Rayleigh wave source using four different beamforming methods. For this simulation, we used a spiral array of 25 stations on the surface. The black marker shows the intended simulation location and the color indicates the likelihood of recovery ('red' corresponds to highly likely).

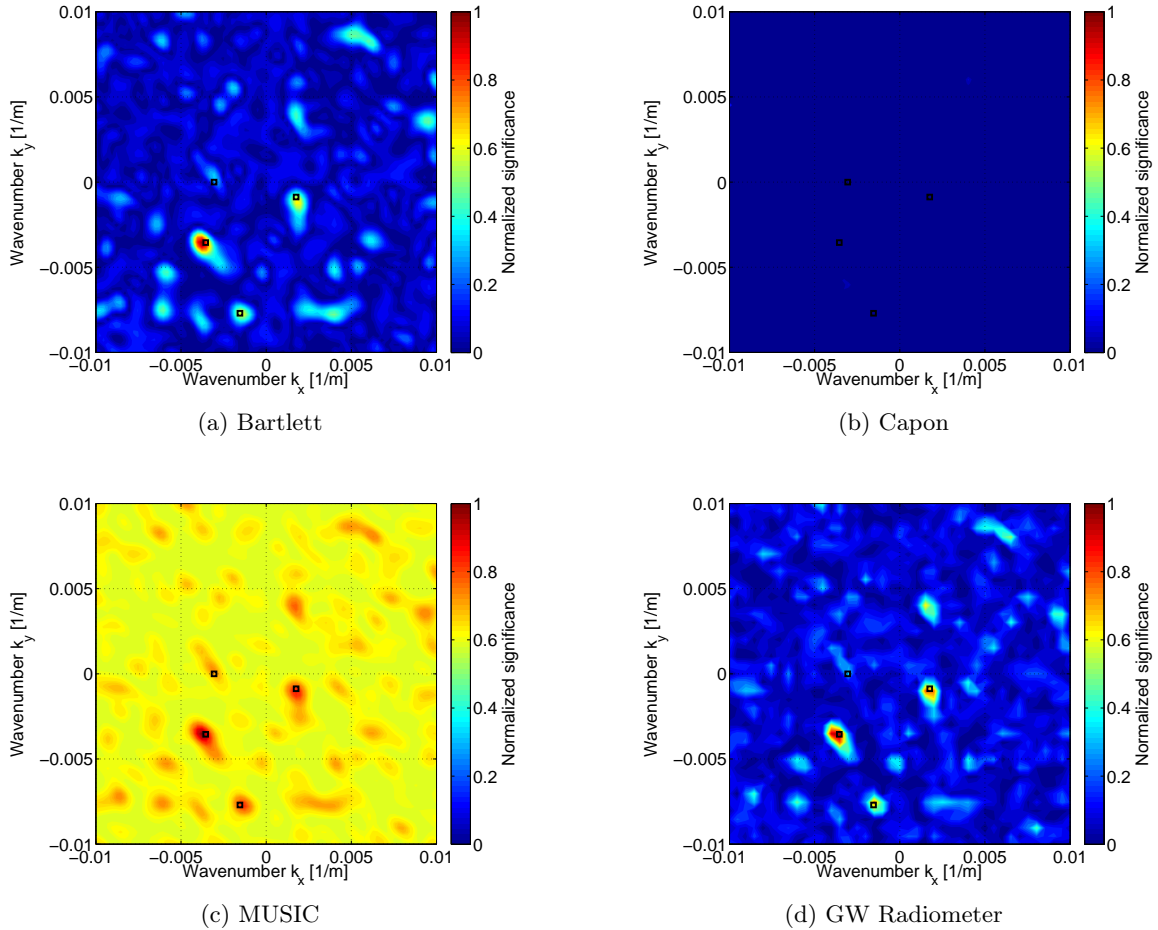


Figure 4.13: Simulation and recovery of four Rayleigh wave sources using four different beamforming methods. For this simulation, we used a spiral array of 25 stations on the surface. The black markers show the intended simulation locations and the color indicates the likelihood of recovery ('red' corresponds to highly likely).

well, capon method suffers from signal cancellation and hence does not recover the signals. This problem of signal cancellation in standard capon method for coherent signals is already discussed in literature [144] and hence not surprising. Both MUSIC and GW radiometer methods recover signals with high signal-to-noise ratio compared to Bartlett beamformer.

We also performed 3D simulations, which are rare in seismological literature due to almost non-existence of 3D seismic arrays. Figure 4.14 shows simulation of and recovery of two P-wave sources in a 3D set-up consisting of 49 seismometers randomly placed (to avoid aliasing effects) in a 16 km^3 volume.

We also performed simulations of wave component identification using GW radiometer method. The γ in Eq. (4.16) is defined as

$$\gamma_{i\alpha, j\beta, \hat{\Omega}} = Q_{i\alpha, \hat{\Omega}} Q_{j\beta, \hat{\Omega}} e^{-2\pi i f \hat{\Omega} \cdot \Delta \vec{x}_{ij} / v} \quad (4.17)$$

where Q 's are responses of seismometer channels to a seismic wave coming from direction $\hat{\Omega}$ and v is the speed of the seismic wave. Here i, j run over all seismometers and α, β run over different channels of seismometer (x, y, z) . By constructing proper filters $Q_{i\alpha, \hat{\Omega}}$ we can identify and separate out different wave components. Figure 4.15 shows simulation and recovery of one P-wave (underground source) and one simple R-wave (surface source). The P-wave filter is defined by the response function

$$Q_{i\alpha} = \hat{\Omega} \cdot \vec{\alpha} = \cos \theta_{\alpha} . \quad (4.18)$$

Here we use the approximation $Q_{i\alpha} = Q_{\alpha}$, which is true for sources that are far away (plane wave approximation). The R-wave filter is defined by the response function,

$$Q_{i\alpha} = e^{-k Z_i} \delta_{z, \alpha} . \quad (4.19)$$

Here Z_i is the 'Z' location of i^{th} seismometer, k is a constant defined by the equation $e^{-4000 k} = 0.1$ (to provide expected order of magnitude suppression of R-wave at a depth of 4000 meters) and δ is the Kronecker delta function. Using these two filters, we were able

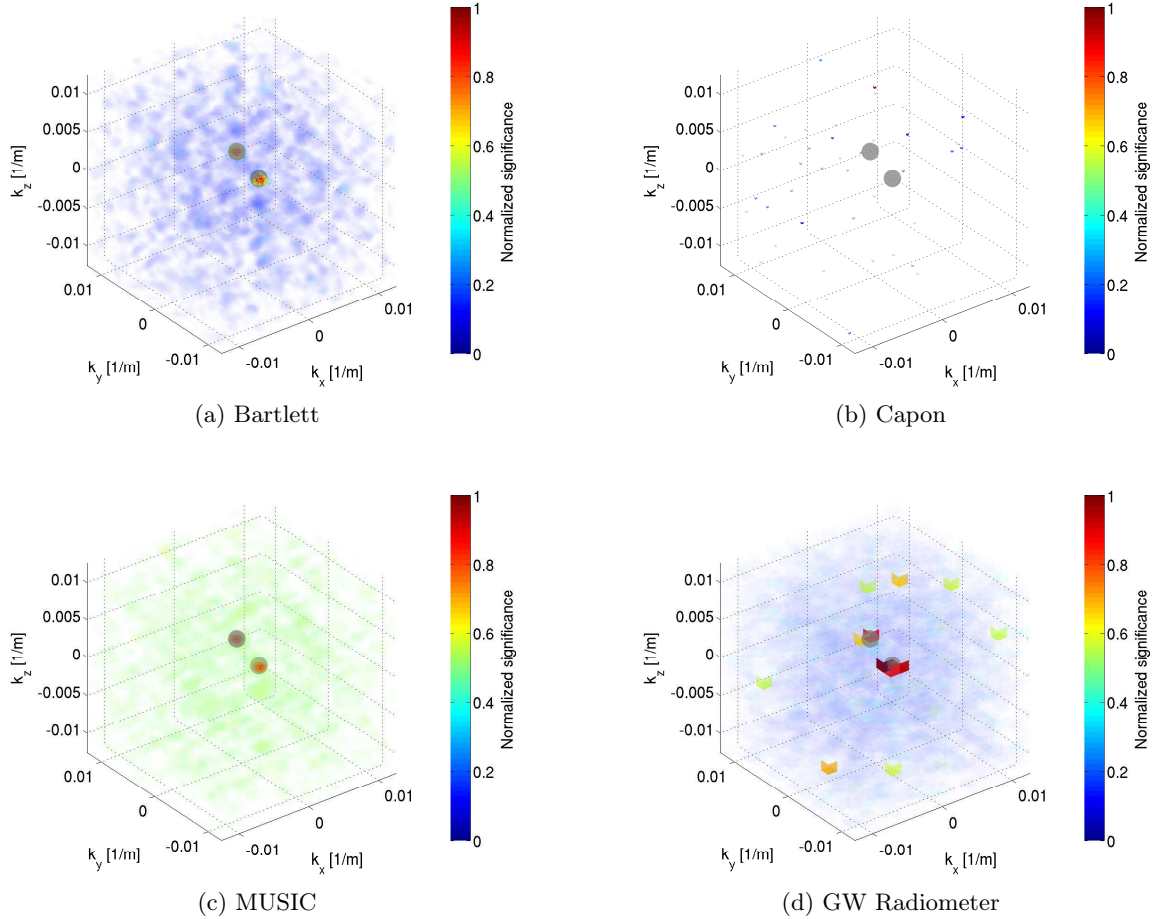


Figure 4.14: 3D simulation and recovery of two P-wave wave sources using four different beamforming methods. For this simulation, we used 49 stations randomly distributed in a 16km^3 volume. The boxes show the intended simulation locations and the color indicates the likelihood of recovery ('red' corresponds to highly likely). Due to computational (memory) problem, GW radiometer method was performed using coarser resolution.

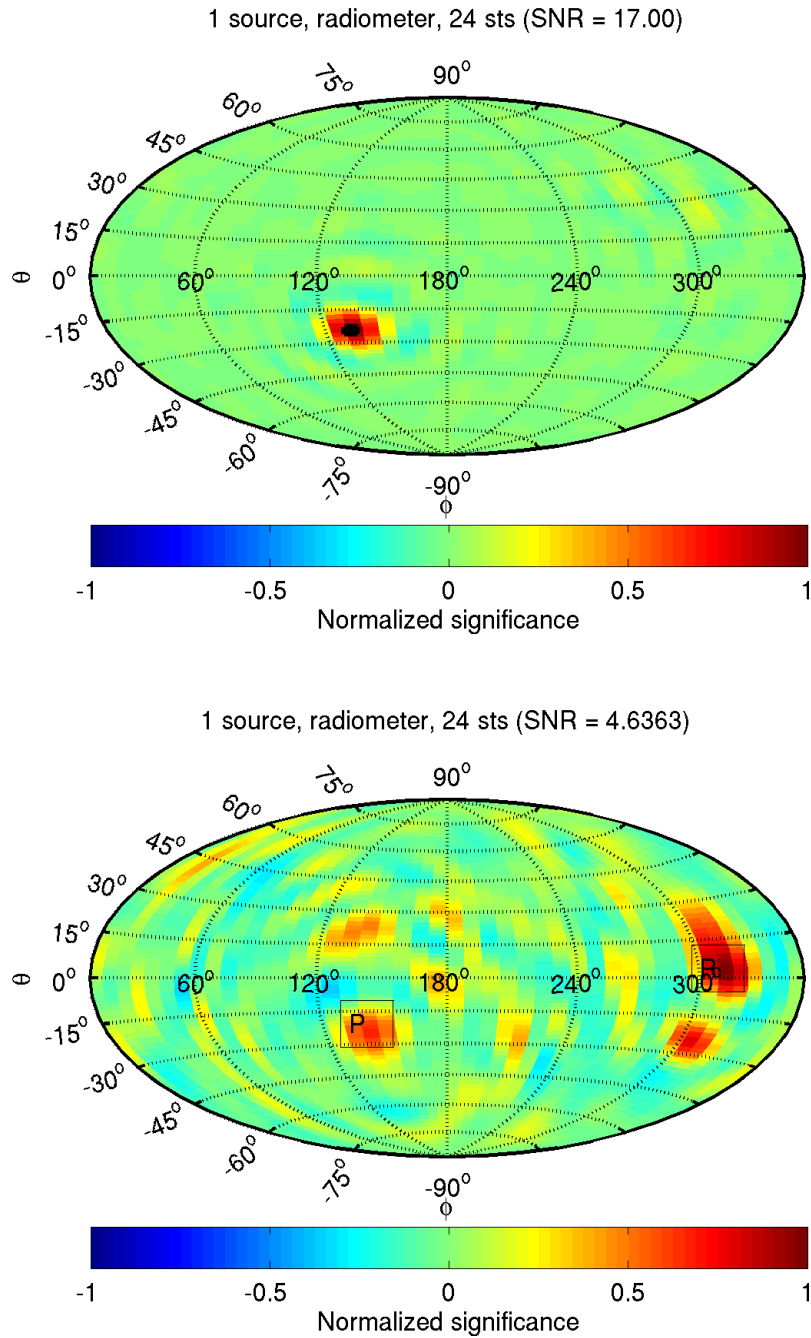


Figure 4.15: Recovery of simulated P and R-waves using corresponding filters. The P-wave was placed underground and R-wave on the surface ($\theta = 0$). The top plot uses P-wave filter and the bottom plot uses R-wave filter.

to differentiate between two wave components to a good extent. However there is a little bit of overlap between the two filters, because of the non-orthogonality (the filters are not completely orthogonal). We are currently developing filters that would be orthogonal and that would include more complex wave compositions.

4.5 Summary

In this chapter, we discussed seismic and Newtonian noise and their impact on current and future generation of GW detectors. We showed they would be significant noise sources at ~ 1 Hz in the future generation of ground based GW detectors. We discussed the possibility of Newtonian noise subtraction and the necessity for understanding different seismic wave fields. We described the seismic array constructed in Homestake mine, South Dakota to study seismic waves underground and its benefit for the design of future underground GW detectors. At the end we discussed different beamforming techniques to identify seismic wave source locations and also use of GW analysis based beamforming technique to identify different seismic wave components. We then showed results for 2D and 3D simulations, using different beamforming techniques. We also showed, for the first time, that using GW radiometer method we can recover seismic signals in a 3D set-up.

Chapter 5

Conclusion and Discussion

Nearly a century after the conception of general relativity, the direct detection of gravitational waves, one of the main predictions of general relativity, is within our grasp. The coming decade of advanced gravitational-wave detectors [71, 67, 85, 105] offers promising opportunities for such a detection. Similar to the detection of cosmic microwave background, it will open up a new era in the field of observational cosmology.

In this thesis, we studied two kinds of gravitational waves: stochastic gravitational waves and long gravitational-wave transients. Stochastic gravitational waves are expected to arise from the events that took place during the early universe or from a collection of recent astrophysical objects such as binary neutron stars. In Chapter 2 we looked at some of the models stochastic gravitational waves and an analysis pipeline to look for such signals in LIGO S5 data. In Section 2.4 and Section 2.5, we presented the results using non-colocated and colocated LIGO detectors, neither of which resulted in detection of SGWB. However, these results provided useful upper limits that were used to constrain some of the cosmological models of stochastic gravitational-wave background. They were also the first set of results from direct (non)observation of gravitational waves that were on par with the indirect bounds obtained from cosmological models such as Big-Bang-Nucleosynthesis. The next generation of gravitational-wave detectors are likely to observe or set significant constraints on many of those models.

In Chapter 3 we studied transient gravitational waves with time scales ranging from minutes to weeks. We looked at some of the models in detail and developed a new analysis

pipeline to look for such gravitational wave signals. We applied the pipeline to look for gravitational wave signals from Gamma-ray bursts and did not find any signals. We placed distance upper limits on some of the models [161] to be as far as 33 Mpc. Many of the sources we considered in that chapter (see Section 3.1) are plausible targets for the advanced detector era. Any detection of such gravitational waves will provide invaluable information about the relevant objects and processes, for which we currently possess only preliminary models, e.g., long gamma-ray bursts. If, on the other hand, no long gravitational wave transients are detected, we can rule out or constrain some of the models that predict relatively large strain amplitudes (e.g., [162]).

In Chapter 4 we studied the effect of seismic and Newtonian noise on current and future generation of gravitational wave detectors. We demonstrated that they would be the dominant noise sources at frequencies ~ 1 Hz around which there are many interesting astrophysical and cosmological sources. We discussed the possibility of noise subtraction methods and the necessity for understanding seismic field composition. We showed that at ~ 4000 ft below the surface, the seismic noise levels are an order magnitude smaller (see Figure 4.9) lending support to the idea of building the next generation of gravitational wave detectors underground. Finally, we also looked at some of the algorithms for decomposing seismic wave fields. In the future, such algorithms will not only be useful in the field of gravitational wave detection, but will also play an important role in geophysics as a tool for understanding seismic wave fields in general.

References

- [1] J. Aasi et al. Enhanced sensitivity of the LIGO gravitational wave detector by using squeezed states of light. *Nature Photonics*, 7:613–619, 2013.
- [2] J. Abadie et al. All-sky search for gravitational-wave bursts in the first joint LIGO-GEO-Virgo run. *Phys. Rev. D*, 81(10):102001, 2010.
- [3] J. Abadie et al. Search for gravitational-wave inspiral signals associated with short gamma-ray bursts during ligo’s fifth and virgo’s first science run. *Astrophys. J.*, 715:1453, 2010.
- [4] J. Abadie et al. Implications for the origin of GRB 051103 from LIGO observations. *Astrophys. J.*, 755:2, 2012.
- [5] J. Abadie et al. Upper limits on a stochastic gravitational-wave background using LIGO and Virgo interferometers at 600-1000 Hz. *Phys. Rev. D*, 85:122001, 2012.
- [6] B. Abbott et al. Detector description and performance for the first coincidence observations between LIGO and GEO. *Nucl. Instrum. and Meth. in Phys. Research Sec. A*, 517:154, 2004.
- [7] B. Abbott et al. Searching for a stochastic background of gravitational waves with the laser interferometer gravitational-wave observatory. *Astrophys. J.*, 659:918, 2007.
- [8] B. Abbott et al. Upper limit map of a background of gravitational waves. *Phys. Rev. D*, 76:082003, 2007.

- [9] B. Abbott et al. Implications for the origin of GRB 070201 from LIGO observations. *Astrophys. J.*, 681:1419, 2008.
- [10] B Abbott et al. All-Sky LIGO Search for Periodic Gravitational Waves in the Early Fifth-Science-Run Data. *Phys. Rev. Lett.*, 102(11):111102, 2009.
- [11] B Abbott et al. Einstein@Home search for periodic gravitational waves in LIGO S4 data. *Phys. Rev. D*, 79:022001, 2009.
- [12] B. Abbott et al. LIGO: the laser interferometer gravitational-wave observatory. *Reports on Prog. in Phys.*, 72:076901, 2009.
- [13] B Abbott et al. Stacked search for gravitational waves from the 2006 SGR 1900+14 storm. *Astrophys. J. Lett.*, 701:68–74, 2009.
- [14] B. Abbott et al. An upper limit on the stochastic gravitational-wave background of cosmological origin. *Nature*, 460:990, 2009.
- [15] B. P. Abbott et al. Search for Gravitational-Wave Bursts from Soft Gamma Repeaters. *Phys. Rev. Lett.*, 101(21):211102, 2008.
- [16] B. P. Abbott et al. Search for gravitational-wave bursts associated with gamma-ray bursts using data from ligo science run 5 and virgo science run 1. *Astrophys. J.*, 715:1438, 2010.
- [17] O. D. Aguiar. Past, present and future of the resonant-mass gravitational wave detectors. *Res. Astron. Astrophys.*, 11(1):1, 2011.
- [18] B. Allen. Relativistic gravitation and gravitational radiation. *Proceedings of the Les Houches School on Astrophysical Sources of Gravitational Waves (Cambridge University Press)*, page 373, 1997.
- [19] B. Allen and J. Romano. Detecting a stochastic background of gravitational radiation: Signal processing strategies and sensitivities. *Phys. Rev. D*, 59:102001, 1999.

- [20] W. G. Anderson, P. R. Brady, J. D. E. Creighton, and É. É. Flanagan. An excess power statistic for detection of burst sources of gravitational radiation. *Phys. Rev. D*, 63:042003, 2001.
- [21] N. Andersson, G. L. Comer, and D. Langlois. Oscillations of general relativistic superfluid neutron stars. *Phys. Rev. D*, 66:104002, 2002.
- [22] ATNF. The ATNF Pulsar Database. <http://www.atnf.csiro.au/people/pulsar/psrcat/>, 2013.
- [23] L. Baiotti, R. De Pietri, G. M. Manca, and L. Rezzolla. Accurate simulations of the dynamical bar-mode instability in full general relativity. *Phys. Rev. D*, 75:044023, 2007.
- [24] R. Bar-Kana. Limits on direct detection of gravitational waves. *Phys. Rev. D*, 50:1157, 1994.
- [25] P.L. Bender, K. Danzmann, and the LISA Study Team. Laser interferometer space antenna for the detection and observation of gravitational waves: Pre-phase a report. *2nd Edition, Max-Planck Institut fuer Quantenoptik, MPQ233*, 1998.
- [26] P.L. Bender and D. Hils. Confusion noise level due to galactic and extragalactic binaries. *Class. Quantum Grav.*, 14:1439, 1997.
- [27] C. Bennet et al. First-year *wilkinson microwave anisotropy probe (wmap)* observations: Preliminary maps and basic results. *Astrophys. J. Supplement Series*, 148:1, 2003.
- [28] L. Bildsten. Gravitational radiation and rotation of accreting neutron stars. *Astrophys. J. Lett.*, 501(1):L89, 1998.
- [29] L. Blackburn et al. The LSC glitch group: monitoring noise transients during the fifth LIGO science run. *Class. Quantum Grav.*, 25:184004, 2008.
- [30] R. Bondarescu, S. A. Teukolsky, and I. Wasserman. Spin evolution of accreting neutron

- stars: Nonlinear development of the r-mode instability. *Phys. Rev. D*, 76(6):064019, 2007.
- [31] R. Bondarescu, S. A. Teukolsky, and I. Wasserman. Spinning down newborn neutron stars: Nonlinear development of the r-mode instability. *Phys. Rev. D*, 79(10):104003, 2009.
- [32] L. Boyle and A. Buonanno. Relating gravitational wave constraints from primordial nucleosynthesis, pulsar timing, laser interferometers, and the cmb: Implications for the early universe. *Phys. Rev. D*, 78:043531, 2008.
- [33] R. Brustein. Relic gravitational waves from string cosmology. *Phys. Lett. B*, 361:45, 1995.
- [34] N. Bucciantini, E. Quataert, B. D. Metzger, T. A. Thompson, J. Arons, and L. Del Zanna. Magnetized relativistic jets and long-duration GRBs from magnetar spin-down during core-collapse supernovae. *Mon. Not. R. Ast. Soc.*, 396:2038, 2009.
- [35] V. Mandic C. Wu and T. Regimbau. Accessibility of the gravitational-wave background due to binary coalescences to second and third generation gravitational-wave detectors. *Phys. Rev. D*, 85:104024, 2012.
- [36] S. W. Caddey and R. L. Bachman. The homestake gold mine, an early proterozoic iron-formation-hosted gold deposit, lawrence county, south dakota. 1991.
- [37] J. M. Centrella, editor. *Rotational instabilities in post-collapse stellar cores*, 2001.
- [38] S. Chandrasekhar. The Effect of Gravitational Radiation on the Secular Stability of the Maclaurin Spheroid. *Astrophys. J.*, 161:561, 1970.
- [39] S. Chatterji, L. Blackburn, G. Martin, and E. Katsavounidis. Multiresolution techniques for the detection of gravitational-wave bursts. *Class. Quantum Grav.*, 21:S1809, 2004.

- [40] N. Christensen. Measuring the stochastic gravitational radiation background with laser interferometric antennas. *Phys. Rev. D*, 46:5250, 1992.
- [41] Planck Collaboration. Planck 2013 results. XXII. Constraints on inflation. *arXiv:1303.5082*, 2013.
- [42] The LIGO Scientific Collaboration and The Virgo Collaboration. An upper limit on the stochastic gravitational-wave background of cosmological origin. *Nature*, 460:990, 2009.
- [43] The LIGO Scientific Collaboration and the Virgo Collaboration. A search for long-lived gravitational-wave transients coincident with long gamma-ray bursts. *arXiv:1309.6160*, 2013.
- [44] A Corsi and P Mészáros. Gamma-ray burst afterglow plateaus and gravitational waves. *Class. Quantum Grav.*, 26:204016, 2009.
- [45] A. Corsi and P. Mészáros. Gamma-ray Burst Afterglow Plateaus and Gravitational Waves: Multi-messenger Signature of a Millisecond Magnetar? *Astrophys. J.*, 702:1171, 2009.
- [46] C. Cutler. Gravitational waves from neutron stars with large toroidal b fields. *Phys. Rev. D*, 66:084025, 2002.
- [47] R.H. Cyburt et al. New BBN limits on physics beyond the standard model from ${}^4\text{He}$. *Astroparticle Phys.*, 23:313, 2005.
- [48] T. Damour, B. R. Iyer, and B. S. Sathyaprakash. Comparison of search templates for gravitational waves from binary inspiral. *Phys. Rev. D*, 63:044023, 2001.
- [49] T. Damour and A. Vilenkin. Gravitational radiation from cosmic (super)strings: Bursts, stochastic background, and observational windows. *Phys. Rev. D*, 71:063510, 2005.

- [50] J A de Freitas Pacheco. Do soft gamma repeaters emit gravitational waves? *Astro. and Astrophys.*, 336:397, 1998.
- [51] S. R. Deans. *The Radon Transform and Some of Its Applications*. Dover Publications, Inc., 2 edition, 2007.
- [52] Jean-Fran çois Dufaux, Amanda Bergman, Gary Felder, Lev Kofman, and Jean-Philippe Uzan. Theory and numerics of gravitational waves from preheating after inflation. *Phys. Rev. D*, 76:123517, 2007.
- [53] É.É. E. E. Flanagan and S.A. Hughes. Measuring gravitational waves from binary black hole coalescences. i. signal to noise for inspiral, merger, and ringdown. *Phys. Rev. D*, 57:4535, 1998.
- [54] A. Buonanno et al. Spectrum of relic gravitational waves in string cosmology. *Phys. Rev. D*, 55:3330, 1997.
- [55] B. P. Abbott et al. All-sky ligo search for periodic gravitational waves in the early fifth-science-run data. *Phys. Rev. Lett.*, 102:111102, 2009.
- [56] B. P. Abbott et al. Search for gravitational waves from low mass binary coalescences in the first year of LIGO's S5 data. *Phys. Rev. D*, 79:122001, 2009.
- [57] B. P. Abbott et al. All-sky search for gravitational-wave bursts in the second joint ligo-virgo run. *Phys. Rev. D*, 85:122007, 2012.
- [58] Iyer. B. et al. Ligo-india tech. rep, 2012.
- [59] J. Harms et. al. Characterization of the seismic environment at the sanford underground laboratory, south dakota. *Class. Quantum Grav.*, 27(22):225011, 2010.
- [60] J. J. Hermes et. al. Rapid Orbital Decay in the 12.75-minute Binary White Dwarf J0651+2844. *The Astrophys. J. Lett.*, 757(2):L21, 2012.
- [61] J. Stachel et. al., editor. *The Collected papers of Albert Einstein, Volume 2: The Swiss Years: Writings, 1900-1909*. Princeton university press, 1990.

- [62] J. T. Whelan et. al. Treatment of calibration uncertainty in multi-baseline cross-correlation searches for gravitational waves. *arXiv:1205.3112*, 2012.
- [63] M.G. Beker et. al. Improving the sensitivity of future GW observatories in the 1-10 Hz band: Newtonian and seismic noise. *Gen. Rel. and Grav.*, 43(2):623–656, 2011.
- [64] P. J. Sutton et al. X-pipeline: an analysis package for autonomous gravitational-wave burst searches. *New Journal of Physics*, 12(5):053034, 2010.
- [65] R. Areda et al. Gravitational waves from electroweak phase transitions. *Nuclear Physics B*, 631:342, 2002.
- [66] S. Mitra et. al. Gravitational wave radiometry: Mapping a stochastic gravitational wave background. *Phys. Rev. D*, 77:042002, 2008.
- [67] T Accadia et. al. Virgo: a laser interferometer to detect gravitational waves. *Journal of Instrumentation*, 7(03):P03012, 2012.
- [68] J. Abadie et al. (LIGO Scientific Collaboration). Calibration of the LIGO gravitational wave detectors in the fifth science run. *Nucl. Instrum. Methods Phys. Res., Sect. A*, 624(1):223, 2010.
- [69] V. Fafone. Developments in resonant-mass detectors. *Class. Quantum Grav.*, 23(8):S223, 2006.
- [70] E.E. Flanagan. Sensitivity of the laser interferometer gravitational wave observatory to a stochastic background, and its dependence on the detector orientations. *Phys. Rev. D*, 48:2389, 1993.
- [71] G. M. Harry (for the LIGO Scientific Collaboration). Advanced ligo: the next generation of gravitational wave detectors. *Class. Quantum Grav.*, 27:084006, 2010.
- [72] N. Fotopoulos et al. Identifying correlated environmental noise in co-located interferometers with application to stochastic gravitational wave analysis. *Class. Quantum Grav.*, 23:S693, 2006.

- [73] N. Fotopoulos et al. Searching for stochastic gravitational-wave background with the co-located LIGO interferometers. *J. of Phy.: Conference Series*, 122:012032, 2008.
- [74] J. L. Friedman and B. F. Schutz. Secular instability of rotating Newtonian stars. *Astrophys. J.*, 222:281, 1978.
- [75] A. Archibald et. al G. Hobbs. The International Pulsar Timing Array project: using pulsars as a gravitational wave detector. *Class. Quant. Grav.*, 27(8):084013, 2010.
- [76] J. R. Gair, I. Mandel, and L. Wen. Improved time–frequency analysis of extreme-mass-ratio inspiral signals in mock LISA data . *Class. Quantum Grav.*, 25:184031, 2008.
- [77] T. J. Galama, P. M. Vreeswijk, J van Paradijs, et al. An unusual supernova in the error box of the γ -ray burst of 25 april 1998. *Nature*, 385:670, 1998.
- [78] N. Gehrels, J. P. Norris, S. D. Barthelmy, et al. A new γ -ray burst classification scheme from grb 060614. *Nature*, 444:1044, 2006.
- [79] N. Gehrels, E. Ramirez-Ruiz, and D. B. Fox. Gamma-ray bursts in the swift era. *Annu. Rev. Astron. Astrophys.*, 47:567, 2009.
- [80] K. Glampedakis, L. Samuelsson, and N. Andersson. Elastic or magnetic? A toy model for global magnetar oscillations with implications for quasi-periodic oscillations during flares. *Mon. Not. R. Ast. Soc. Lett.*, 371:74, 2006.
- [81] E. Goetz and K. Riles. PlaneMon: Airplane Detection Monitor. LIGO T050174-00-D, 2010.
- [82] G. González. Suspensions thermal noise in the LIGO gravitational wave detector. *Class. Quantum Grav.*, 17(21):4409, 2000.
- [83] L.P. Grishchuk. Primordial gravitons and possibility of their observation. *Soviet Physics JETP Letters*, 23:293, 1976.

- [84] L.P. Grishchuk and Yu.V. Sidorov. Squeezed quantum states of relic gravitons and primordial density fluctuations. *Phys. Rev. D*, 42:3413, 1990.
- [85] H Grote and the LIGO Scientific Collaboration. The GEO 600 status. *Class. Quantum Grav.*, 27(8):084003, 2010.
- [86] Stochastic Analysis Group. Companion Technical Note to the S3 Stochastic IFO-IFO Analysis Paper. LIGO-T050012-00-Z, 2005.
- [87] The Pennsylvania State University GWA Group. Gravitational wave interferometer noise calculator. <http://www.gwastro.org/for%20scientists/gravitational-wave-interferometer-noise-calculator>, 2013.
- [88] C.W. Helstrom. *Statistical Theory of Signal Detection*, volume 9 of *International Series of Monographs in Electronics and Instrumentation*. Pergamon Press, Oxford; New York, 2nd edition, 1968.
- [89] D. Hils and P.L. Bender. Gravitational radiation from helium cataclysmics. *Astrophys. J.*, 537:334, 2000.
- [90] D. Hils, P.L. Bender, and R.F. Webbink. Gravitational radiation from the galaxy. *Astrophys. J.*, 360:75, 1990.
- [91] R. Honda, S. Yamagishi, and N. Kanda. Astrophysically motivated time–frequency clustering for burst gravitational wave search: application to TAMA300 data. *Class. Quantum Grav.*, 25:184035, 2008.
- [92] J E Horvath. Energetics of the superflare from sgr1806-20 and a possible associated gravitational wave burst. *Modern Phys. Lett. A*, 20:2799, 2005.
- [93] K Ioka. Magnetic deformation of magnetars for the giant flares of the soft gamma-ray repeaters. *Mon. Not. R. Ast. Soc.*, 327:639, 2001.
- [94] J. Harms J. C. Driggers and R. X. Adhikari. Subtraction of newtonian noise using optimized sensor arrays. *Phys. Rev. D*, 86:102001, 2012.

- [95] V. Kalogera K. Belczynski and T. Bulik. A comprehensive study of binary compact objects as gravitational wave sources: Evolutionary channels, rates, and physical properties. *The Astrophys. J.*, 572(1):407, 2002.
- [96] P. M. Kalmus. *Search for Gravitational Wave Bursts from Soft Gamma Repeaters*. PhD thesis, Columbia University, 2008.
- [97] R. Khan and S. Chatterji. Enhancing the capabilities of ligo time-frequency plane searches through clustering. *Class. Quantum Grav.*, 26:155009, 2009.
- [98] T.W.B. Kibble. Topology of cosmic domains and strings. *Journal of Physics A*, 9:1387, 1976.
- [99] K. Kiuchi, Y. Sekiguchi, M. Shibata, and K. Taniguchi. Long-term general relativistic simulation of binary neutron stars collapsing to a black hole. *Phys. Rev. D*, 80(6):064037, 2009.
- [100] E. Komatsu et al. Five-year wilkinson microwave anisotropy probe (wmap) observations: Cosmological interpretation. *Astrophys. J. Supplement Series*, 180:330, 2009.
- [101] C. Kouveliotou, C. A. Meegan, G. J. Fishman, et al. Identification of two classes of gamma-ray bursts. *Astrophys. J. Lett.*, 413:L101, 1993.
- [102] A Krawczyk, A G Lyne, J A Gil, and B C Joshi. Observations of 14 pulsar glitches. *Mon. Not. R. Ast. Soc.*, 340:1087, 2003.
- [103] H. Krim and M. Viberg. Two decades of array signal processing research: the parametric approach. *Signal Processing Magazine, IEEE*, 13(4):67, 1996.
- [104] B. Krishnan, A. M. Sintes, M. A. Papa, B. F. Schutz, S. Frasca, and C. Palomba. Hough transform search for continuous gravitational waves. *Phys. Rev. D*, 70:082001, 2004.
- [105] K. Kuroda et al. Status of LCGT . *Class. Quantum Grav.*, 27:084004, 2010.

- [106] D. Lai and S. L. Shapiro. Gravitational radiation from rapidly rotating nascent neutron stars. *Astrophys. J.*, 442:259, 1995.
- [107] A. Lazzarini and J. Romano. Use of overlapping windows in the stochastic background search. LIGO-T040089-00-Z, 2004.
- [108] Y. Levin. QPOs during magnetar flares are not driven by mechanical normal modes of the crust. *Mon. Not. R. Ast. Soc. Lett.*, 368:35, 2006.
- [109] LIGO. Inspiral gravitational waves. <http://www.ligo.org/science/GW-Inspiral.php>, 2013.
- [110] L. Lindblom, B. J. Owen, and S. M. Morsink. Gravitational Radiation Instability in Hot Young Neutron Stars. *Phys. Rev. Lett.*, 80:4843, 1998.
- [111] E. Müller, M. Rampp, R. Buras, H.-T. Janka, and D. H. Shoemaker. Toward Gravitational Wave Signals from Realistic Core-Collapse Supernova Models. *Astrophys. J.*, 603:221, 2004.
- [112] M. Maggiore. Gravitational wave experiments and early universe cosmology. *Phys. Rep.*, 331:283, 2000.
- [113] V. Mandic and A. Buonanno. Accessibility of the pre-big-bang models to ligo. *Phys. Rev. D*, 73:063008, 2006.
- [114] P. M. McCulloch, P. A. Hamilton, D. McConnell, and E. A. King. The Vela glitch of Christmas 1988. *Nature*, 346:822, 1990.
- [115] P.F. Michelson. On detecting stochastic background gravitational radiation with terrestrial detectors. *Mon. Not. R. Ast. Soc. Lett.*, 227:933, 1987.
- [116] C. W. Misner, K. S. Thorne, and J. A. Wheeler. *Gravitation*. W. H. Freeman and Co, 1973.
- [117] P. D. Morley and R. García-Pelayo. Scaling law for pulsar glitches. *Europhys. Lett.*, 23:185–189, 1993.

- [118] E. Pajer N. Barnaby and M. Peloso. Gauge field production in axion inflation: Consequences for monodromy, non-gaussianity in the cmb, and gravitational waves at interferometers. *Phys. Rev. D*, 85:023525, 2012.
- [119] NASA. Swift grb table and lookup, 2013. http://swift.gsfc.nasa.gov/archive/grb_table/.
- [120] G. Nelemans, L.R. Yungelson, and S.F. Portegies-Zwart. The gravitational wave signal from the galactic disk population of binaries containing two compact objects. *Astr. and Astrophys.*, 375:890, 2001.
- [121] R. M. O’Leary, B. Kocsis, and A. Loeb. Gravitational waves from scattering of stellar-mass black holes in galactic nuclei. *Mon. Not. R. Ast. Soc.*, 395:2127, 2009.
- [122] S. Ölmez, V. Mandic, and X. Siemens. Gravitational-wave stochastic background from kinks and cusps on cosmic strings. *Phys. Rev. D*, 81:104028, 2010.
- [123] C. D. Ott. Gravitational wave signal catalog. <http://stellarcollapse.org/gwcatalog/ott2009>, 2009.
- [124] C. D. Ott. Probing the core-collapse supernova mechanism with gravitational waves. *Class. Quantum Grav.*, 26(20):204015, 2009.
- [125] C. D. Ott, H. Dimmelmeier, A. Marek, H.-T. Janka, I. Hawke, B. Zink, and E. Schnetter. 3D Collapse of Rotating Stellar Iron Cores in General Relativity Including Deleptonization and a Nuclear Equation of State. *Phys. Rev. Lett.*, 98:261101, 2007.
- [126] B. Owen. Detectability of periodic gravitational waves by initial interferometers. *Class. Quantum Grav.*, 23:S1–S7, 2006.
- [127] B J Owen. Maximum elastic deformations of compact stars with exotic equations of state. *Phys. Rev. Lett.*, 95:211101, 2005.
- [128] B. J. Owen, L. Lindblom, C. Cutler, B. F. Schutz, A. Vecchio, and N. Andersson.

- Gravitational waves from hot young rapidly rotating neutron stars. *Phys. Rev. D*, 58(8):084020, 1998.
- [129] J. Peterson. Observations and modeling of seismic background noise. 1993.
- [130] A. L. Piro and E. Pfahl. Fragmentation of collapsar disks and the production of gravitational waves. *Astrophys. J.*, 658:1173, 2007.
- [131] T. Prestegard and E. Thrane, 2012. LIGO L1200204 <https://dcc.ligo.org/cgi-bin/DocDB/ShowDocument?docid=93146>.
- [132] R. Prix, S. Giampanis, and C. Messenger. Search method for long-duration gravitational-wave transients from neutron stars. *Phys. Rev. D*, 84:023007, 2011.
- [133] P. Raffai et al. How to find long narrow-band gravitational wave transients with unknown frequency evolution? *Class. Quantum Grav.*, 24:S457–S568, 2007.
- [134] L. Rayleigh. On waves propagated along the plane surface of an elastic solid. *Proceed. of the London Math. Society*, 1:s1–17, 1885.
- [135] T. Regimbau and J.A. de Freitas Pacheco. Cosmic background of gravitational waves from rotating neutron stars. *Astr. and Astrophys.*, 376:381, 2001.
- [136] T. Regimbau and J.A. de Freitas Pacheco. Gravitational wave background from magnetars. *Astr. and Astrophys.*, 447:1, 2006.
- [137] S. Rost and C. Thomas. Array seismology: Methods and applications. *Rev. Geophys*, 40:2–1, 2002.
- [138] L. Santamaría and C. D. Ott. Gravitational wave emission from accretion disk instabilities - analytic models. 2011. LIGO T1100093.
- [139] S. Sarangi and S. H. H. Tye. Cosmic string production towards the end of brane inflation. *Phys. Lett. B*, 536:185, 2002.

- [140] B.S. Sathyaprakash and Bernard F. Schutz. Physics, astrophysics and cosmology with gravitational waves. *Living Reviews in Relativity*, 12(2), 2009.
- [141] P. R. Saulson. *Fundamentals of interferometric gravitational wave detectors*. World Scientific, 1994.
- [142] S. Scheidegger, R. Käppeli, S. C. Whitehouse, T. Fischer, and M. Liebendörfer. The influence of model parameters on the prediction of gravitational wave signals from stellar core collapse. *Astron. Astrophys.*, 514:A51, 2010.
- [143] B. F. Schutz. *A first course in general relativity*. Cambridge University Press, 1985.
- [144] T. Shan and T. Kailath. Adaptive beamforming for coherent signals and interference. *Acoustics, Speech and Signal Processing, IEEE Transactions on*, 33(3):527–536, 1985.
- [145] S Shapiro and S Teukolsky. *Black Holes, White Dwarfs, and Neutron Stars*. Wiley, 1983.
- [146] M. Shibata and Y.-I. Sekiguchi. Three-dimensional simulations of stellar core collapse in full general relativity: Nonaxisymmetric dynamical instabilities. *Phys. Rev. D*, 71:024014, 2005.
- [147] X. Siemens et al. Size of the smallest scales in cosmic string networks. *Phys. Rev. D*, 66:043501, 2002.
- [148] X. Siemens et al. Gravitational wave bursts from cosmic (super)strings: Quantitative analysis and constraints. *Phys. Rev. D*, 73:105001, 2006.
- [149] J. Slutsky et al. Methods for reducing false alarms in searches for compact binary coalescences in LIGO data. *Class. Quantum Grav.*, 27:165023, 2010.
- [150] H. Sotani, K. D. Kokkotas, and N. Stergioulas. Alfvén quasi-periodic oscillations in magnetars. *Mon. Not. R. Ast. Soc. Lett.*, 385:5, 2008.
- [151] A.A. Starobinskii. Spectrum of relict gravitational radiation and the early state of the universe. *Soviet Physics JETP Letters*, 30:682, 1979.

- [152] J. Sylvestre. Optimal generalization of power filters for gravitational wave bursts, from single to multiple detectors. *Phys. Rev. D*, 68:102005, 2003.
- [153] T. L. Smith, E. Pierpaoli, and M. Kamionkowski. A new cosmic microwave background constraint to primordial gravitational waves. *Phys. Rev. Lett.*, 97:021301, 2006.
- [154] T. T. Regimbau and J.A. de Freitas Pacheco. Cosmic background of gravitational waves from rotating neutron stars. *Astronomy and Astrophysics*, 376:381, 2001.
- [155] R. Takahashi and the TAMA Collaboration. Status of tama300. *Class. Quantum Grav.*, 21(5):S403, 2004.
- [156] The LIGO and Virgo Collaborations. Search for gravitational waves associated with gamma-ray bursts during LIGO science run 6 and Virgo science runs 2 and 3. *The Astrophys. J.*, 760:12, 2012.
- [157] T. A. Thompson, P. Chang, and E. Quataert. Magnetar Spin-Down, Hyperenergetic Supernovae, and Gamma-Ray Bursts. *Astrophys. J.*, 611:380, 2004.
- [158] E. Thrane et al. Probing the anisotropies of a stochastic gravitational-wave background using a network of ground-based laser interferometers. *Phys. Rev. D*, 80:122002, 2009.
- [159] E Thrane, S Kandhasamy, C D Ott, et al. Long gravitational-wave transients and associated detection strategies for a network of terrestrial interferometers. *Phys. Rev. D*, 83:083004, 2011.
- [160] C. A. van Eysden and A Melatos. Gravitational radiation from pulsar glitches. *Class. Quantum Grav.*, 25:225020, 2008.
- [161] M.H.P.M. van Putten. Proposed Source of Gravitational Radiation from a Torus around a Black Hole. *Phys. Rev. Lett.*, 87(9):091101, 2001.
- [162] M.H.P.M. van Putten. LIGO/VIRGO searches for gravitational radiation in hypernovae. *Astrophys. J. Lett.*, 575:71–74, 2002.

- [163] M.H.P.M. van Putten. Gravitational Waveforms of Kerr Black Holes Interacting with High-Density Matter. *Astrophys. J. Lett.*, 684:91, 2008.
- [164] J. Weber. Detection and generation of gravitational waves. *Phys. Rev.*, 117:306–313, 1960.
- [165] J. M. Weisberg, D. J. Nice, and J. H. Taylor. Timing Measurements of the Relativistic Binary Pulsar PSR B1913+16. *The Astrophys. J.*, 722(2):1030, 2010.
- [166] S. E. Woosley. Gamma-ray bursts from stellar mass accretion disks around black holes. *Astrophys. J.*, 405:273, 1993.
- [167] X. Siemens, V. Mandic, and J. Creighton. Gravitational-wave stochastic background from cosmic strings. *Physical Review Letters*, 98:043531, 2007.

Appendix A

Statistics of long GW transient analysis pipeline

A.1 Derivations

We describe how a GW source can be characterized by its power spectrum $H(t; f)$, we construct an estimator $\hat{Y}(t; f)$ for $H(t; f)$ and calculate the associated variance. We construct an estimator for the variance.

A.1.1 Introduction and notation

Working in the transverse-traceless gauge we write down the general form of a GW field, which can depend on direction $\hat{\Omega}$, polarization state A and frequency f (see, Section 2.2):

$$h_{ab}(t, \vec{x}) = \sum_A \int_{-\infty}^{\infty} df \int_{S^2} d\hat{\Omega} e_{ab}^A(\hat{\Omega}) \tilde{h}_A(f, \hat{\Omega}) e^{2\pi i f(t + \hat{\Omega} \cdot \vec{x}/c)}. \quad (\text{A.1})$$

Here \vec{x} and $\hat{\Omega}$ are defined in equatorial coordinate systems defined in Figure A.1. The polarization tensors $e_{ab}^{+, \times}$ can be obtained by the similarity transformation using the rotation matrix $R: (X, Y, Z) \rightarrow (x, y, z)$,

$$R = \begin{pmatrix} -\cos \theta \cos \phi & -\sin \phi & -\cos \phi \sin \theta \\ -\cos \theta \sin \phi & \cos \phi & -\sin \theta \sin \phi \\ \sin \theta & 0 & -\cos \theta \end{pmatrix}. \quad (\text{A.2})$$

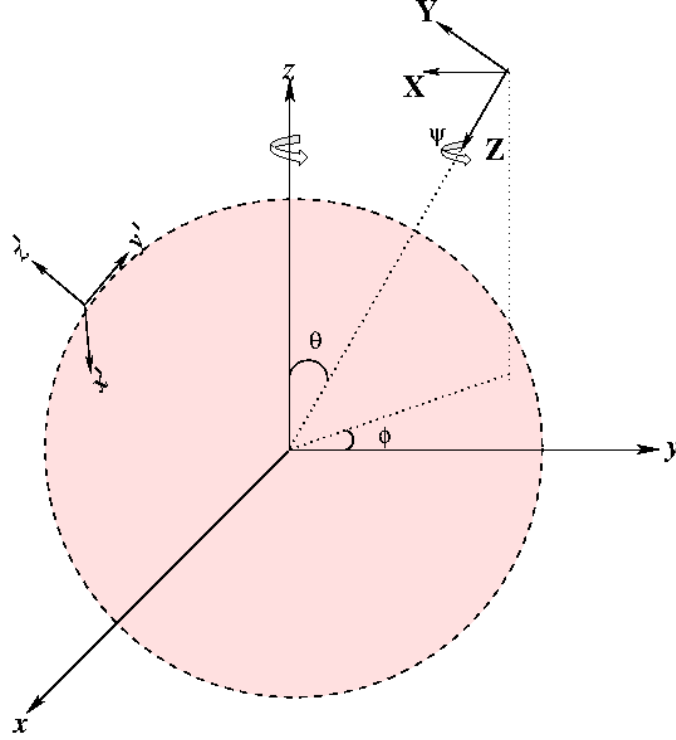


Figure A.1: The above figure shows different coordinate systems and angles involved in the calculation of strain induced in GW detectors. For unpolarized signals, we assume $\psi = 0$.

where the source direction $\hat{\Omega}$ is given by

$$\hat{\Omega} = \cos \phi \sin \theta \hat{x} + \sin \theta \sin \phi \hat{y} + \cos \theta \hat{z}, \quad (\text{A.3})$$

and wave propagation is in $-\hat{\Omega}$. In calculating R above we assumed that ψ , called polarization angle, is zero (see Figure A.1). In general, it need not be the case. Also the XY plane of wave frame could make a non-zero angle ι , called inclination angle, with respect to $\hat{\Omega}$. If we include those angles, then $R:(X, Y, Z) \rightarrow (x, y, z)$ becomes,

$$R = \begin{pmatrix} -(c\theta c\phi c\psi + s\phi s\psi)c\iota + c\phi s\theta s\iota & -c\psi s\phi + c\theta c\phi s\psi & -c\iota c\phi s\theta - (c\theta c\phi c\psi + s\phi s\psi)s\iota \\ -(c\theta c\psi s\phi - c\phi s\psi)c\iota + s\theta s\phi s\iota & c\phi c\psi + c\theta s\phi s\psi & -c\iota s\theta s\phi - (c\theta c\psi s\phi - c\phi s\psi)s\iota \\ c\iota c\psi s\theta + c\theta s\iota & -s\theta s\psi & c\psi s\theta s\iota - c\theta c\iota \end{pmatrix} \quad (\text{A.4})$$

Since we are interested in unpolarized sources, here after we would assume $\psi = 0$ and $\iota = 0$.

Since we are looking for GW transients, we restrict our attention to *point sources* for which $h_A(f, \hat{\Omega}) = h_A(f)\delta(\hat{\Omega} - \hat{\Omega}_0)$. We perform the integral over $\hat{\Omega}$ and obtain:

$$h_{ab}(t, \vec{x}) = \sum_A \int_{-\infty}^{\infty} df e_{ab}^A(\hat{\Omega}_0) \tilde{h}_A(f) e^{2\pi i f(t + \hat{\Omega}_0 \cdot \vec{x}/c)}. \quad (\text{A.5})$$

For simplicity, we henceforth replace $\hat{\Omega}_0$ with $\hat{\Omega}$. It follows that the GW strain in detector I is given by

$$h_I(t) = \sum_A \int_{-\infty}^{\infty} df \tilde{h}_A(f, \hat{\Omega}) e^{2\pi i f(t + \hat{\Omega} \cdot \vec{x}_I/c)} e_{ab}^A(\hat{\Omega}) d_I^{ab}(t) \quad (\text{A.6})$$

where $d_I^{ab}(t)$ is the detector response tensor at time t :

$$d_I = \frac{1}{2}(\hat{x}'_I \otimes \hat{x}'_I - \hat{y}'_I \otimes \hat{y}'_I) . \quad (\text{A.7})$$

Here, the two detector arms lie along the $\hat{x}'(t)$ and $\hat{y}'(t)$ axes, which are time-dependent due to the rotation of the Earth.

We now consider a finite stretch of $h_I(t)$ and take the discrete Fourier transform of Eq.(A.6) to obtain:

$$\tilde{h}_I(t; f) = \sum_A \tilde{h}_A(t; f, \hat{\Omega}) e^{2\pi i f \hat{\Omega} \cdot \vec{x}_I/c} F_I^A(t; \hat{\Omega}). \quad (\text{A.8})$$

where we define the ‘‘antenna factors’’ (see e.g., [19]) to be

$$F_I^A(t; \hat{\Omega}) \equiv e_{ab}^A(\hat{\Omega}) d_I^{ab}(t). \quad (\text{A.9})$$

We define the GW strain power spectrum to be

$$\langle \tilde{h}_A^*(t; f) \tilde{h}_{A'}(t; f) \rangle = \frac{1}{2} H_{AA'}(t; f), \quad (\text{A.10})$$

where the factor $1/2$ comes from the fact that $H_{AA'}(t; f)$ is the one-sided power spectrum.

It is convenient to characterize the source with a single spectrum that includes contri-

butions from both $+$ and \times polarization. We therefore define

$$H(t; f) \equiv \text{Tr} [H_{AA'}(t; f)], \quad (\text{A.11})$$

so as to be invariant under change of polarization bases. This definition is a generalization of the one-sided power spectrum for unpolarized sources found in [19, 8, 158]. Our goal now is to derive an estimator for $H(t; f)$ in a data segment over which it is presumed to be constant.

A.1.2 Derivation of \hat{Y}

Let $s_I(t) = h_I(t) + n_I(t)$ be the strain time series from detector I , where $h_I(t)$ is the GW strain and $n_I(t)$ is the detector noise. Following [19, 8, 158], we combine the strain time series from two spatially separated detectors, $s_I(t), s_J(t)$, to construct an estimator for GW-power $H(t; f)$ for a point source at a sky position $\hat{\Omega}$,

$$\hat{Y}(t; f, \hat{\Omega}) \equiv 2 \text{Re} \left[\tilde{Q}_{IJ}(t; f, \hat{\Omega}) \tilde{s}_I^*(t; f) \tilde{s}_J(t; f) \right] \quad (\text{A.12})$$

where $\tilde{Q}_{IJ}(t; f, \hat{\Omega})$ is some filter function to be determined below. We take the real part to ensure physicality of the estimator. The expectation value of $\hat{Y}(t; f, \hat{\Omega})$ is given by

$$\langle \hat{Y}(t; f, \hat{\Omega}) \rangle = 2 \text{Re} \left[\tilde{Q}_{IJ}(t; f, \hat{\Omega}) \langle \tilde{h}_I^*(t; f) \tilde{h}_J(t; f) \rangle \right], \quad (\text{A.13})$$

since, by assumption, there is no correlation between signal and noise and also no correlation between noise in two spatially separated detectors, the other terms vanish.

Combining Eqs. (A.8), (A.13) and (A.10) we get

$$\begin{aligned} \langle \hat{Y}(t; f, \hat{\Omega}) \rangle = & 2 \text{Re} \left[\tilde{Q}_{IJ}(t; f, \hat{\Omega}) \sum_{AA'} \frac{1}{2} H_{AA'}(t; f) \right. \\ & \left. e^{-2\pi i f (\hat{\Omega} \cdot (\vec{x}_I - \vec{x}_J) / c)} F_I^A(t; \hat{\Omega}) F_J^{A'}(t; \hat{\Omega}) \right] \end{aligned} \quad (\text{A.14})$$

In order to simplify the form of $H_{AA'}(t; f)$ we now consider *unpolarized* sources, for which

$$H_{AA'}(t; f) = \frac{1}{2}H(t; f)\delta_{AA'}. \quad (\text{A.15})$$

For unpolarized sources,

$$\begin{aligned} \langle \hat{Y}(t; f, \hat{\Omega}) \rangle &= \frac{1}{2} \text{Re} \left[\tilde{Q}_{IJ}(t; f, \hat{\Omega}) H(t; f) e^{-2\pi i f \hat{\Omega} \cdot \Delta \vec{x}_{IJ}/c} \right. \\ &\quad \left. \sum_A F_I^A(t; \hat{\Omega}) F_J^A(t; \hat{\Omega}) \right], \end{aligned} \quad (\text{A.16})$$

where we have defined $\Delta \vec{x}_{IJ} \equiv \vec{x}_I - \vec{x}_J$.

We desire that $\langle \hat{Y} \rangle = H(t; f)$, which implies:

$$\tilde{Q}_{IJ}(t; f, \hat{\Omega}) = \frac{2 e^{2\pi i f \hat{\Omega} \cdot \Delta \vec{x}_{IJ}/c}}{\sum_A F_I^A(t; \hat{\Omega}) F_J^A(t; \hat{\Omega})}. \quad (\text{A.17})$$

By setting $Q_{IJ}(t; f, \hat{\Omega})$ thusly, we account for the phase difference between detectors I and J ensuring that the bracketed quantity in Eq. (A.16) is real. We also account for the detector pair efficiency. Finally, we define (unpolarized) *pair efficiency* as

$$\epsilon_{IJ}(t; \hat{\Omega}) \equiv \frac{1}{2} \sum_A F_I^A(t; \hat{\Omega}) F_J^A(t; \hat{\Omega}), \quad (\text{A.18})$$

which enables us to rewrite the filter function as

$$\tilde{Q}_{IJ}(t; f, \hat{\Omega}) = \frac{1}{\epsilon_{IJ}(t; \hat{\Omega})} e^{2\pi i f \hat{\Omega} \cdot \Delta \vec{x}_{IJ}/c}. \quad (\text{A.19})$$

Since $\hat{Y}(t; f, \hat{\Omega}) \propto \tilde{Q}(t; f, \hat{\Omega})$ and $\tilde{Q} \propto 1/\epsilon_{IJ}(t; f, \hat{\Omega})$, it follows that $\hat{Y}(t; f, \hat{\Omega}) \propto 1/\epsilon_{IJ}(t; \hat{\Omega})$. This can be understood as follows. If we observe a modest value of strain power from a direction associated with low efficiency, we may infer (if the signal is statistically significant) that the true source power is much higher because the network only “sees” some fraction of the true GW power.

A.1.3 Variance of the estimator

We derive an expression for the variance of $\hat{Y}(t; f, \hat{\Omega})$, $\sigma_Y(t; f, \hat{\Omega})^2 \equiv \langle \hat{Y}(t; f, \hat{\Omega})^2 \rangle - \langle \hat{Y}(t; f, \hat{\Omega}) \rangle^2$. In searches for persistent stochastic GWs, the second term is usually omitted and the first term is simplified by assuming that signal in each pixel is small compared to the noise. Such small signals are extracted by averaging over a very large number of segments (see, e.g., [19]). Since we are dealing with transients, however, the signal may be comparable to the noise and so we can not neglect any terms in our calculation of σ_Y^2 .

To begin we define a new (complex-valued) estimator that will be handy in our derivation of σ_Y^2 :

$$\hat{W}(t; f, \hat{\Omega}) \equiv 2 \tilde{Q}_{IJ}(t; f, \hat{\Omega}) \tilde{s}_I^*(t; f) \tilde{s}_J(t; f). \quad (\text{A.20})$$

Our GW power estimator $\hat{Y}(t; f, \hat{\Omega})$ is simply the real part of $\hat{W}(t; f, \hat{\Omega})$:

$$\hat{Y}(t; f, \hat{\Omega}) = \frac{1}{2} \left(\hat{W}(t; f, \hat{\Omega}) + \hat{W}(t; f, \hat{\Omega})^* \right). \quad (\text{A.21})$$

For notational compactness, we shall omit the arguments of $\hat{W}(t; f, \hat{\Omega})$ in the remainder of this derivation. It follows that the variance of $\hat{Y}(t; f, \hat{\Omega})$ can be written as

$$\sigma_Y^2 = \frac{1}{4} \left[\left(\langle \hat{W}^2 \rangle - \langle \hat{W} \rangle^2 \right) + \left(\langle \hat{W}^{*2} \rangle - \langle \hat{W}^* \rangle^2 \right) + 2 \sigma_W^2 \right], \quad (\text{A.22})$$

where

$$\sigma_W^2 \equiv \langle |\hat{W}|^2 \rangle - |\langle \hat{W} \rangle|^2. \quad (\text{A.23})$$

Now we evaluate the three terms in Eq. (A.22) beginning with σ_W^2 . We obtain

$$\begin{aligned} \sigma_W^2(t; f, \hat{\Omega}) &= 4 \left[\langle \tilde{s}_I^*(t; f) \tilde{s}_J(t; f) \tilde{s}_I(t; f) \tilde{s}_J^*(t; f) \rangle \right. \\ &\quad \left. - \langle \tilde{s}_I^*(t; f) \tilde{s}_J(t; f) \rangle \langle \tilde{s}_I(t; f) \tilde{s}_J^*(t; f) \rangle \right] \\ &\quad \left| \tilde{Q}_{IJ}(t; f, \hat{\Omega}) \right|^2. \end{aligned} \quad (\text{A.24})$$

For mean-zero Gaussian random variables, we can expand the four-point correlation into a

sum of products of two-point correlations. We substitute $s = h + n$ and set signal-noise cross terms to zero along with noise-noise cross terms from different detectors. The variance becomes

$$\begin{aligned} \sigma_W^2(t; f, \hat{\Omega}) = & 4 \left[\langle \tilde{h}_I^*(t; f) \tilde{h}_I(t; f) \rangle \langle \tilde{h}_J(t; f) \tilde{h}_J^*(t; f) \rangle + \right. \\ & \langle \tilde{h}_I^*(t; f) \tilde{h}_I(t; f) \rangle \langle \tilde{n}_J(t; f) \tilde{n}_J^*(t; f) \rangle + \\ & \langle \tilde{h}_J(t; f) \tilde{h}_J^*(t; f) \rangle \langle \tilde{n}_I^*(t; f) \tilde{n}_I(t; f) \rangle + \\ & \left. \langle \tilde{n}_I^*(t; f) \tilde{n}_I(t; f) \rangle \langle \tilde{n}_J(t; f) \tilde{n}_J^*(t; f) \rangle \right] \\ & \left| \tilde{Q}_{IJ}(t; f, \hat{\Omega}) \right|^2, \end{aligned} \quad (\text{A.25})$$

Evaluating the four terms in Eq. (A.25), we obtain

$$\begin{aligned} \sigma_W^2(t; f, \hat{\Omega}) = & \left[\epsilon_{II}(t; \hat{\Omega}) \epsilon_{JJ}(t; \hat{\Omega}) H(t; f)^2 + \right. \\ & H(t; f) \left(\epsilon_{II}(t; \hat{\Omega}) N_J(t; f) + \epsilon_{JJ}(t; \hat{\Omega}) N_I(t; f) \right) \\ & \left. + N_I(t; f) N_J(t; f) \right] \left| \tilde{Q}_{IJ}(t; f, \hat{\Omega}) \right|^2, \end{aligned} \quad (\text{A.26})$$

where ϵ is defined in Eq. (A.18) and where $N_I(t; f)$ is the one-sided noise-power spectra:

$$N_I(t; f) \equiv 2 |\tilde{n}_I(t; f)|^2. \quad (\text{A.27})$$

Using the same line of reasoning, we calculate the remaining terms in Eq. (A.22):

$$\langle \hat{W}^2 \rangle - \langle \hat{W} \rangle^2 = \langle \hat{W}^{*2} \rangle - \langle \hat{W}^* \rangle^2 = H(t; f)^2. \quad (\text{A.28})$$

Combining Eqs. (A.22) and (A.28), we conclude that

$$\sigma_Y^2 = \frac{1}{2} [\sigma_W^2 + H(t; f)^2]. \quad (\text{A.29})$$

The factor of 1/2 comes about from the fact that $\hat{Y}(t; f, \hat{\Omega})$ is real whereas $\hat{W}(t; f, \hat{\Omega})$ is complex. We note that in the small-signal limit $H(f) \rightarrow 0$ and the variance reduces to the

canonical stochastic result [19]:

$$\sigma_Y^2 \rightarrow \frac{1}{2} \left(N_I(t; f) N_J(t; f) \left| \tilde{Q}_{IJ}(t; f, \hat{\Omega}) \right|^2 \right), \quad (\text{A.30})$$

A.1.4 Expectation value of $\hat{\sigma}_Y^2$

Our estimator for the variance of \hat{Y} is given by

$$\hat{\sigma}_Y^2(t; f, \hat{\Omega}) = \frac{1}{2} \left| \tilde{Q}_{IJ}(t; f, \hat{\Omega}) \right|^2 P_I^{\text{adj}}(f) P_J^{\text{adj}}(f), \quad (\text{A.31})$$

where P_I is the average auto-power in neighboring pixels:

$$P_I^{\text{adj}}(f) \equiv 2 \overline{|\tilde{s}_I(f)|^2}. \quad (\text{A.32})$$

The overline denotes an average over neighboring pixels. By averaging over neighboring pixels, we assume that the detector noise in any given pixel can be characterized by looking at its neighbors. This assumption is discussed below. Now we calculate the expectation value of our estimator for variance $\hat{\sigma}_Y^2$ given in Eq. (A.31) in order to compare it to the theoretical variance given in Eqs. (A.29) and (A.26). Eqs. (3.8) and (3.9) together imply

$$\begin{aligned} \langle \hat{\sigma}_Y^2(t; f, \hat{\Omega}) \rangle &= 2 \left| \tilde{Q}_{IJ}(t; f, \hat{\Omega}) \right|^2 \\ &\quad \langle s_I^{*\text{adj}}(f) s_I^{\text{adj}}(f) s_J^{*\text{adj}}(f) s_J^{\text{adj}}(f) \rangle. \end{aligned} \quad (\text{A.33})$$

Using Equation (A.24) to write the expectation value of $\hat{\sigma}_Y^2$ in terms of the theoretical value of σ_W^2 , we find

$$\begin{aligned} \langle \hat{\sigma}_Y^2(t; f, \hat{\Omega}) \rangle &= \frac{1}{2} \left[\sigma_W^2(t; f, \hat{\Omega}) + 4 \left| \tilde{Q}_{IJ}(t; f, \hat{\Omega}) \right|^2 \right. \\ &\quad \left. \langle \tilde{s}_I^{\text{adj}*}(t; f) \tilde{s}_J^{\text{adj}}(t; f) \rangle \langle \tilde{s}_I^{\text{adj}}(t; f) \tilde{s}_J^{\text{adj}*}(t; f) \rangle \right] \\ &= \frac{1}{2} \left[\sigma_W^2(t; f, \hat{\Omega}) + \left| \langle \hat{W} \rangle \right|^2 \right] \\ &= \frac{1}{2} \left[\sigma_W^2(t; f, \hat{\Omega}) + H(t; f)^2 \right] \end{aligned} \quad (\text{A.34})$$

Since this is the theoretical variance from (A.29), we conclude that $\langle \hat{\sigma}_Y^2 \rangle = \sigma_Y^2$. Thus, Eq. (3.8) provides an unbiased estimator for σ_Y^2 . Here we have assumed that the noise and signal are comparable in neighboring segments. This assumption can fail for rapidly changing, high-SNR signals and also for highly non-stationary noise, and so additional work may be required to estimate σ in these situations.

A.1.5 Distribution of $\text{SNR}(t; f, \hat{\Omega})$

For the case of $\delta F = 1/T$, we can derive the distribution of $\text{SNR}(t; f, \hat{\Omega})$ as follows. The $\text{SNR}(t; f, \hat{\Omega})$ is defined as,

$$\text{SNR}(t; f, \hat{\Omega}) = \frac{\text{Re}[s_1(f; t) * s_2(f; t)]}{\sqrt{P_{1,\text{adj}} P_{2,\text{adj}}}}, \quad (\text{A.35})$$

where $s_1(f; t)$ and $s_2(f; t)$ are Fourier transforms of time series from two detectors (hence complex numbers) and, $P_{1,\text{adj}}$ and $P_{2,\text{adj}}$ are (averaged) power spectrum calculated from adjacent N of segments.

In general, if x and y are Gaussian distributed variables with mean 0 and variance σ^2 i.e,

$$f(x) = \frac{1}{\sqrt{2\pi\sigma^2}} e^{-\frac{x^2}{2\sigma^2}} \quad \text{and} \quad (\text{A.36})$$

$$f(y) = \frac{1}{\sqrt{2\pi\sigma^2}} e^{-\frac{y^2}{2\sigma^2}} \quad (\text{A.37})$$

then the distribution of a new variable z defined as $z = xy$ will be given by the expression,

$$f(z) = \frac{1}{\pi\sigma^2} K_0 \left(\frac{|z|}{\sigma^2} \right) \quad (\text{A.38})$$

where $K_0(x)$ is the modified Bessel function of second kind.

In our transient pipeline, $s_1(f)$ and $s_2(f)$ (in frequency domain) are complex numbers and hence $\text{Re}(s_1(f) * s_2(f))$, also known as Y , is actually sum of two such ‘ z ’ distributions. Assuming $s_1(f)$ and $s_2(f)$ are Gaussian variables, using convolution theorem we can

calculate the distribution of Y and it is given by

$$f_Y(y) = \frac{1}{2\sigma^2} e^{-\frac{|y|}{\sigma^2}}. \quad (\text{A.39})$$

In literature the above distribution is known as double exponential or Laplace distribution. This would be the distribution of numerator of our $\text{SNR}(t; f, \hat{\Omega})$. Figure A.2 shows the fit of Eq. (A.39) to simulated data with Gaussian distribution with constant $\sigma(f)$ (for real detector data $\sigma(f)$ is not constant).

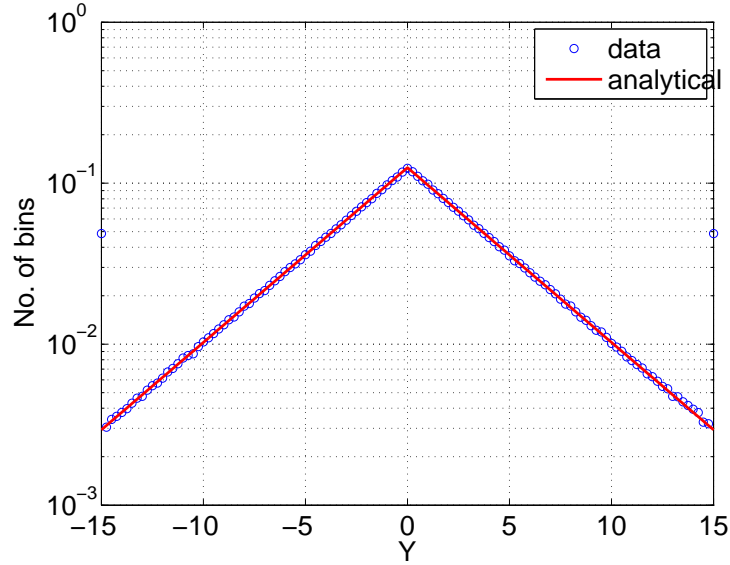


Figure A.2: Distribution of Y (Eq. (A.39)) for Gaussian data.

Now we calculate the distribution of the denominator of $\text{SNR}(t; f, \hat{\Omega})$. Each of P_{adj} in the denominator is calculated by averaging over P 's obtained from N number of neighboring segments i.e.,

$$P1_{\text{adj}} = \frac{1}{N} \sum_{j=1}^N P1_j \quad (\text{A.40})$$

$$P2_{\text{adj}} = \frac{1}{N} \sum_{j=1}^N P2_j \quad (\text{A.41})$$

The distributions of P themselves are well known in the literature (it is the sum of squares

of two Gaussian variables) and are described by exponential distributions. But here we are interested in the average of N such distributions and using the convolution theorem we obtain the distribution of P_{adj} averaged over N segments as

$$f_P(z) = \frac{N^N}{2^N \sigma^{2N} \Gamma(N)} e^{-\frac{Nz}{2\sigma^2}} z^{N-1} \quad (z \geq 0) \quad (\text{A.42})$$

In Figure A.3, we compare the above analytical expression with simulated data.

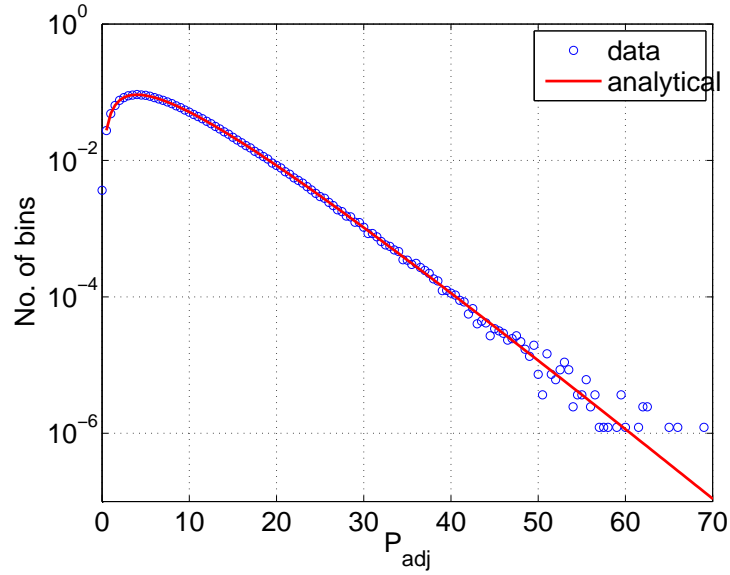


Figure A.3: Distribution of P_{adj} (Eq. (A.42)) using simulated data.

Using the distributions for $P_{1\text{adj}}$ and $P_{2\text{adj}}$ we can now calculate the distribution of denominator of $\text{SNR}(t; f, \hat{\Omega})$, which is given by

$$f_{\sigma_Y}(z) = \frac{N^{2N}}{2^{2N-2} \sigma^{4N} (\Gamma(N))^2} K_0 \left(\frac{Nz}{\sigma^2} \right) z^{2N-1} \quad (\text{A.43})$$

Figure A.4 shows the comparison between analytical expression for σ_Y and simulated data.

From distribution of Y and σ_Y we can calculate the distribution of $\text{SNR}(t; f, \hat{\Omega})$ which

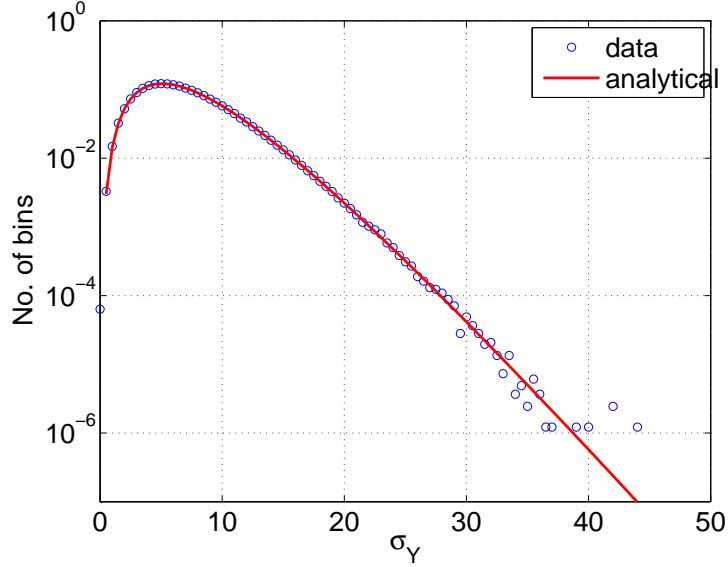


Figure A.4: Distribution of σ_Y (Eq. (A.43) using simulated data).

is given by

$$f_{\text{SNR}}(z) = \frac{N^{2N}}{2^{2N-1}\sigma^{4N+2}(\Gamma(N))^2} \int_0^\infty |x| e^{-\frac{|xz|}{\sigma^2}} K_0\left(\frac{Nx}{\sigma^2}\right) x^{2N-1} dx \quad (\text{A.44})$$

The above integral has different convergence properties depending on the values z , which in our case can be any real number, and hence writing down a simple final expression is difficult. A naive run on MATHEMATICA yields answers in terms of hypergeometric functions for different ranges of z . But for fixed values of N and z , we can solve the above integral numerically. Figure A.5 shows $f_{\text{SNR}}(z)$ for $N=2$ which also agrees with the MC simulations.

Even though the above integral is difficult to solve analytically, because of the z term, it can be analytically evaluated for the moments of the distribution. In such case, instead of doing the x integral first, for the required moment we do the z integral first and then do the x integral later (this takes care of the z term). In this way we get the variance of $\text{SNR}(t; f, \hat{\Omega})$ as $\frac{N^2}{2(N-1)^2}$ (valid for $N > 1$). We see that the distribution of SNR is a function of the number of segments N used to calculate P_{adj} and is similar to the bias factor we used in SGWB searches (see Section 2.3.3).

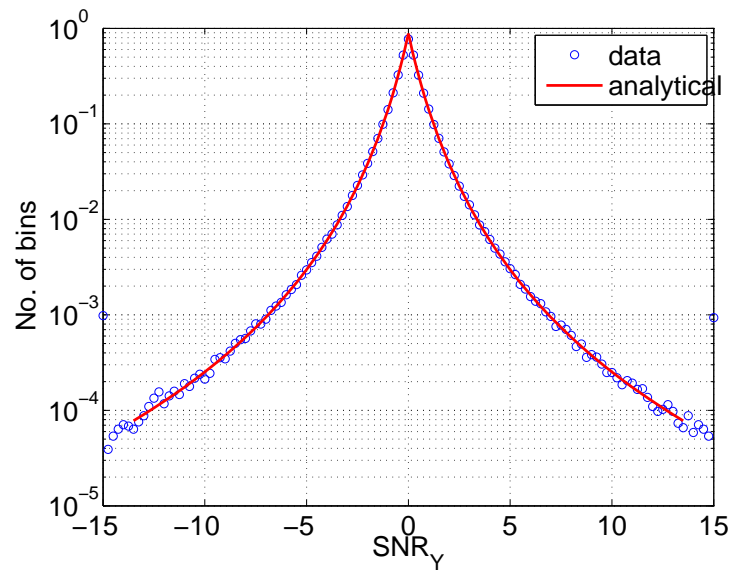


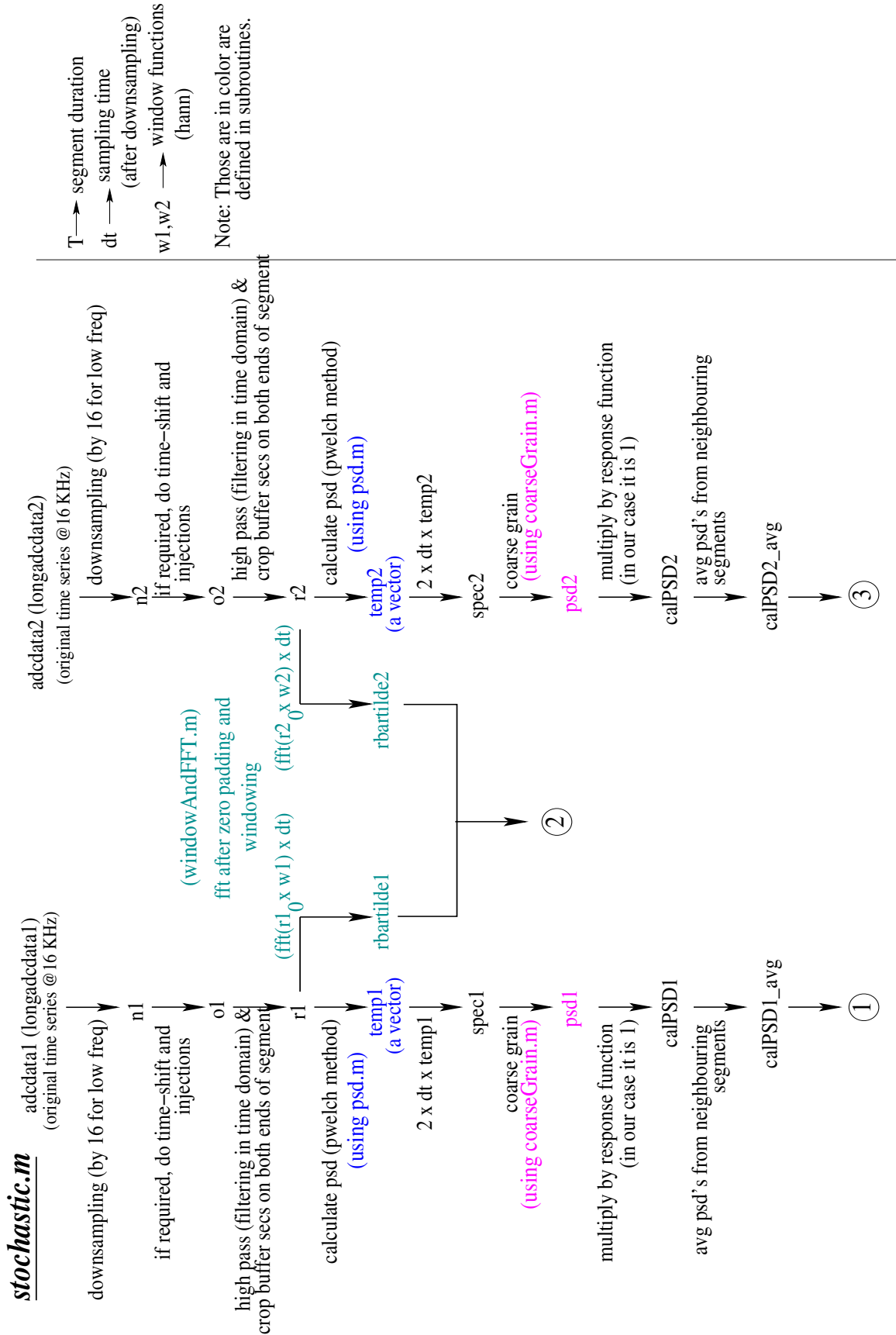
Figure A.5: Distribution of $\text{SNR}(t; f, \hat{\Omega})$ using simulated data (for $N = 2$).

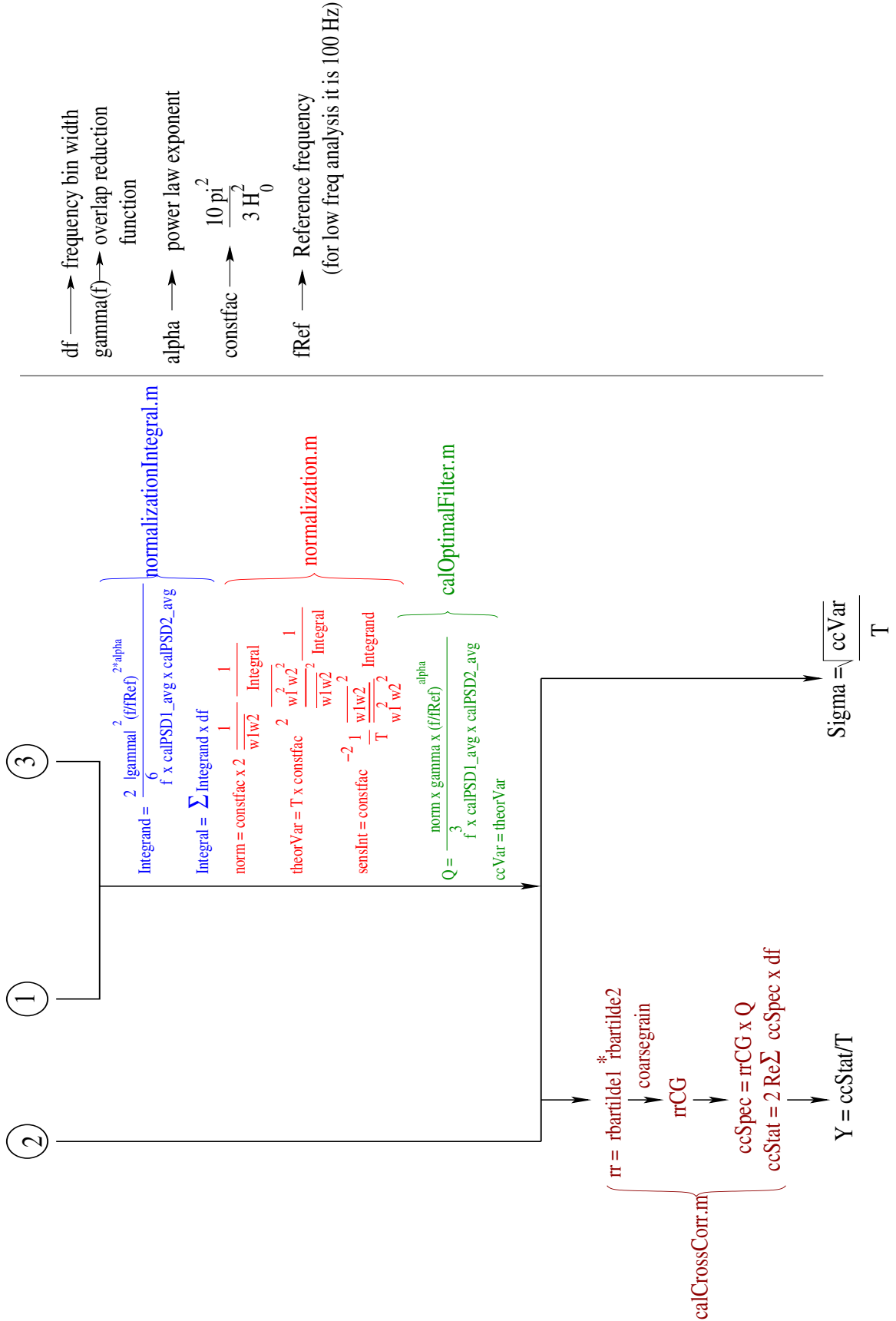
Appendix B

Flowcharts of analysis pipelines

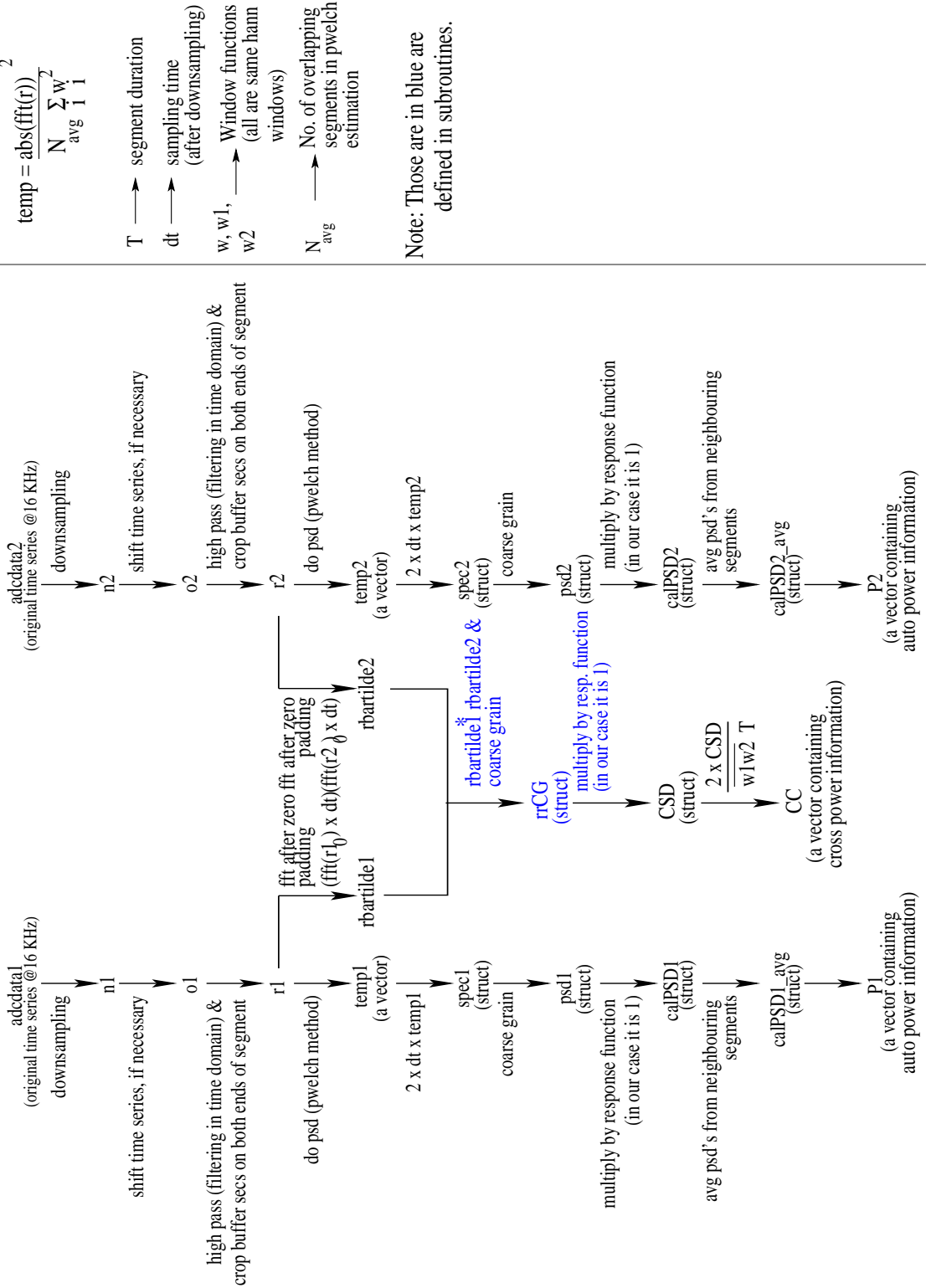
In the next four pages, we have provided the flowcharts of stochastic and long GW transient pipelines. The first two pages of flowchart correspond to stochastic GW pipeline while the next two pages correspond to long GW transient pipeline. Both the analysis pipelines are written in Matlab.

The stochastic analysis pipeline is made up of a master code called ‘stochastic.m’ while the long GW transient pipeline, also called *STAMP*, has two main codes: ‘preproc.m’ and ‘stochmap.m’ (in a recent revision ‘stochmap.m’ was renamed as ‘clustermmap.m’). In *STAMP* pipeline, ‘preproc.m’ produces ft-maps and other intermediate data while ‘stochmap.m’ computes calibrated ft-maps and applies pattern recognition algorithms (which is not shown in the flowchart). The colored variables in the flowcharts represent variables defined and/or calculated in sub-functions while other variables are defined in the main functions themselves.





preproc.m



$$\text{temp} = \frac{\text{abs}(\text{fft}(r))^2}{N_{\text{avg}} \sum_{i=1}^2 w_i^2}$$

- T → segment duration
- dt → sampling time (after downsampling)
- w, w1, w2 → Window functions (all are same hann windows)
- N_{avg} → No. of overlapping segments in pwelch estimation

Note: Those are in blue are defined in subroutines.

